

**CHEMICAL ENGINEERING DIVISION
BASIC ENERGY SCIENCES RESEARCH:**

July 1976—September 1977

PROPERTY OF
ANL-W Technical Library



U of C-AUA-USDOE

ARGONNE NATIONAL LABORATORY, ARGONNE, ILLINOIS

**Prepared for the U. S. DEPARTMENT OF ENERGY
under Contract W-31-109-Eng-38**

The facilities of Argonne National Laboratory are owned by the United States Government. Under the terms of a contract (W-31-109-Eng-38) between the U. S. Department of Energy, Argonne Universities Association and The University of Chicago, the University employs the staff and operates the Laboratory in accordance with policies and programs formulated, approved and reviewed by the Association.

MEMBERS OF ARGONNE UNIVERSITIES ASSOCIATION

The University of Arizona	Kansas State University	The Ohio State University
Carnegie-Mellon University	The University of Kansas	Ohio University
Case Western Reserve University	Loyola University	The Pennsylvania State University
The University of Chicago	Marquette University	Purdue University
University of Cincinnati	Michigan State University	Saint Louis University
Illinois Institute of Technology	The University of Michigan	Southern Illinois University
University of Illinois	University of Minnesota	The University of Texas at Austin
Indiana University	University of Missouri	Washington University
Iowa State University	Northwestern University	Wayne State University
The University of Iowa	University of Notre Dame	The University of Wisconsin

NOTICE

This report was prepared as an account of work sponsored by the United States Government. Neither the United States nor the United States Department of Energy, nor any of their employees, nor any of their contractors, subcontractors, or their employees, makes any warranty, express or implied, or assumes any legal liability or responsibility for the accuracy, completeness or usefulness of any information, apparatus, product or process disclosed, or represents that its use would not infringe privately-owned rights. Mention of commercial products, their manufacturers, or their suppliers in this publication does not imply or connote approval or disapproval of the product by Argonne National Laboratory or the U. S. Department of Energy.

Printed in the United States of America
Available from
National Technical Information Service
U. S. Department of Commerce
5285 Port Royal Road
Springfield, Virginia 22161
Price: Printed Copy \$6.50; Microfiche \$3.00

ANL-78-42

ARGONNE NATIONAL LABORATORY
9700 South Cass Avenue
Argonne, Illinois 60439

CHEMICAL ENGINEERING DIVISION
BASIC ENERGY SCIENCES RESEARCH:

July 1976—September 1977

F. A. Cafasso	Associate Division Director
M. Blander	Group Leader, Physical Inorganic Chemistry
V. A. Maroni	Group Leader, Chemistry of Liquid Metals
C. E. Johnson	Group Leader, Thermochemistry
R. Kumar	Group Leader, Environmental Chemistry
S. Siegel	Group Leader, Structural and Surface Chemistry

TABLE OF CONTENTS

	<u>Page</u>
ABSTRACT	1
SUMMARY	2
I. PHYSICAL INORGANIC CHEMISTRY	10
A. Physical Properties of Associating Gases	10
1. Thermal Conductivities of Associating Gases	10
2. <i>Ab Initio</i> Molecular Orbital Calculations	13
B. Chemistry of Molten Salts	17
1. Chemistry of Sulfides in Molten LiCl-KCl Eutectic: Measurements of Solubility Products of Iron Sulfide in Molten LiCl-KCl Eutectic	17
C. Salt Vapor Studies	20
1. Raman Spectra of Indium Halide Vapors and of Indium Aluminum Halide Vapor Complexes	21
2. Resonance Raman Spectra of Pd-Al-Cl and Cu-Al-Cl Vapor Complexes	23
3. Thermodynamics and Spectra of the Co-In-Cl, Pd-In-Cl, and Pd-Al-Br Vapor Complexes	26
4. Halogenation and Separation of Lanthanide Oxides	27
5. Irreversible Thermostructural Transformations in Amorphous As ₂ S ₃ Films	28
D. Thermodynamic Properties of Alloys	30
1. Electromotive Force Measurements and Interpretation of the Activity Coefficients of Lithium in Molten Li-Pb Alloys	30
2. Computation of Phase Diagrams	34
E. Electrochemical Studies	40
1. Metal Deposition/Dissolution Studies	40
F. Meteoritic Studies	42
1. Oxygen Isotopes in Refractory Inclusions in Carbonaceous Meteorites	42
REFERENCES	43
II. CHEMISTRY OF LIQUID METALS	46
A. Thermodynamic Studies of the Sorption of Hydrogen in Lithium-Containing Alloys	46
1. Lithium-Aluminum Alloys	47
2. Lithium-Lead Alloys	48
B. Resistometric Studies of Distribution and Corrosion Phenomena in Liquid-Metal Systems	48

TABLE OF CONTENTS (contd)

	<u>Page</u>
C. Solubility of Lithium Oxide in Liquid Lithium	52
REFERENCES	55
III. THERMOCHEMICAL STUDIES	57
A. Thermochemistry of Coal Components	57
1. Xanthone	57
2. Chromone	58
3. Benzo[b]naphtho[2,3-d]furan	58
4. Estimation of $\Delta H_f^\circ(g)$ and ΔH_{sub} of Xanthone	59
5. Resonance Energy	59
B. Thermochemistry of the Trifluorides of Scandium, Yttrium, Lanthanum and the Rare Earths	62
1. Enthalpies of Formation	62
2. High-Temperature Enthalpy Data	63
C. Uranium Compounds: The Enthalpies of Formation of $\gamma\text{-UO}_3$ and UF_6	65
D. Thermochemical Study of Cs_3CrO_4 and Cs_4CrO_4	67
1. Calorimetric Experiments for Cs_3CrO_4 and Cs_4CrO_4	67
2. Discussion	68
E. The Thermodynamic Properties of the Arsenic Sulfides	69
REFERENCES	73
IV. ENVIRONMENTAL CHEMISTRY	77
A. Chemistry of Airborne Particulate Matter	77
B. Oxygen Isotopy in Atmospheric Sulfate Formation	79
1. Results and Discussions	79
2. Dependence of Oxygen Isotope Effects on Conditions of Sulfur Oxidation	81
C. Sulfur Emissions Control Chemistry	82
1. Dolomite Regeneration Studies: $\text{CaSO}_4\text{-CaS}$ Reaction	82
D. Sulfation Studies: Green River Oil Shale	88
1. Experimental	90
2. Half-Calcination Results	91
3. Sulfation Results	92
4. Discussion	94
REFERENCES	95

TABLE OF CONTENTS (contd)

	<u>Page</u>
V. STRUCTURAL AND SURFACE STUDIES	96
A. Kinetics of Electrochemical Incorporation of Lithium in Solid Alloy Electrodes	96
B. Structural and Morphological Studies on Solid Alloy Electrodes	96
C. Studies of Corrosion in Molten Salt Systems	97
D. Bond Strength-Bond Length Relationships for Metal-Oxygen Bonds	99
REFERENCES	100

LIST OF FIGURES

<u>No.</u>	<u>Title</u>	<u>Page</u>
I-1.	Typical Thermal Conductivity <i>vs.</i> Pressure Isotherms near 370 K for H ₂ O, Trifluoroethanol, and Acetone	11
I-2.	Effect of Pressure on Thermal Conductivity of Acetic Acid at Four Temperatures from 355 to 416 K	13
I-3.	Structures of 2,2,2 Trifluoroethanol	15
I-4.	Optimized Equilibrium Structures for Acetone Dimers	16
I-5.	Variation of ΔE with the Sulfide Mole Fractions at 673, 723, and 773 K	19
I-6.	Experimental and Calculated Vibrational-Rotational Raman Band Contours for InCl(g) and InBr(g)	22
I-7.	Temperature Dependence of Raman Spectra of InAlBr ₄ Vapors	24
I-8.	Temperature Dependence of Absorption Spectra and Excitation Profile at 575 K for Gaseous PdAl ₂ Cl ₈	25
I-9.	Effect of the Intensity of the Excitation Line on the Raman Spectra of the Cu-Al-Cl Gaseous Complexes	26
I-10.	Absorption Spectrum of the Sm ³⁺ -Al-Cl Vapor Complex	28
I-11.	Polarization Unanalyzed Raman Spectra of an Evaporated As-Deposited Film, after Annealing at 180°C for 1 h, and Bulk Glass	29
I-12.	Polarized Raman Spectrum of As ₂ S ₃ Vapors at 600°C	29
I-13.	Variations of $\ln \gamma_{Li}$ and $\ln \gamma_{Pb}$ with the Atom Fraction of Pb at $T = 932$ K	31
I-14.	Variation of the Excess Stability, $ES = \frac{RT}{1 - X_{Li}} \left(\frac{\partial \ln \gamma_{Li}}{\partial X_{Li}} \right),$ with Composition at 932 K	31
I-15.	Calculated Variations of the Partial Structure Factors, $a_{LiLi}(0)$, $a_{LiPb}(0)$, $a_{PbPb}(0)$, and $S_{CC}(0)$ at the Long Wavelength Limit, with Composition	33

LIST OF FIGURES (contd)

<u>No.</u>	<u>Title</u>	<u>Page</u>
I-16.	Computed Isothermal (T = 673 K) Section of the Phase Diagram of the Al-Li-Mg System	36
I-17.	Computed Isothermal (T = 723 K) Section of the Phase Diagram of the Al-Li-Mg System	36
I-18.	Computed Isothermal (T = 773 K) Section of the Phase Diagram of the Al-Li-Mg System	37
I-19.	Computed Isothermal (T = 648 K) Section of the Phase Diagram of the Al-Li-Mg System	37
I-20.	Computed Isothermal (T = 673 K) Section of the Phase Diagram of the Ca-Li-Mg System	38
I-21.	Computed Isothermal (T = 723 K) Section of the Phase Diagram of the Ca-Li-Mg System	39
I-22.	Computed Isothermal (T = 773 K) Section of the Phase Diagram of the Ca-Li-Mg System	39
I-23.	Oxygen Isotope Anomalies in Carbonaceous Chondrites	42
II-1.	Isotherms in the Lithium-Aluminum System	49
II-2.	Comparison of Lithium Activities Measured by Hydridation and Emf Methods	50
II-3.	Stainless Steel Apparatus for Measuring the Resistivity of Liquid Lithium Solutions	51
II-4.	Solubility of Lithium Oxide in Liquid Lithium	54
III-1.	Plot of $(\Delta H_{\text{cryst}})^{1/2}$ vs. Mole Fraction of Cs_2O [ordinate units are $(\text{kJ mol}^{-1})^{1/2}$]	70
IV-1.	Selected Spectra Showing the Variation in the Spectra of Submicron Particles and the Scale of Acidity	78
IV-2.	Variations of $\delta^{18}\text{O}_{\text{SO}_4^{2-}}$ with $\delta^{18}\text{O}_{\text{H}_2\text{O}}$ for Different Methods of Oxidation in the Hydrolysis-Oxidation Mechanism of Sulfate Formation	82
IV-3.	CaSO_4 -CaS Reaction Kinetics at 950°C Using Starting Materials with $\text{SO}_4^{2-}/\text{S}^{2-}$ Mole Ratios of 1.2, but Prepared under Different Conditions	84

LIST OF FIGURES (contd)

<u>No.</u>	<u>Title</u>	<u>Page</u>
IV-4.	Photomicrograph of a Particle Reduced at 800°C with 2% H ₂	85
IV-5.	Effect of Various Mole Ratios of SO ₄ ²⁻ /S ²⁻ on the Kinetics of the CaSO ₄ -CaS Regeneration Reaction at 950°C	86
IV-6.	Photomicrographs of Two Particles from the Same Sample (SO ₄ ²⁻ /S ²⁻ = 1.6)	89
IV-7.	Photomicrograph of a Sulfate-Free Particle after 64% Regeneration	90
IV-8.	Effect of Temperature on the Reaction Kinetics and SO ₂ Evolution for the CaSO ₄ -CaS Regeneration Reaction at 950°C with the Initial SO ₄ ²⁻ /S ²⁻ = 1.5	91
IV-9.	Sulfation Kinetics at 750°C for Half-calcined Oil Shale and Half-calcined 1337 Dolomite	93
V-1.	Cyclic Voltammograms of Cobalt/Oxide in 0.54M Solution of Li ₂ O in LiCl-KCl Eutectic at 450°C	98
V-2.	Cyclic Voltammogram of Copper/Oxide in 0.54M Solution of Li ₂ O in LiCl-KCl Eutectic at 450°C	98
V-3.	Cyclic Voltammogram of Nickel/Oxide in 0.54M Solution of Li ₂ O in LiCl-KCl Eutectic at 450°C	99

LIST OF TABLES

<u>No.</u>	<u>Title</u>	<u>Page</u>
I-1.	Enthalpies and Entropies of Association of Various Dimers	12
I-2.	Least-Squares-Fitted Equation of Electrochemical Voltage of Cell (3) for Dilute FeCl_2 and No Li_2S	18
I-3.	Solubility of Li_2S in LiCl-KCl Eutectic	20
I-4.	Solubility Products of FeS and Standard Free Energies of Solution of FeS in Molten LiCl-KCl Eutectic	20
I-5.	Calculated Solubility Products of Some Sulfides at 700 K	21
III-1.	Calculation of Group Additivity Values	60
III-2.	Heats of Combustion of Resonance Hybrids	61
III-3.	Derived Data from Combustions of Some Lanthanides in Fluorine at 298.15 K	64
III-4.	Derived Results for UF_6 at 298.15 K	67
III-5.	Calorimetric Results and Enthalpy of Formation of Cesium Chromates	68
III-6.	Derived Results for the Arsenic Sulfides at 298.15 K	71
III-7.	Comparison of ΔH_f° Results for Arsenic Sulfides	73
IV-1.	Summary of Kinetic Parameters for $\text{CaSO}_4\text{-CaS}$ Reaction at 950°C	87

CHEMICAL ENGINEERING DIVISION
BASIC ENERGY SCIENCES RESEARCH:
July 1976—September 1977

ABSTRACT

Studies in basic energy science covered many different activities, nearly all of which were designed to gain information required for a better understanding of systems important to national needs in energy and environment. Studies of associating gases included measurements of thermal conductivities and *ab initio* molecular orbital calculations. Raman spectroscopy and spectrophotometry were used to determine thermodynamic and spectroscopic data on salt vapor complexes. Polarized Raman spectra of As_2S_3 thin films and vapors were recorded. Halogenation of lanthanide oxides with aluminum chloride allowed the separation of the resultant chloride complexes by vapor transport. Electrochemical titrations were used to obtain the solubility product of iron sulfide in molten LiCl-KCl eutectic. Solubility products of eleven sulfides in the same eutectic mixture were calculated *a priori*. Galvanostatic techniques were used to study metal deposition/dissolution reactions in molten salts. Activity coefficients of lithium in lithium-lead alloys were determined electrochemically; phase diagrams of ternary alloys of Li-Al-Mg and Li-Ca-Mg were computed. Thermodynamic studies are being made of the sorption of hydrogen by Li-Al and Li-Pb alloys. The study of the solubility of oxygen in liquid lithium was completed. An electric resistance method for measuring distribution properties of nonmetallic elements in binary metallic systems containing lithium is being developed. Calorimetric methods were used to measure standard enthalpies of formation of some coal components, lanthanum and rare earth trifluorides, and $\gamma\text{-UO}_3$, UF_6 , Cs_3CrO_4 , Cs_4CrO_4 , As_4S_4 , and As_2S_3 . High-temperature enthalpy increments were measured for LaF_3 and $\beta\text{-As}_4\text{S}_4$. The acidities of airborne ammonium sulfate-bearing particles from various areas of the U. S. were measured using Fourier-transform infrared spectroscopy. Oxygen isotopy was used to determine the mechanism of formation of particulate sulfates. The effects of the conditions used in the partial reduction of CaSO_4 to CaS on the kinetics of the $\text{CaSO}_4\text{-CaS}$ reaction for dolomite regeneration were explored. The sulfation of Colorado oil shale was studied. Studies were made of the electrochemical incorporation of Li into Al , and of the structural and morphological changes during charge/discharge cycling of Li-Al electrodes. Mechanisms and rates of corrosion of selected metals and alloys in sulfide and oxide solution in molten LiCl-KCl eutectic are being determined using cyclic voltammetry. Bond strength-bond length relationships have been developed and successfully applied to coordination complexes.

SUMMARY

I. PHYSICAL INORGANIC CHEMISTRY

Physical Properties of Associating Gases

Thermal Conductivity of Associating Gases. Thermal conductivity-pressure measurements have been carried out for the following substances in the vapor state: H_2O , D_2O , acetone, 2,2,2 trifluoroethanol (TFE), and acetic acid. The measurements were made using a thick hot-wire cell in the range 0.07-2 atm (7-200 kPa) and 320-416 K. Nearly linear increases of the thermal conductivity with pressure for H_2O , D_2O , acetone, and TFE were analyzed in terms of a monomer-dimer equilibrium. The thermodynamic results are $-\Delta H_2 = 3.63, 3.69, 3.48, \text{ and } 4.75 \text{ kcal/mol}$ (1 kcal = 4.184 kJ) and $-\Delta S_2 = 18.61, 18.58, 15.09, \text{ and } 18.73 \text{ cal/mol}\cdot\text{K}$ for H_2O , D_2O , acetone, and TFE, respectively. The thermal conductivity of acetic acid was greatly enhanced by a large amount of association and exhibited a maximum as a function of pressure. These data were also analyzed in terms of a monomer-dimer equilibrium, with the results being $-\Delta H_2 = 15.55 \text{ kcal/mol}$ (65.1 kJ/mol) and $-\Delta S_2 = 37.7 \text{ cal/mol}\cdot\text{K}$ (157.7 J/mol·K).

Ab Initio Molecular Orbital Calculations. Molecular orbital calculations using the minimal STO-3G basis set were carried out on various structures of the TFE and acetone dimers. The lowest energy TFE dimer ($-\Delta E_2 = 6.46 \text{ kcal/mol}$) was found to contain two $\text{F}\cdots\text{H}$ internal bonds, an $\text{O}-\text{H}\cdots\text{O}$ bond, and an external $\text{F}\cdots\text{H}$ bond involving the same fluorine taking part in the intramolecular bond. The most stable acetone dimer ($-\Delta E = 1.65 \text{ kcal/mol}$) was arranged in such a way as to form two nearly linear $\text{C}-\text{H}\cdots\text{O}$ hydrogen bonds in a closed structure.

Chemistry of Molten Salts

Chemistry of Sulfides in Molten LiCl-KCl Eutectic: Measurements of Solubility Products of Iron Sulfide in Molten LiCl-KCl Eutectic. An electrochemical titration method was used to determine the solubility product of iron sulfide in molten LiCl-KCl eutectic in the temperature range from 673 to 773 K. The cell used in this investigation can be schematized as follows:



Metallographic and X-ray analyses showed that around the equivalence point FeS precipitated. At temperatures below 773 K, as the solution approached saturation with Li_2S , a compound tentatively described as $\text{Li}_6\text{Fe}_{24}\text{S}_{26}\text{Cl}$ (J phase) precipitated as the major phase. At 773 K, a compound Li_2FeS_2 (X phase) was identified. The solubility of Li_2S , the solubility products of FeS , and the related thermodynamic properties were deduced from the data. The chemical stabilities of the J and X phases, which also form in engineering-scale cells, were deduced from the data.

Calculations of the solubility products of eleven sulfides in the LiCl-KCl eutectic were made *a priori*, based on exact

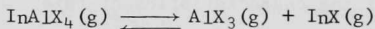
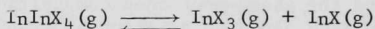
thermodynamic considerations. The results of this calculation for FeS are in close agreement with our measurements, which indicate that FeS is relatively insoluble in the melt.

Salt Vapor Studies

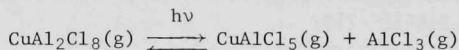
The formation of vapor complexes between volatile "acidic gases" ($A_2X_6 = Al_2Cl_6, Al_2Br_6, In_2Cl_6$ etc.) and a variety of involatile metal halides (MX_p) has been investigated. Simple experiments have shown that the volatility enhancement of the MX_p salt can be used for mass transport, purification, and single crystal growth. It has been recognized that vapor complexes play an important role in the development of new industrial processes designed for energy conservation. Examples are the new process for production of Al via $AlCl_3$ and the construction of high-efficiency lamps. Furthermore, vapor complexes of lanthanides have been considered as lasing materials for the construction of high-power lasers.

Spectroscopic and thermodynamic properties of the vapor and vapor complex species investigated are outlined below:

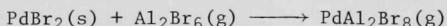
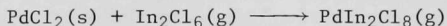
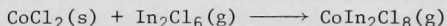
(1) Raman spectra of indium halide vapors over liquid InX_n ($X = Cl, Br; n = 1, 2, 3$) and of vapors over liquid $InAlX_4$ have been measured. At elevated temperatures, $InInX_4$ and $InAlX_4$ dissociate according to the reactions:



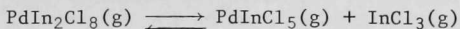
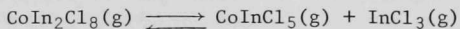
(2) Resonance Raman spectra of $PdAl_2Cl_8$ and $CuAl_2Cl_8$ vapor complexes show similar structures for both molecules. The effect of aluminum chloride pressure and the intensity of the laser line on the spectra of the Cu-Al-Cl complex(es) indicate two predominant copper-containing species in equilibrium



(3) Spectrophotometric measurements were used to determine the stoichiometry and thermodynamics of the following reaction:



Molar absorptivity and vapor pressure measurements suggest that the predominant vapor species at temperatures above 900 K are $CoInCl_5$ and $PdInCl_5$ and that the following equilibria occur:



(4) Lanthanide oxides have been halogenated using AlX_3 (liquid or vapor; $X = Cl$ or Br) at temperatures above 450 K. Vapor transport of the lanthanide chlorides has been used to separate them. Spectrophotometric measurements have determined that the vapor transport occurs through the formation of vapor complexes of the type $SmCl_3 \cdot 3AlCl_3$.

(5) Polarized Raman spectra of As_2S_3 thin films and vapors have been recorded. Irreversible thermostructural transformations have been found to occur in the evaporated thin films. Vapor spectra over liquid As_2S_3 indicate the presence of several molecular species in the gas phase.

Thermodynamic Properties of Alloys

Electromotive Force Measurements and Interpretation of the Activity Coefficients of Lithium in Molten Li-Pb Alloys. Electromotive force measurements of the activity of lithium in lithium-lead liquid alloys are reported in the temperature range from 770 to 932 K. The partial molar excess Gibbs free energies are negative. Variations with composition exhibit an inflection point around a mole ratio of lithium to lead of 4, which corresponds to the ratio of the valences of Pb to Li. The inflection point, as well as structural data, may be interpreted by assuming an at least partly ionic character of the alloy. A set of partial structure factors are calculated as a function of the composition at the long wavelength limit. Their variations support the hypothesis of a local short-range order around the above-mentioned composition (Li/Pb ratio of 4). Finally, a modeling approach based on an electron transfer from Li to Pb is used to explain some of the characteristics of this class of alloys.

Computation of Phase Diagrams. The phase diagrams of the ternary Al-Li-Mg and Ca-Li-Mg systems have been computed from the lower order subsystems. Isothermal sections have been calculated at temperatures of interest for high-temperature and high-energy batteries. A knowledge of the phase relations of such systems is a significant aid in selecting electrode materials and in understanding the interactions occurring between the electrode and the electrolyte.

Electrochemical Studies

Metal Deposition/Dissolution Studies. A systematic study is being made of metal deposition/dissolution reactions in molten alkali halides which are important elementary steps in molten-salt batteries (such as the $LiAl/FeS_x$ batteries) and also in metalwinning from molten salts. The kinetics and mechanisms of the electrode reactions are being investigated in order to gain a fundamental understanding of electrode behavior in molten salts. The first system to be investigated is iron in $LiCl-KCl$ eutectic. Initial measurements using the single-pulse galvanostatic technique have shown that the reaction rate is too high for this technique ($i_0 \gtrsim 10 \text{ A/cm}^2$ at 450°C and at $7.7 \times 10^{-6} \text{ mol Fe}^{2+}/\text{cm}^3$). Before using the double-pulse method, which has been used for measurement of fast reactions, theoretical work was carried out to eliminate certain weaknesses of the technique for its present usage. A modified technique was devised in which the problem caused by the inevitable inductive spike and ringing of the potential signal close to the beginning of the pulse was circumvented; this will allow the measurement of rate constants

that are at least one order of magnitude larger than those measurable with the single-pulse method. The theory was also extended to allow the treatment of a generalized multistep reaction scheme. The original theory was applicable only to reactions in which all electrons were transferred in the rate-determining step. A detailed error analysis was also carried out that took into account the nonideal behavior of the pulse generators (finite rise time). It was shown that rise times larger than 100 nsec will introduce considerable errors, but a calculational method can be applied in which the errors caused by the finite rise times of the first and second pulses will largely cancel. This is an added, and up to now, an unknown advantage of the double-pulse method.

Meteoritic Studies

Oxygen Isotopes in Refractory Inclusions in Carbonaceous Meteorites.
A diffusion model that was proposed by us for the interpretation of oxygen isotope anomalies in refractory inclusions in carbonaceous chondrites appears to be consistent with the observations of Clayton *et al.*, and negates most of the earlier speculations concerning the extra-solar or pre-solar origins of these anomalies.

II. CHEMISTRY OF LIQUID METALS

Thermodynamic Studies of the Sorption of Hydrogen in Lithium-Containing Alloys

A new method is presented for studying the thermodynamic and phase relations of binary, lithium-containing alloys by reacting them with controlled quantities of hydrogen gas. Lithium in the alloy reacts with hydrogen to form solid LiH, thereby changing the composition of the alloy in proportion to the amount of hydrogen added. The advantages of the method are twofold: (1) it provides information on the composition of intermediate phases and (2) it permits the calculation of lithium activity as a function of alloy composition from the measured hydrogen decomposition pressures and the standard free energy of formation of solid LiH. Current status of applications to the Li-Al and Li-Pb systems is described.

Resistometric Studies of Distribution and Corrosion Phenomena in Liquid Metal Systems

A project has been initiated to investigate ternary systems of the form, Li-M-X, where M is a transition metal and X is a nonmetallic element, such as nitrogen, oxygen or carbon. The project is aimed at increasing knowledge of lithium corrosion of structural metals by examining selected aspects of the solution behavior of the nonmetallic elements in the two metal phases. A parameter of prime importance in such a study is the distribution coefficient of the nonmetallic element--the quantity these experiments are designed to measure. The experimental method used for probing the ternary system will be to measure changes in the electrical resistivity of the liquid lithium phase as a function of nonmetallic element concentration and temperature. The experimental apparatus and operating procedures for the resistivity experiments are described.

Solubility of Lithium Oxide in Liquid Lithium

The solubility of lithium oxide in liquid lithium has been measured by a direct sampling technique. Filtered samples of saturated solutions were taken at 28 temperatures ranging from 195 to 734°C and were analyzed for oxygen by a fast-neutron activation method. The solubility can be represented by the equations

$$\ln S = 6.054 - 6669 T^{-1}$$

$$\log S^* = 6.992 - 2896 T^{-1}$$

where S is in mole percent Li_2O and S^* is in weight parts per million (wppm). The theoretical limit of oxygen removal by cold trapping at 200°C is indicated to be ~ 7 wppm, although it is suggested that this limit could only be attained by filtration through filters of fine pore size (2 μm or less).

III. THERMOCHEMICAL STUDIES

Thermochemistry of Coal Components

The energies of combustion of solid xanthone ($\text{C}_{13}\text{H}_8\text{O}_2$), chromone ($\text{C}_9\text{H}_6\text{O}_2$), and benzo[b]naphtho[2,3-d]furan ($\text{C}_{16}\text{H}_{10}\text{O}$) were measured by oxygen bomb calorimetry and their standard enthalpies of formation calculated. The heat of sublimation of xanthone was estimated by analogy with compounds of related structure in order to obtain the heat of formation of gaseous xanthone. A system of group additivity values was developed to permit estimation of the heat of formation in the gaseous state, and ultimately the resonance stabilization of such compounds. Interpretations of such calculations suggest that the xanthone molecule is planar and aromatic.

Lanthanum and the Rare Earth Trifluorides

Bomb calorimetric measurements of the energy of combustion of La, Nd, Er, Gd, Dy and Ho in fluorine have yielded enthalpies of formation for the trifluorides of each of these elements. The enthalpy data are in accord with those expected for the rare earths. High-temperature drop-calorimetry data for LaF_3 have corrected discrepancies that existed in the literature between low-temperature heat capacity data and prior high-temperature measurements.

Uranium Compounds

Recent assessment of the thermochemistry of selected uranium compounds suggests that published enthalpy values for $\gamma\text{-UO}_3$ and UF_6 may be in error. Solution calorimetric measurements on $\gamma\text{-UO}_3$ affirmed published values; however, a redetermination of the $\Delta H_f^\circ(\text{UF}_6, \text{c})$ by fluorine bomb calorimetry showed earlier results to be in error by about 10 kJ mol^{-1} .

Cs₃CrO₄ and Cs₄CrO₄

The enthalpy changes of the reactions of Cs₃CrO₄ and Cs₄CrO₄ with XeO₃/CsOH solutions were measured by solution calorimetry and the standard enthalpies of formation were calculated. The lattice energy is discussed for the Cs-Cr-O system and an estimate of the standard enthalpy of formation of Cs₅CrO₄ is given.

Arsenic Sulfides

Combustions of As₄S₄ and As₂S₃ were carried out in a fluorine bomb calorimeter. In both cases the products were AsF₅ and SF₆. These studies yielded ΔH_f° values at 298.15 K and served to clarify the large discrepancies that have existed for some time in the scientific literature.

IV. ENVIRONMENTAL CHEMISTRY

Chemistry of Airborne Particulate Matter

A procedure developed at ANL for sampling and analyzing airborne particulate matter is described. A modified Lundgren impactor is used to collect time- and size-resolved samples of the particles. The collected samples are analyzed by Fourier-transform infrared spectroscopy for quantitative determination of nitrate and neutral ammonium sulfate, and for qualitative determination of the degree of acidity of the ammonium sulfates. From well over a thousand samples collected in the Midwest, near Chicago, IL, and St. Louis, MO, it has been found that ammonium sulfates are the predominant constituents of the submicrometer particles, that the acidity of the ammonium sulfate varies with time, and that regional episodes of acidic sulfate sometimes occur. Several hundred samples taken from eastern sites, near State College, PA, and Charlottesville, VA, have shown a very much larger occurrence of acidic sulfate, both in the degree of acidity and in its frequency of occurrence. This frequent occurrence of acidic ammonium sulfate aerosols in the eastern atmospheres has not been reported previously.

Oxygen Isotopy in Atmospheric Sulfate Formation

It has been determined from oxygen isotope ratio analyses that sulfate in precipitation water (rain and snow) is most likely formed from SO₂ by the hydrolysis-oxidation mechanism. The SO₂ dissolves in a large excess of liquid water (cloud droplets) and the resulting HSO₃⁻ ion undergoes rapid oxygen isotope equilibration with the water. It is then oxidized to SO₄²⁻ which thus has an isotopic quality corresponding to three oxygen atoms contributed by the water. Precipitating clouds transfer the freshly formed sulfate to the earth's surface as rain or snow.

It is postulated that atmospheric particulate sulfate is also formed by the same hydrolysis-oxidation mechanism of SO₂ conversion in cloud droplets, but is not captured by the precipitation. Evaporation of the host cloud droplets leaves a residue of the particulate sulfate. This aerosol sulfate has a relatively long time of residence in the atmosphere, during which time it may experience extensive transport and mixing with sulfates in other air masses, thus obscuring any systematic variations.

As observed for samples collected at Argonne, the $\delta^{18}\text{O}$ values for particulate sulfate sampled at San Diego, CA, also did not show any specific seasonal trends. However, their 12-month average value for 1975 was 4.4 ‰ higher than that of the sulfate at Argonne. A plausible explanation for the higher $\delta^{18}\text{O}$ in San Diego samples is that the average atmospheric water is richer in $\delta^{18}\text{O}$ in the lower latitude of San Diego than in the higher latitude of Argonne.

Results of laboratory experiments on the hydrolysis-oxidation of SO_2 indicated that the number of oxygen atoms contributed by water to the product sulfate varies at least between 2.5 to all 4, depending upon the method of oxidation, *e.g.*, the oxidizing agent employed.

Sulfur Emissions Control Chemistry

In basic research on sulfur sorbent chemistry, studies are being conducted on the interrelationships between the sorbent structure and morphology and its chemical reactivity. The sorbents under study include BCR 1337 dolomite, synthetic dolomites, alternative natural sorbents, and Colorado oil shale.

For the BCR 1337 dolomite, the CaSO_4 -CaS regeneration reaction for producing CaO has been studied further. It had been established earlier that the extent of this reaction is governed by the $\text{SO}_4^{2-}/\text{S}^{2-}$ mole ratio in the starting material which is prepared by the partial reduction of the sulfated dolomite with hydrogen. Recently, experiments have been conducted to determine the effects of the reduction reaction conditions (reaction temperature, hydrogen concentration) on the yield of CaO obtained. Additional information has been obtained on the kinetics of the partial reduction and regeneration reactions, the gases evolved during the reactions, and the morphologies of the reactants and the products. It was observed that, in general, reducing the sulfated dolomite at relatively low rates (low temperature and/or low H_2 concentrations in the reducing gas mixture) gave a higher yield of CaO from the CaSO_4 -CaS reaction. The kinetic studies showed that, while the CaO yield varied depending upon the composition of the partially reduced materials, in each case the reaction was 80% complete in about 20 min.

Colorado oil shale has a relatively large content of calcium and magnesium carbonates. Shale from the Green River formation was used in our study to evaluate its sulfation characteristics. It was found that although the spent oil shale contains less calcium carbonate than the BCR 1337 dolomite, it has a greater sulfur retention capacity than the dolomite when each is reacted with SO_2 for 3 hr or less. This was shown to be due to the substantial sulfation of the Mg in the shale; the Mg in dolomite has previously been determined to be mostly inactive for sulfation. The sulfation of half-calcined spent oil shale proceeds faster than that of dolomite; this has been attributed to the larger pore sizes and pore volume and the smaller grain sizes in the shale than in the dolomite. Overall, the spent oil shale was found to be superior to dolomite as a sulfur sorbent for sulfation times of up to 3 hr.

V. STRUCTURAL AND SURFACE STUDIES

Kinetics of Electrochemical Incorporation of Li in Solid Alloy Electrodes

The electrochemical incorporation of Li into Al wire electrodes at 450°C was investigated by chronocoulometric, galvanostatic and potentiostatic techniques. The rate-limiting processes at low and high current densities were determined. Values of Li diffusivity in the α - and β -LiAl phases were obtained.

Structural and Morphological Studies on Solid Alloy Electrodes

Electrochemical and crystal chemical investigations of the Li-Al electrode were made to gain a better understanding of the kinetic behavior and the origin of structural and morphological changes during charge and discharge. Based on these studies, a Li-Al-Mg ternary electrode is being developed and its properties are presently being studied.

Studies of Corrosion in Molten Salt Systems

The FeS and J-sulfide phases have been produced by anodic sulfidation of iron in molten LiCl-KCl eutectic and are being characterized by Mössbauer spectroscopy. The anodic oxidation behavior of Co, Cu, and Ni is being examined; the oxides of these metals appear to be potentially useful as cathode materials.

Bond Strength-Bond Length Relationships for Metal-Oxygen Bonds

A bond strength-bond length relationship has been formulated utilizing structural data of uranyl salts as a basis. The bond distance D is given by $D = A + K/S$, where A and K are cation and anion covalent radii, respectively, and S is the bond strength. The expression has been derived explicitly and is applicable to S between 1 and 2. However, if it is assumed that the Pauling D-S relation can be expanded and a coordination correction added, then it can be shown that $D = \alpha - \beta S^x$ where α , β , and x are readily evaluated. Refinement of the evaluated quantities leads to reasonable D-S relationships for all S (or D) values.

I. PHYSICAL INORGANIC CHEMISTRY

(M. Blander, D. J. Frurip, L. Curtiss, M. L. Saboungi,
J. J. Marr, G. H. Kucera, G. N. Papatheodorou,
C. C. Hsu, and Z. Nagy)

A. Physical Properties of Associating Gases

Because of the relative simplicity of vapor species, fundamental studies of the character and strengths of bonding between vapor molecules can be performed in an unambiguous manner. Thus, a study of association constants can lead to definitive values of bond strengths. In addition a substance that associates in the gas phase to form molecular aggregates has special physical properties that make it potentially useful as a working fluid in power cycles. This is partly due to the enhancement of the thermal conductivity and heat capacity of the gas, which can lead to substantially improved heat exchange and thermodynamic properties. Measurements of the thermal conductivity of a number of associating vapors have been carried out to (1) characterize the types (size) of polymers present and gain a fundamental understanding of the factors which influence bond strength, (2) accurately determine the thermodynamics of the individual association reactions and hence the extent of such reactions, and (3) determine the magnitude of the thermal conductivity augmentation.

1. Thermal Conductivities of Associating Gases
(D. J. Frurip and L. Curtiss)

The pressure and temperature dependence of the thermal conductivity of a gas can be analyzed to determine what associated species are present. In this work, expressions developed by Butler and Brokaw¹ are used. The thermal conductivity of an associating gas is given by

$$\lambda = \lambda_f + \lambda_R \quad (1)$$

where λ_f is the thermal conductivity of the frozen (nonreacting) mixture of all the vapor species and λ_R is the enhancement of the thermal conductivity due to formation of associated species. The λ_f is generally weakly dependent on pressure, whereas the λ_R is strongly dependent on pressure. When monomers and dimers are present in the vapor, Eq. 1 has the form

$$\lambda = \lambda_f + \left(\frac{pD_{12}}{RT} \right) \left(\frac{\Delta H_2^0}{RT^2} \right) \left(\frac{K_2 p_1}{(1 + 2K_2 p_1)^2} \right) \quad (2)$$

where pD_{12} is the pressure-binary diffusion coefficient, ΔH_2^0 is the enthalpy of association of the dimer, K_2 is the equilibrium constant for formation of the dimer, and p_1 is the pressure of the monomer.

Thermal conductivity measurements and analyses of the data in terms of the associated species present have been carried out for five substances: H_2O , D_2O , 2,2,2 trifluoroethanol, acetone, and acetic acid. These substances were chosen for measurement in order to gain insight into their bonding characteristics (especially those of the hydrogen bonds), and to obtain data to help find suitable candidates for working fluids.

The thermal conductivity of water vapor was measured in a thick hot-wire cell^{2,3} at four temperatures between 358 K and 386 K and pressures up to 1400 torr (187 kPa). The plots of thermal conductivity *vs.* pressure were nearly linear, with approximately a 3% slope per atmosphere (101 kPa) of pressure (see Fig. I-1). The near linearity of the plots indicates that

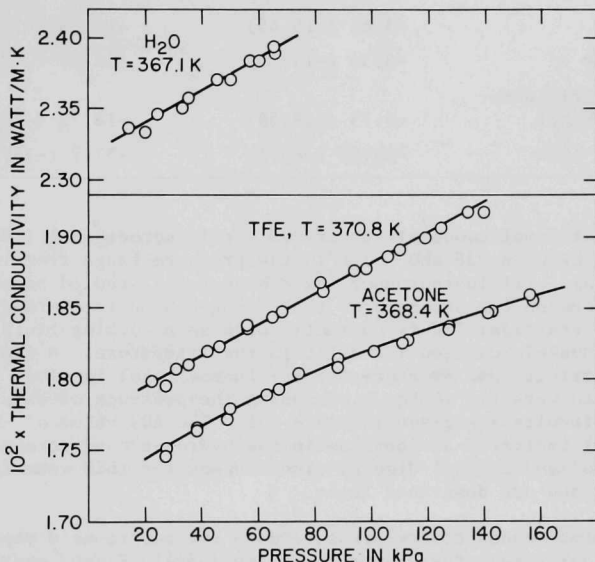


Fig. I-1. Typical Thermal Conductivity *vs.* Pressure Isotherms near 370 K for H₂O, Trifluoroethanol (TFE), and Acetone. (The theoretical fit to the data points is represented by the solid lines. Refer to Table I-1 for the thermodynamic results on the dimers.)

the associated species were mainly dimers and, hence, the data were fit to Eq. 1 assuming that only monomers and dimers were present. The results are given in Table I-1. The enthalpy of association of -3.63 ± 0.5 kcal/mol (-15.2 kJ/mol) for the water dimer is in reasonable agreement with the best theoretical calculations, which indicate that ΔH_2 is between -3.75 and -4.20 kcal/mol (-15.7 and -17.6 kJ/mol).

Thermal conductivity measurements were carried out on D₂O vapor to determine the effect of isotopic substitution on dimer formation. The results in Table I-1, indicate that the effect is small. The ΔH_2 value for (D₂O)₂ is -3.69 kcal/mol (-15.44 kJ/mol) as compared with -3.63 kcal/mol (-15.2 kJ/mol) for (H₂O)₂; however, this comparison may not be meaningful because of uncertainties in the numbers.

Table I-1. Enthalpies and Entropies of Association of Various Dimers

Species	ΔH_2 , kcal/mol (kJ/mol)	ΔS_2 , cal/mol·deg (J/mol·K)
H ₂ O	-3.63 (-15.20)	-18.61 (-77.86)
D ₂ O	-3.69 (-15.45)	-18.58 (-77.74)
Acetone	-3.36 (-14.09)	-15.07 (-63.10)
2,2,2 Trifluoro- ethanol	-4.75 (-19.89)	-18.73 (-78.36)
Acetic Acid	-15.55 (-65.1)	-37.7 (-157.7)

The thermal conductivity of 2,2,2 trifluoroethanol (TFE) vapor has been measured between 338 and 385 K in the pressure range from 100 to 1400 torr (13 to 190 kPa). Trifluoroethanol was chosen to be studied because the effect of the fluorines on the strength of the hydrogen bond is of fundamental interest. In addition, TFE is currently used as a working fluid and very little thermodynamic data on TFE exist in the literature. A typical plot of thermal conductivity *vs.* pressure for trifluoroethanol is given in Fig. I-1. Again, the data were fit to Eq. 1, assuming the presence of only monomers and dimers. The results are given in Table I-1. The ΔH_2 value of -4.75 kcal/mol (-19.9 kJ/mol) indicates an increase in the hydrogen bond strength over that in the methanol and ethanol dimers. The reasons for this were investigated theoretically and are described later.

Thermal conductivity-pressure data for acetic acid vapor have been obtained at four temperatures over the range 355-416 K, and over the pressure range 0-2 atm (0-200 kPa). The data were acquired in a newly built apparatus capable of operation at higher temperatures (~ 500 K) and pressures (~ 5 atm). Available data on acetic acid show it to be strongly dimerized at room temperature and normal pressures.⁴ For such a substance, Eq. 1 predicts a maximum λ_R when $p_2/p_1 = 1/2$. The experimental data, shown in Fig. I-2, exhibit maxima that are indicative of large amounts of association. A fit of the experimental data, assuming a monomer-dimer equilibrium, was performed as previously described and is represented by the solid lines in Fig. I-2. The experimental points are reproduced well by the theoretical fit. The dimer thermodynamic results are $\Delta H_2 = -15.55 \pm 0.20$ kcal/mol (-65.1 kJ/mol) and $\Delta S_2 = -37.7 \pm 0.5$ cal/mol·K (-157.7 J/mol·K).

It is interesting to note the extremely large absolute values of the thermal conductivity for acetic acid because of the reaction enhancement. At 385 K, acetic acid possesses a thermal conductivity that is $\sim 45\%$ larger than that of neon gas. This large augmentation is similar to that observed with NO₂ gas owing to the $2\text{NO}_2 \rightleftharpoons \text{N}_2\text{O}_4$ equilibrium.⁵ Thus, the potential use of acetic acid (or some derivative) as a working fluid is conceivable.

The thermal conductivity of acetone vapor was measured at four temperatures in the range from 341 to 378 K and pressures up to 1200 torr (160 kPa). A typical isotherm from our data, as shown in Fig. I-1, is

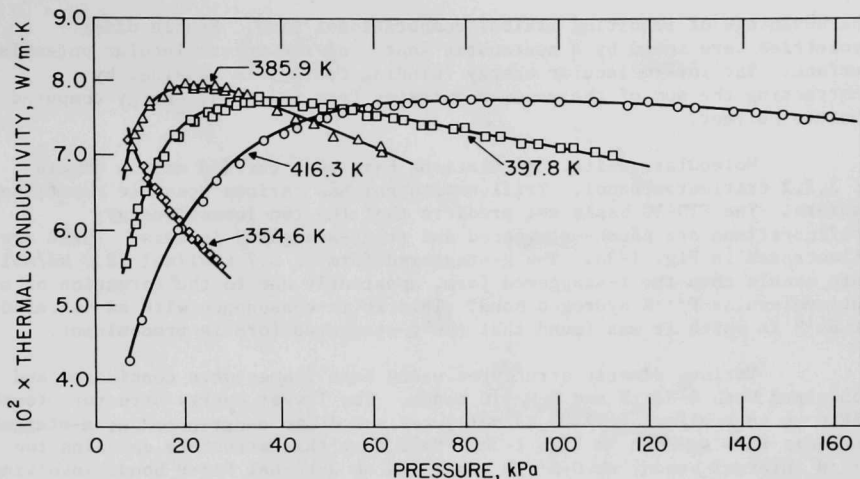


Fig. I-2. Effect of Pressure on Thermal Conductivity of Acetic Acid at Four Temperatures from 355 to 416 K. (The theoretical fit to the data is represented by the solid lines. The best fit thermodynamic data are $-\Delta H_2 = 65.1$ kJ/mol and $-\Delta S_2 = 157.7$ J/mol·K. The maximum for the 354.6 K curve is not shown because it was observed near 3.3 kPa, a region wherein the data are considered to be unreliable.

nearly linear but with a slight regressive curvature at the higher pressures. This behavior is again indicative of a predominantly monomer-dimer equilibrium⁶ but in this case the denominator term $(1 + 2K_2P_1)^2$ in Eq. 2 is large enough to cause the slight curvature in the thermal conductivity *vs.* pressure isotherms. No higher polymers are indicated by the data. The theoretical fit to the data (Eq. 2) was excellent (Fig. I-1), with the results (Table I-1) being $-\Delta H_2 = 3.48 \pm 0.4$ kcal/mol (14.6 kJ/mol) and $-\Delta S_2 = 15.09 \pm 0.20$ cal/mol·deg (63.1 J/mol·K). Thus the acetone dimers appear to be fairly strongly bound entities. Evidence for conventional hydrogen or dipole-dipole bonding in the dimers studied was sought out theoretically and is discussed below.

2. Ab Initio Molecular Orbital Calculations (L. Curtiss and D. J. Frurip)

In order to gain a better understanding of the association process, we performed *ab initio* molecular orbital calculations on various dimeric structures of TFE and acetone. The results of these calculations provide a basis for comparison of the experimentally determined association enthalpy and yield insight into the nature of the hydrogen bonding in these species. Standard LCAO-SCF methods were utilized in this study using the minimal STO-3G basis set. This small basis set has been found to give valid geometries and binding energies for hydrogen-bonded complexes⁷⁻⁹ and has

the advantage of requiring minimal computational time. Stable dimer geometries were found by a systematic search of the intermolecular potential surface. The intermolecular energy (binding energy) is obtained by subtracting the sum of the monomer energies from the total energy computed for the polymer.

Molecular orbital calculations have been carried out on dimers of 2,2,2 trifluoroethanol. Trifluoroethanol has various possible rotational isomers. The STO-3G basis set predicts that the two lowest energy configurations are gauche-staggered and trans-staggered isomers. These are illustrated in Fig. I-3a. The g-staggered form is 0.7 kcal/mol (2.9 kJ/mol) more stable than the t-staggered form, apparently due to the formation of an intramolecular $F\cdots H$ hydrogen bond. This is in consonance with an infrared study¹⁰ in which it was found that the g-staggered form is predominant.

Various dimeric structures using each isomer were considered and contained both $O-H\cdots F$ and $O-H\cdots O$ bonds. The lowest energy structure found [$\Delta E = -6.46$ kcal/mol (-27.03 kJ/mol)] was the dimer constructed of g-staggered monomers and is shown in Fig. I-3b. Note that this structure contains two $F\cdots H$ internal bonds, an $O-H\cdots O$ bond, and an external $F\cdots H$ bond, involving the same fluorine that is taking part in the intramolecular bond.

Experimentally the trifluoroethanol dimer is found to be more stable by about 1 kcal/mol (4.18 kJ/mol) than the ethanol dimer. The theoretical calculations indicate that this is primarily due to the extra hydrogen bond ($F\cdots H$) that is formed in the dimer. Also, the presence of an intramolecular hydrogen bond provides a possible explanation for the fact that tetramers are not observed in trifluoroethanol vapor as they are in methanol and ethanol vapors.^{2,11}

The acetone monomer geometry has been previously optimized with the STO-3G basis set.¹² A search of the intermolecular potential surface yielded the two stable dimer geometries shown in Fig. I-4. In both structures, the $C=O$ dipoles are aligned in nearly opposite directions. In structure A, the CCC molecular planes are slightly nonparallel with a STO-3G binding energy of -0.98 kcal/mol (-4.10 kJ/mol). Note that the $C=O$ group in molecule I is directed slightly toward the protons that are trans to the oxygen in molecule II and may be an indication of some hydrogen bonding.

Structure B in Fig. I-4 is the second stable acetone dimer. In this case, the carbon and oxygen atoms in both molecules are coplanar, forming a closed structure. Also, the dimer is symmetric about an axis perpendicular to the molecular planes. The binding energy for this structure of -1.65 kcal/mol (-6.90 kJ/mol) is nearly double that of structure A. This increase is due to the formation of two linear hydrogen bonds as indicated by the dashed lines in structure B of Fig. I-4. Note, however, that this calculated binding energy is still less negative than the most recent experimental enthalpy of dimerization, $-\Delta H_2$ of ~ 3.5 kcal/mol (see above). The dipole moment for the acetone monomer as determined with the STO-3G basis set is nearly 1 D less than the experimental value of 2.9 D. Therefore, the use of a basis set which better represents the electronic distribution and, hence, provides a more realistic dipole moment would be needed to decrease the discrepancy between theory and experiment.

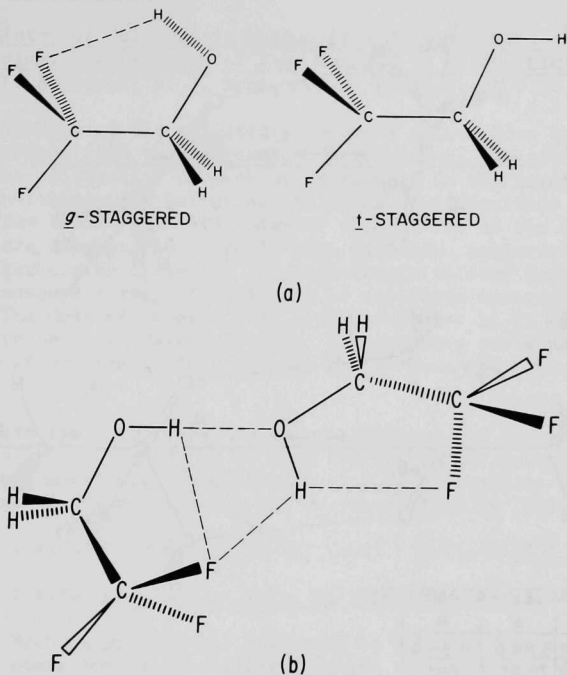
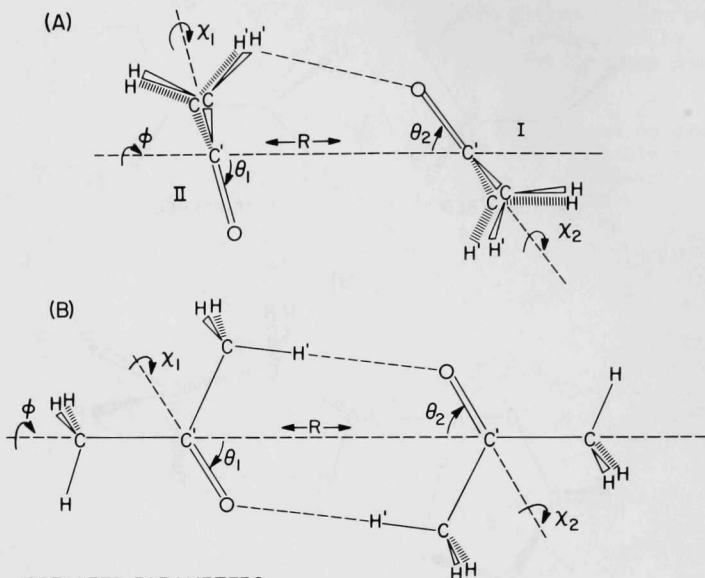


Fig. I-3. Structures of 2,2,2 Trifluoroethanol (TFE):
 (a) Rotational Isomers of TFE Monomer; (b)
 Lowest Energy TFE Dimer. [The STO-3G
 binding energy of this dimer is
 -6.46 kcal/mol (-27.0 kJ/mol).]



OPTIMIZED PARAMETERS

	A	B
R	3.84 Å	4.65 Å
θ_1	76.6°	58°
θ_2	53.5°	58°
X_1	90°	0°
X_2	90°	0°
ϕ	180°	180°

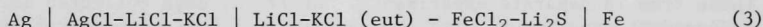
Fig. I-4. Optimized Equilibrium Structures for Acetone Dimers. [The intermolecular geometry was represented by the coordinate system shown in structure A. The ST0-3G binding energies are -0.98 and -1.65 kcal/mol (-4.10 and -6.90 kJ/mol) for A and B, respectively. Note that in structure A the protons cis to the carbonyl oxygen have been omitted for clarity.]

B. Chemistry of Molten Salts

1. Chemistry of Sulfides in Molten LiCl-KCl Eutectic: Measurements of Solubility Products of Iron Sulfide in Molten LiCl-KCl Eutectic (M. L. Saboungi, J. J. Marr, and M. Blander)

Predictions of the solubility products of sulfides in molten salts can be made *a priori* from thermodynamic considerations. Measurements were made to test the reliability of such predictions. In the development and testing of high-temperature batteries utilizing iron disulfide (FeS_2) as electrode and the molten LiCl-KCl eutectic composition as the electrolyte, some problems are encountered in cells that have been subjected to extensive charging and discharging cycles.¹³ One hypothesis relates these problems to chemical transport through dissolution of electrode materials in the electrolyte. The determination of the solubilities of Li_2S , FeS and FeS_2 are important to resolve these problems. Consequently our studies should provide a test of our predictions as well as new data of technological significance.

At this time, we report on an experimental and theoretical investigation of the solubilities of Li_2S and FeS in the molten LiCl-KCl eutectic in the temperature range of operation of the battery ($T = 673\text{--}773\text{ K}$). The cell used in this investigation can be schematized as follows:



a. Dilute Solutions of FeCl_2 in LiCl-KCl Eutectic

Each experiment was initiated by checking the behavior of the iron electrode since the silver-silver chloride electrode has proven to be reversible. For dilute solutions of FeCl_2 in the LiCl-KCl eutectic, the emf's vary with composition according to the relation:

$$E = E_4^0 - \frac{RT}{2F} \ln a_{\text{FeCl}_2} \quad (4)$$

where E is the true electrochemical voltage of cell (3); R , the gas constant; F , the Faraday constant; a_{FeCl_2} , the activity of iron chloride in solution; and E_4^0 , the limiting potential of FeCl_2 in the LiCl-KCl eutectic melt *versus* the silver-silver chloride electrode. For each temperature, a least-squares fit of the data leads to slopes in excellent agreement with the theoretical slopes of $2.3026 RT/2F$ (Table I-2). At 723 K, combining our value for E_4^0 with that of the standard formation potential of AgCl in the LiCl-KCl eutectic^{14,15} and making the appropriate corrections, we calculate 1.382 V for the standard formation potential of FeCl_2 in the LiCl-KCl eutectic melt, which is in reasonable agreement with the value of 1.387 V measured by Laitinen and Liu.¹⁵

Table I-2. Least-Squares-Fitted Equation of Electrochemical Voltage of Cell (3) for Dilute FeCl_2 and No Li_2S :

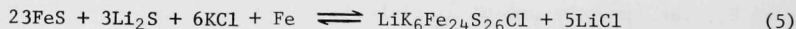
$$E = E_4^0 - m \log X_{\text{Fe}^{2+}}$$

T, K	$m(\text{Theor.}) = \frac{2.3026 RT}{2F}$, mV	$m(\text{Exp.})$, mV	E_4^0 , mV
673	66.77	66.43 ± 0.13	256.66 ± 0.50
723	71.73	71.18 ± 0.18	231.58 ± 0.67
773	76.69	76.95 ± 0.22	209.09 ± 1.85

b. Titration of FeCl_2 with Li_2S

Successive additions of Li_2S were made to FeCl_2 solutions to precipitate sulfides. In Fig. I-5, the differences in the emf's (emf of cell (3) - emf of cell (3) with $X_S = 0$) are plotted *versus* the total sulfide added; the three titration curves shown at 673, 723 and 773 K are typical of those from 18 separate experiments. At 773 K, data collected in two independent experiments with the same initial FeCl_2 concentration are plotted to show the reproducibility of the measurements (Fig. I-5).

In order to identify the black precipitate which formed, samples were separately prepared by equilibration with the melt and submitted for X-ray and metallographic analysis. Three different phases were found depending on the temperature and the composition of the solution. Well before the solution became saturated with Li_2S , FeS was the only precipitate to be identified in the temperature range of this study. As the solution approached saturation, two other sulfide phases were identified. At 673 and 723 K, the major phase in these precipitates consisted of the mineral djerfisherite (also called J phase) which has a composition tentatively described as $\text{LiK}_6\text{Fe}_{24}\text{S}_{26}\text{Cl}$.¹⁶ A possible reaction occurring in the solution is



This complex compound which forms on the iron sulfide electrode in engineering-scale cells is highly undesirable because it slows the kinetics of the cell reaction to a considerable extent.¹⁶ At 773 K, for solutions approaching saturation with Li_2S , a phase commonly referred to as X phase ($=\text{Li}_2\text{FeS}_2$) has been identified by analyses.

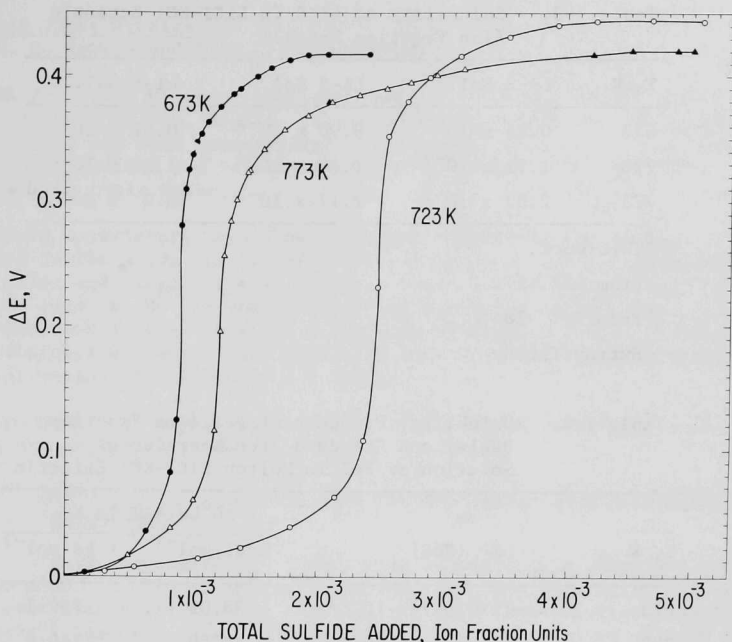
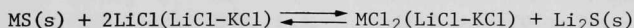


Fig. I-5. Variation of ΔE with the Sulfide Mole Fractions at 673, 723, and 773 K (The initial mole fractions of FeCl_2 were 0.926×10^{-3} , 2.402×10^{-3} , and 1.233×10^{-3} , respectively.) ANL Neg. No. 308-77-349

c. Calculations from the Data

One can derive the solubility of Li_2S in the LiCl-KCl eutectic from the titration curves by knowing the chemical nature of the precipitate. Our results, given in Table I-3, differ from some of the earlier measurements;^{17,18} however, the temperature dependence is similar. The solubility products of FeS were computed by (1) taking into account the possible existence of a limited solid solution of Li_2S in FeS ¹⁹ or (2) neglecting any solid solubility. The values obtained for K_{sp} (Table I-4) were not significantly affected by either hypothesis. The standard Gibbs free energy of solution of FeS ($-RT \ln K_{\text{sp}}$) can be calculated *a priori* from exact thermodynamic considerations²⁰ based on the analysis of the reaction



where M can be iron or other metals. Using known data on free energies of formation, the formation potential of MCl_2 , the solubility of Li_2S , and the solution properties of LiCl , we obtained a value of 38.38 kcal/mol for $-RT \ln K_{\text{sp}}$, which is in good agreement with the measurements.²¹

Table I-3. Solubility of Li_2S in LiCl-KCl Eutectic (Ion Fraction Units)

T, K	Li_2S Sol. ^a	Li_2S Sol. ^b	Li_2S Sol. ^c
673	0.86×10^{-3}	0.90×10^{-3}	0.67×10^{-3}
723	1.51×10^{-3}	1.49×10^{-3}	1.29×10^{-3}
773	2.52×10^{-3}	2.17×10^{-3}	$(2.0 \times 10^{-3})^d$

^aThis work.^bFrom Ref. 17.^cFrom Ref. 18.^dExtrapolated.Table I-4. Solubility Products of FeS (Ion Fraction Basis) and Standard Free Energies of Solution of FeS in Molten LiCl-KCl Eutectic

T, K	K_{sp} (FeS)	$\Delta G^\circ = -RT \ln K_{\text{sp}}$	
		kcal mol ⁻¹	kJ mol ⁻¹
673	$0.44 (\pm 0.05) \times 10^{-12}$	38.05	159.1
723	$2.3 (\pm 0.2) \times 10^{-12}$	38.50	160.9
773	$1.3 (\pm 0.1) \times 10^{-11}$	38.50	160.9

We have also calculated the solubility products of a number of other sulfides in the LiCl-KCl eutectic melt *a priori*. These solubility products which are given in Table I-5, indicate very low solubilities for all of these sulfides, some of which have potential as positive electrode materials in batteries. Finally, careful analysis of the data showed that both the J and X phases have marginal stabilities. The formation of the undesirable J phase could be prevented by increasing the ratio of the activity of LiCl to that of KCl in the electrolyte in a manner which can be deduced from our data.

Table I-5. Calculated Solubility Products of Some Sulfides at 700 K

Sulfide	K_{sp}	Sulfide	K_{sp}	Sulfide	K_{sp}
Ag(I)	1.85×10^{-16}	Fe(II)	1.2×10^{-12}	Pb(II)	1.16×10^{-12}
Cu(I)	6.04×10^{-17}	Mg(II)	7.65×10^{-2}	Ti(II)	1.83×10^{-16}
Cu(II)	4.32×10^{-19}	Mn(II)	1.26×10^{-11}	Zn(II)	3.65×10^{-13}
Cr(II)	1.36×10^{-11}	Ni(II)	1.17×10^{-16}		

C. Salt Vapor Studies

(G. H. Kucera and G. N. Papatheodorou)

The formation of vapor complexes between volatile "acidic gases" ($A_2X_6 = Al_2Cl_6, Al_2Br_6, In_2Cl_6, \text{etc.}$) and a variety of involatile metal halides (MX_p) has been investigated. The strong bonding in these complexes is little understood and careful studies are needed as a basis for understanding their nature.

Simple experiments have shown that the volatility enhancement of the MX_p salts in the acidic gas environment can be used for mass-transport purification and single-crystal growth. Vapor complexes also play an important role in the new energy-efficient ALCOA process for the production of aluminum and in the construction of high-efficiency lamps. Furthermore, vapor complexes of lanthanides have been considered as lasing materials for the construction of high-power gas lasers.

Structural and thermodynamic studies of certain high-temperature vapor species are discussed below:

1. Raman Spectra of Indium Halide Vapors and of Indium Aluminum Halide Vapor Complexes

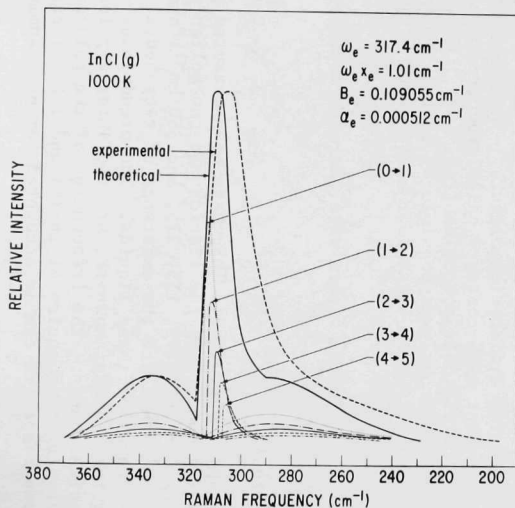
The Raman spectra of vapors over liquid indium chlorides and bromides with the stoichiometries InX , InX_2 and InX_3 ($X = Cl$ or Br) and of vapors over liquid $InAlX_4$ were obtained. A laser Raman system described previously²² has been used for this study at temperatures up to 1200 K.

The spectra of InX vapors consisted of the 0, Q, and S vibrational contours that are characteristic for a diatomic molecule. The measured contours are in reasonable agreement with contours calculated from known molecular constants²³ for the InX diatomic molecules (Fig. I-6). An accurate reproduction of the experimental contours was possible by taking into account vibrational-rotational transitions from at least four excited vibrational states.

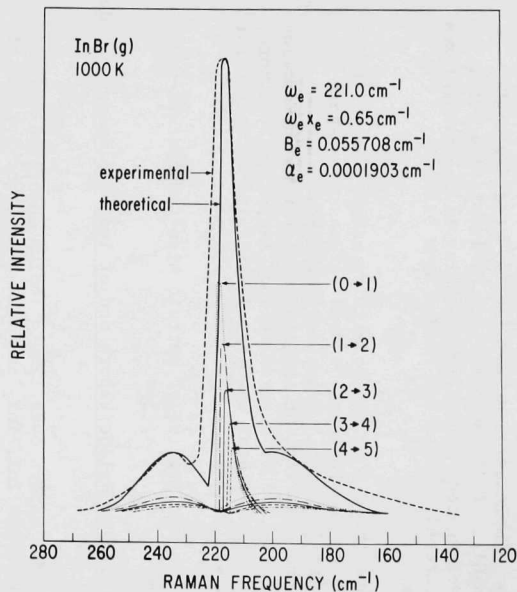
The spectra of indium trihalide vapors were characteristic of the equilibrium:



Raman spectra of vapors over liquid InX_2 have been measured and compared with the corresponding spectra of the liquid. In the molten state, the main observed frequencies for $InCl$ (95, 115, 315, and 350 cm^{-1}) and for $InBr$ (62, 79, 192, and 232 cm^{-1}) indicate the existence of tetrahedral InX_4^- species and a mixed valence state for these liquids. The predominant features of the vapors over the liquids, however, are two intense polarized bands and three weak depolarized bands. The frequencies of the polarized bands are close to the stretching frequencies of $InX(g)$ and $InX_3(g)$ and suggest that the observed vapor spectra can be accounted for by assuming a dissociation:

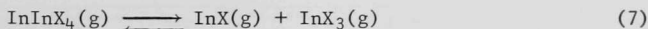


(a)



(b)

Fig. I-6. Experimental and Calculated Vibrational-Rotational Raman Band Contours for InCl(g) and InBr(g) (The theoretical curve is derived by summing the vibrational-rotational-contours of the $0 \rightarrow 1$, $1 \rightarrow 2$, $2 \rightarrow 3$, $3 \rightarrow 4$ and $4 \rightarrow 5$ vibrational states.) ANL Neg. No. 308-77-510 (a); 308-77-513 (b).



with an equilibrium constant greater than one. Raman spectra of InAlX_4 liquids and their vapors were obtained. For each different halide compound, three depolarized bands and a strong polarized band were present in both the liquid and the gas phase. The frequencies of these bands were close to the fundamentals of the AlX_4^- tetrahedra. Temperature-dependence studies of the vapor spectra show that the $\text{InAlX}_4(\text{g})$ molecule dissociates with increasing temperature:

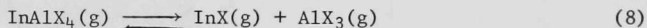
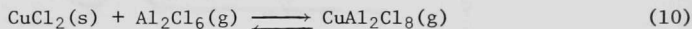


Figure I-7 shows the spectra of the $\text{InAlBr}_4(\text{g})$ molecule from 800 to 1100 K. At 1100 K, the predominant features of the spectrum are attributed to a gas mixture of InBr and AlBr_3 .

2. Resonance Raman Spectra of Pd-Al-Cl and Cu-Al-Cl Vapor Complexes

Resonance Raman spectra of complex vapor-phase compounds formed according to the reactions²⁴



have been measured in the temperature range from 500 to 1100 K and total pressures from 0.1 to ~ 28 atm (1 atm = 101.325 kPa). The equilibrium gas mixture over the MCl_2 (M = Pd, Cu) solid consists mainly of Al_2Cl_6 - AlCl_3 - MAl_2Cl_8 and was contained in fused silica cells. Raman spectra obtained from these mixtures were a superposition of the Al_2Cl_6 - AlCl_3 bands and new polarized Raman bands due to the MAl_2Cl_8 vapor complexes.

Raman spectra obtained with the 647.1 nm laser line from the equilibrium gas mixture Al_2Cl_6 - AlCl_3 - PdAl_2Cl_8 show three high-intensity polarized bands at 84, 175, and 298 cm^{-1} superimposed on the aluminum chloride spectra. The excitation profiles of these bands, which are attributed to PdAl_2Cl_8 , exhibit *minima* in the vicinity of the absorption maxima of the Pd(II) ligand field transition(s). Figure I-8 shows the excitation profile of the 298 cm^{-1} band and the absorption spectra of the PdAl_2Cl_8 molecule.²⁴ The appearance of the minimum is mainly attributed to interference between the weak scattering from the Laporte forbidden electronic transitions (near 20 kK) and strong preresonance scattering from higher-energy allowed charge-transfer states.²⁵ A D_{2d} molecular symmetry is proposed for PdAl_2Cl_8 , having Pd (II) as a central atom in square planar coordination, and the observed Raman bands are assigned as follows:

$$\begin{aligned} \nu_{\text{Pd-Cl (bridged)}} &= 298\text{ cm}^{-1}; \quad \delta_{\text{PdCl}_2} = 175\text{ cm}^{-1}; \\ \nu_{\text{PdCl}_2\text{Al}} &= 84\text{ cm}^{-1} \text{ (ring deformation)} \end{aligned}$$

The Raman spectra of the Cu-Al-Cl vapor complex(es) were obtained using different Kr^+ and Ar^+ laser lines from cells containing no excess of CuCl_2 . All laser lines used lie between the d+d band (11.5 kK) and the first charge transfer band (31 kK) of Cu^{2+} . The intensities of the

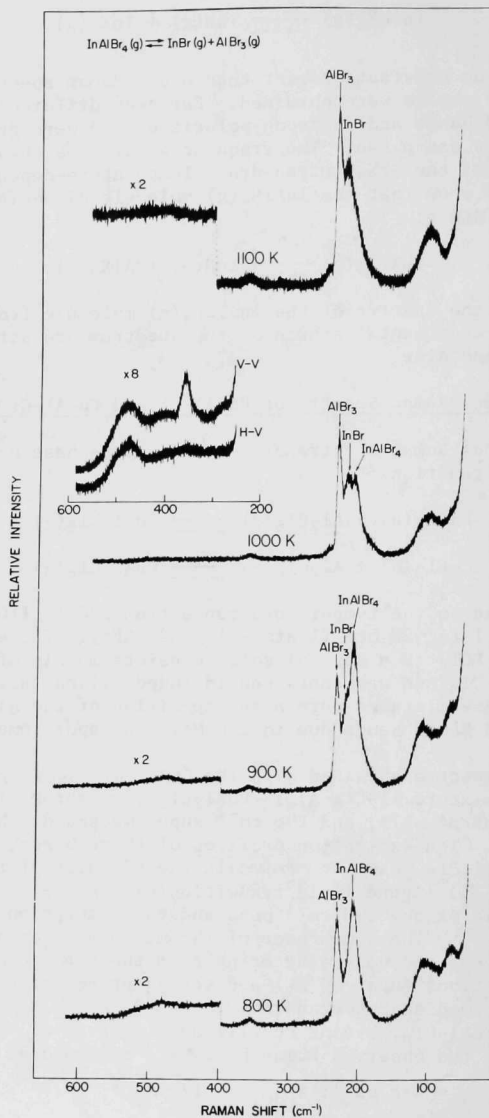


Fig. I-7. Temperature Dependence of Raman Spectra of InAlBr_4 Vapors ($\lambda_0 = 488.0 \text{ nm}$)
ANL Neg. No. 308-77-432

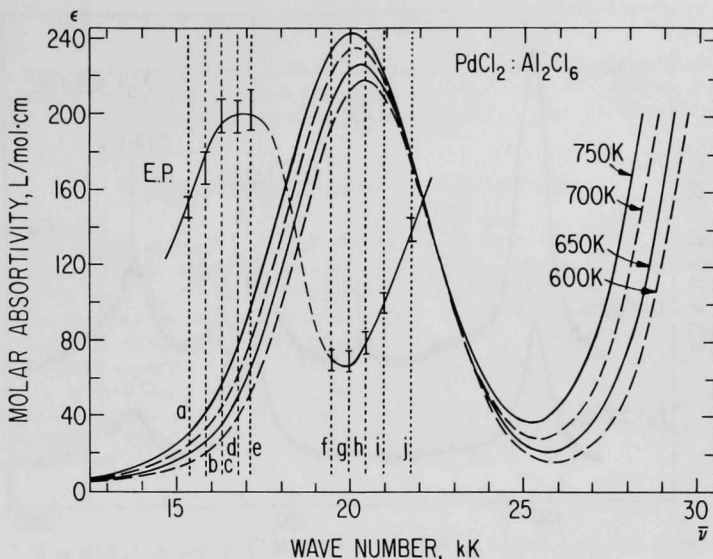
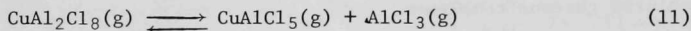


Fig. I-8. Temperature Dependence of Absorption Spectra and Excitation Profile at 575 K for Gaseous PdAl_2Cl_8 . ANL Neg. No. 308-77-168

Raman bands due to the Cu-Al-Cl complex were found to be dependent on (1) the excitation frequency (2) the power of the excitation line and (3) the pressure of the aluminum chloride. The data are interpreted in terms of two copper-containing molecular species:



Three polarized bands at 281 , 174.5 and 84.5 cm^{-1} are assigned to preresonance-enhanced A_1 fundamentals of the CuAl_2Cl_8 molecule. Two strong bands at 448 and 291.5 cm^{-1} and their combinations and overtones are assigned to resonance-enhanced A_1 fundamentals of the CuAlCl_5 molecule having the Cu (II) in trigonal coordination.

Reaction 11 shifts to the right with increasing intensity of the laser line (Fig. I-9). This is attributed to partial decomposition of the $\text{CuAl}_2\text{Cl}_8(\text{g})$ by the laser line and shows that the spectroscopic temperature is much higher than that of the average cell.

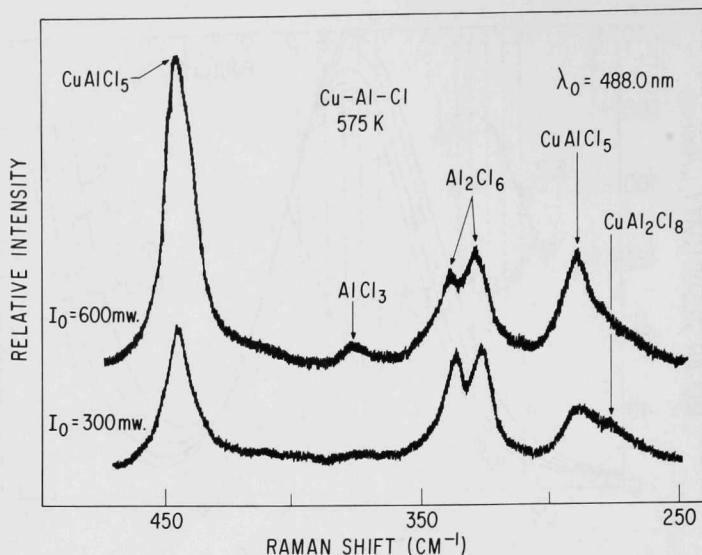
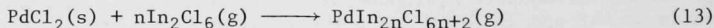
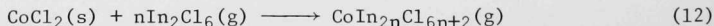


Fig. I-9. Effect of the Intensity of the Excitation Line on the Raman Spectra of the Cu-Al-Cl Gaseous Complexes. ANL Neg. No. 308-77-508

3. Thermodynamics and Spectra of the Co-In-Cl, Pd-In-Cl, and Pd-Al-Br Vapor Complexes

Spectrophotometric investigations have been conducted on reactions of solid divalent transition-metal halides with "acidic gases" to form colored gaseous complexes:

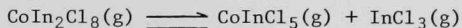


The complex formed in reaction 12 was blue-green and those formed in reactions 13 and 14 were brick red.

Molar absorptivity and vapor pressure data for reaction 12, in the temperature range from 800 to 1100 K and indium chloride pressures up to 11 atm, suggest the presence of more than one vapor species. At lower temperatures (800-900 K) and high pressures, it was determined that the predominant species is CoIn_2Cl_8 . The thermodynamic quantities for the formation of the CoIn_2Cl_8 complex are given by:

$$R \ln K = 9.3 - 11.3/T \quad \text{cal mol}^{-1} \cdot \text{deg}^{-1}$$

At higher temperatures (>900) and/or low pressures, the data indicate that the predominant absorbing species is CoInCl_5 . The Co-In-Cl system can then be rationalized in terms of reaction 12 (with $n = 1$) and the decomposition reaction



The molar absorptivity of the Pd-In-Cl vapor complex (reaction 13) decreased dramatically with increasing temperature, going from $290 \text{ mol}^{-1} \cdot \text{cm}^{-1}$ at 900 K to $70 \text{ mol}^{-1} \cdot \text{cm}^{-1}$ at 1100 K. These changes and the vapor pressure measurements suggest an equilibrium in which more than one vapor species is present. Since similar, but less dramatic, trends were seen in the Co-In-Cl system, it seems reasonable to suggest that two gaseous species analogous to the CoIn_2Cl_8 and CoInCl_5 complexes are formed. From the calculated equilibrium constants and an Arrhenius plot, the thermodynamic quantities for the formation of the PdIn_2Cl_8 complex were deduced and are given (in $\text{cal mol}^{-1} \cdot \text{deg}^{-1}$) by

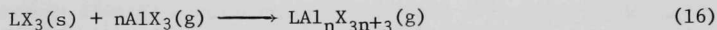
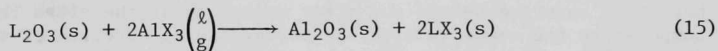
$$R \ln K = 9.7 - 9.9/T$$

The molar absorptivity of the Pd-Al-Br vapor complex (reaction 14) increased slightly with increasing temperature and was found to be independent of the Al_2Br_6 pressure. This pressure independence implies that there is one predominant gaseous species present. With the value of $n = 1$, determined from the vapor pressure measurements, the thermodynamic quantities for the formation of PdAl_2Br_8 (in $\text{cal mol}^{-1} \cdot \text{deg}^{-1}$) are

$$R \ln K = 8.05 - 8.3/T$$

4. Halogenation and Separation of Lanthanide Oxides

Recent experiments indicate that lanthanide oxides can be halogenated by liquid or vapor AlX_3 ($X = \text{Cl}, \text{Br}$) at temperatures above 453 K. The halogenation goes to completion within a few hours with an apparent yield of ~100%. If an excess of AlX_3 is used, the halogenation is followed by a reaction of the AlX_3 with solid lanthanide halides (LX_3) to form vapor complexes. In this manner, the desired LX_3 can be separated from the residue formed in the halogenation step. The following reactions are believed to take place:



To test the merits of the procedure, reaction 15 has been verified using $X = \text{Cl}$ with $L = \text{Sm}, \text{Er}, \text{Pr}, \text{Nd}$, and using $X = \text{Br}$ with $L = \text{Sm}, \text{Pr}, \text{Nd}$. Reaction 16 has been investigated spectrophotometrically for $L = \text{Sm}$ and $X = \text{Cl}$ at temperatures up to 850 K and aluminum chloride pressures up to 10 atm. The spectrum of the pale yellow SmCl_{3n+3} vapor complex shown

in Fig. I-10 is characteristic of the $f \rightarrow f$ electronic transitions of Sm(III) . Thermodynamic considerations indicate that the predominant vapor complex is $\text{SmCl}_3 \cdot 3\text{AlCl}_3$.

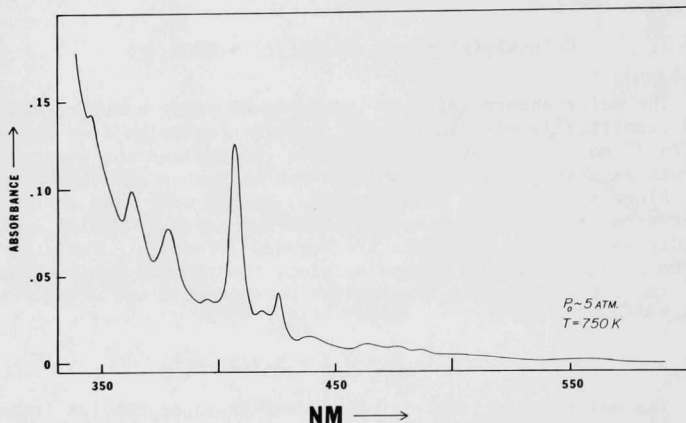


Fig. I-10. Absorption Spectrum of the $\text{Sm}^{3+}\text{-Al-Cl}$ Vapor Complex. ANL Neg. No. 308-77-174

In other experiments, using fused silica containers and employing temperature gradients, it was shown that a mixture of Pr_2O_3 and Er_2O_3 could be chlorinated and vapor-transported. With the bulk of the materials at 400°C and a gradient of $\sim 100^\circ$ along the length of the tube, it was seen that the vapor-transported chlorides were deposited in different parts of the tube. It thus appears that a procedure utilizing reactions 15 and 16 can be developed for the simultaneous chlorination and separation of the lanthanide oxides.

5. Irreversible Thermostructural Transformations in Amorphous As_2S_3 Films*

Polarized Raman spectra of evaporated thin films of As_2S_3 glass have been recorded before and after annealing at the glass transition temperature and compared with the corresponding spectrum of the bulk glass (Fig. I-11). The spectra of virgin films consist of several sharp molecular bands superimposed on a network-like continuum that is characteristic of the bulk glass, whereas annealed films yield only the bulk glass spectrum, albeit with some indication of residual nonstoichiometry. These results are direct evidence that irreversible thermostructural transformations (or equivalent photostructural transformations) in evaporated As_2S_3 films proceed through polymerization of a metastable molecular glass as suggested by deNeufville,

* In collaboration with S. A. Solin, Department of Physics, University of Chicago.

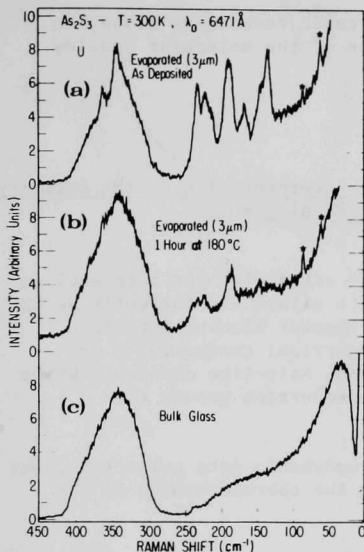


Fig. I-11.

Polarization Unanalyzed (U) Raman Spectra of (a) an Evaporated As-Deposited Film, (b) after Annealing at 180°C for 1 h, and (c) Bulk Glass.

Moss, and Ovshinsky.²⁶ The polarized Raman spectra of the vapors over As_2S_3 liquid have been obtained and indicate the presence of several gaseous molecular species (Fig. I-12). The molecular constituency of the evaporated amorphous film is also complex but distinct from that of the vapor, an indication that deposition itself introduces some structural alterations.

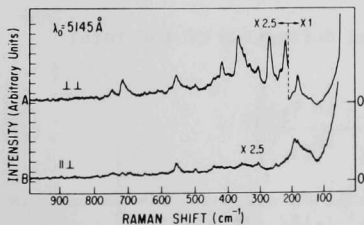


Fig. I-12.

Polarized Raman Spectrum of As_2S_3 Vapors at 600°C (Excited with 1.1 W of 5145-Å Ar radiation and recorded with a spectral slit width of 8.6 cm^{-1} , a time constant of 2 sec, and a scan rate of 12.5 $\text{\AA}/\text{min}$)

Our results provide a direct confirmation of that part of the deNeufville, Moss and Ovshinsky model which ascribes irreversible thermostructural and photostructural transformation in evaporated As_2S_3 films to polymerization of a partially cross-linked molecular glass. The polymerization process, however, appears to involve several distinct molecular species, one of which may be As_4S_6 . The molecular composition of the vapor produced by melting bulk As_4S_6 glass in a vacuum is quite complex, is not merely As_4S_6 , and is not preserved in the deposition process used to

produce As_2S_3 amorphous films. Raman spectroscopic techniques alone are markedly inadequate for a proper identification of the molecular species present in As_2S_3 vapor.

D. Thermodynamic Properties of Alloys

(M. Blander)

1. Electromotive Force Measurements and Interpretation of the Activity Coefficients of Lithium in Molten Li-Pb Alloys

(M. L. Saboungi and J. J. Marr)

The lithium-lead system appears to be attractive for both applied and fundamental reasons. Solid and liquid Li-Pb alloys are currently being considered as potential candidates for fusion reactor blanket materials.²⁷ Previous data (neutron-scattering patterns, electrical conductivity and density measurements, *etc.*) seem to indicate some salt-like character which leads to unusual thermodynamic and electrical properties around the composition of the Li_4Pb compound.

We have earlier reported on the thermodynamic data collected using emf techniques.²⁸ We will focus on discussing the thermodynamics of the system.

The variations of $\ln \gamma_{\text{Li}}$ and $\ln \gamma_{\text{Pb}}$, where γ_{Li} and γ_{Pb} refer to the activity coefficients of Li and Pb, respectively, with composition are plotted in Fig. I-13. The striking features in this figure are

- (1) the existence of an inflection point on the curve of $\ln \gamma_{\text{Li}}$ around the composition corresponding to $X_{\text{Li}} \sim 0.8$;
- (2) the strong asymmetry between the two curves. For example, the limiting value of the excess chemical potential of Pb in Li is about twice that of Li in Pb.

The excess stability, ES, defined as the second derivative of the total excess Gibbs free energy (ΔG^E):

$$\text{ES} = \left(\frac{\partial^2 \Delta G^E}{\partial X_{\text{Li}}^2} \right) = \frac{RT}{(1 - X_{\text{Li}})} \left(\frac{\partial \ln \gamma_{\text{Li}}}{\partial X_{\text{Li}}} \right) \quad (17)$$

further reflects the "unusual" behavior of the Li-Pb alloys. The variations of ES with X_{Pb} at $T = 932 \text{ K}$ are plotted in Fig. I-14. An analogous peak has been obtained at a composition close to that of the compound Mg_3Bi_2 .²⁹

Anomalies in the electrical resistivity,³⁰ in the thermoelectric power,³⁰ and in the activity coefficients show that the Li-Pb liquid alloys belong to the type II liquid alloys of Enderby and Collings.³¹ When metals of very different electronegativities are alloyed, a change from metallic behavior to at least partly ionic behavior is expected.^{32,33}

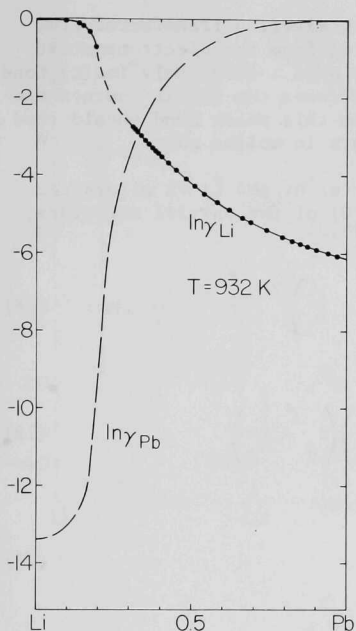


Fig. I-13.

Variations of $\ln \gamma_{Li}$ and $\ln \gamma_{Pb}$ with the Atom Fraction of Pb at $T = 932$ K. (The $\ln \gamma_{Pb}$ values indicated by the broken line are calculated) ANL Neg. No. 308-77-254

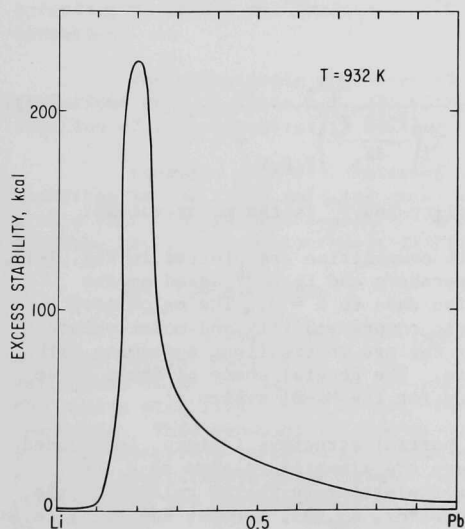


Fig. I-14.

Variation of the Excess Stability,

$$ES = \frac{RT}{1 - X_{Li}} \left(\frac{\partial \ln \gamma_{Li}}{\partial X_{Li}} \right), \text{ with}$$

Composition at 932 K. ANL Neg. No. 308-77-318

In such cases, one may picture that an electron transferred from the alkali metal pairs up with a valence electron from the electronegative atom and is localized, thus forming a polar (or even a completely ionic) bond between the two atoms. The attractive forces between the unlike charges and the repulsive forces between the like charges in this polar bond should lead to short-range ordering such as that which occurs in molten salts.

Other indications of the ionic character of the Li-Pb alloys can be deduced from the long wavelength limit ($\vec{k} = 0$) of the partial structure factors, a_{ii} and a_{ij} , which can be written as:^{34,35}

$$a_{ii}(\vec{k}=0) = \phi - \frac{X_j}{X_i} + A \left(\delta_i - \frac{1}{X_i} \right)^2 \quad (18)$$

and

$$a_{ij}(\vec{k}=0) = \phi + 1 - A \left(\delta_i - \frac{1}{X_i} \right) \left(\delta_j - \frac{1}{X_j} \right) \quad (19)$$

The quantities, ϕ , δ_i and A are defined as follows:

$$\phi = \left(\frac{RT}{V_m} \right) \beta_T \quad (20)$$

$$\delta_i = \frac{1}{V_m} \left(\frac{\partial V_m}{\partial X_i} \right)_{T,P,N} = - \frac{1}{V_m} \left(\frac{\partial V_m}{\partial X_j} \right)_{T,P,N} \quad (21)$$

and

$$A = RT \left(\frac{\partial^2 \Delta G}{\partial X_i^2} \right)_{T,P,N}^{-1} = \frac{X_i X_j}{X_i \left(\frac{\partial \ln \gamma_i}{\partial X_i} \right)_{T,P,N} + 1} \quad (22)$$

where β_T is the isothermal compressibility and V_m is the molar volume.

The variations of $a_{ij}(0)$ with composition are plotted in Fig. I-15, together with the calculations of Ruppertsberg and Egger³⁶ based on the extrapolation of the neutron-diffraction data to $\vec{k} = 0$. The calculated values of $a_{ij}(0)$, based on thermodynamic compressibility and molar volume data (Eqs. 18-22, where 1 = Li and 2 = Pb) are in excellent agreement with those based on neutron diffraction data. The general shape of these three curves is similar to the one calculated for the Mg-Bi system.³⁷

One can also use the set of partial structure factors, introduced by Bhatia and Thornton.³⁵ These factors are linearly related to $a_{ij}(\vec{k})$. At the long wave-length limit ($\vec{k} = 0$), the structure factor related to the fluctuations in the composition of the alloy, $S_{CC}(0)$, becomes identical to A :

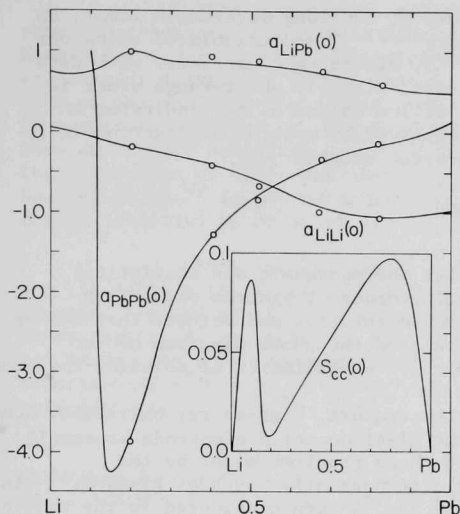


Fig. I-15.

Calculated Variations of the Partial Structure Factors, $a_{\text{LiLi}}(0)$, $a_{\text{LiPb}}(0)$, $a_{\text{PbPb}}(0)$, and $S_{\text{CC}}(0)$ at the Long Wavelength Limit, with Composition. (The circles refer to results derived from the neutron diffraction data of Ruppersberg and Egger.³⁶) ANL Neg. No. 308-77-317

$$S_{\text{CC}}(0) = A = N \langle (\Delta X_1)^2 \rangle \quad (23)$$

A plot of $S_{\text{CC}}(0)$ versus X_{Pb} is given in the inset of Fig. I-15. The only important feature is the fact that $S_{\text{CC}}(0)$ presents a dip around $X_{\text{Pb}} \approx 0.2$ which, according to Bhatia and Thornton,³⁵ is a characteristic feature of complex formation.

The quasi-ionic character is also confirmed if one compares the variations of $a_{\text{LiLi}}(0) - a_{\text{PbPb}}(0)$ with those of an ionic system using a relation of electroneutrality defined by Stillinger and Lovett.³⁸

Finally, we have considered a primitive model in which the lithium electrons in the Li-Pb solution exist either in bound lower states (paired with a lead electron and localized on lead anions) or in upper states (the electron gas), and are thermally distributed between these levels.³⁹

a. Conclusions

In the temperature range 770-932 K, measurements of the activity coefficients of Li in Li-Pb alloys exhibit "anomalies" in the variations of $\ln \gamma_{\text{Li}}$ versus X_{Pb} (*i.e.*, an inflection point), as well as in the excess stability (*i.e.*, a sharp peak), in the vicinity of the Li-rich compounds. This behavior is consistent with the unusual behavior observed in other properties such as the molar volume and is also consistent with a proposed constitutive ionic nature of the alloy. However, the ionic character is not unambiguously determined and other types of bonding may be involved.

Partial structure factors at the long wavelength limit, as defined by Ziman, Enderby, and coworkers^{30,31,34} and calculated using our data for the activity coefficients of Li, are in good agreement with data derived from neutron diffraction patterns. If only short-range order is significant, then the slope of $\ln \gamma_{Li}$ at low values of X_{Li} indicates an ordering effect consistent with that observed by neutron diffraction in which unlike atoms are preferred as nearest neighbors.

2. Computation of Phase Diagrams (M. L. Saboungi and C. C. Hsu)

The utilization of fundamental thermodynamic and statistical mechanical concepts in the study of multicomponent systems presents a fundamental challenge in devising suitable theories and methods that can be applied to such systems. We have calculated the phase diagrams of two ternary alloys to illustrate the predictive capabilities of solution theories.

In the development of high-temperature, high-energy batteries, some problems have been encountered with the Li-Al negative electrode presently being developed at ANL. A solution to these problems might be the replacement of the Li-Al electrode by a ternary alloy such as Li-Al-M.⁴⁰ In addition to such an alloy, some calcium alloys were considered in the search for new electrode materials for batteries. The interaction of these electrodes with the LiCl-KCl-CaCl₂ electrolyte is an important factor in the selection of the alloy.⁴¹ Therefore, a knowledge of the phase diagram of either Al-Li-M or Ca-Li-M helps in providing valuable information on the chemical stability of the phases present in the temperature range of battery operation: 673-773 K. We report on a thermodynamically self-consistent prediction of isothermal sections of the phase diagrams of the ternary Al-Li-Mg and Ca-Li-Mg systems. Our calculations are to be considered as a preliminary construction of a phase diagram that can be modified to account for new phase data.

a. The Al-Li-Mg System

Alloys of Al-Li-Mg have been of interest from a practical point of view. They were primary candidates in a search for ductile, malleable structural materials.⁴² However, to our knowledge, there is rather incomplete and inconsistent information in the literature on the phase diagram.

Shamrai, in a series of papers, Ref. 43 being the last, reported the phase diagram of Al-Li-Mg, as well as isothermal sections at 20°C and 400°C. The ternary compound MgLiAl₂ was identified. Frost *et al.*⁴⁴ studied the phase relationships at 700°F (≈644 K) for several compositions of the alloys. Jones *et al.*⁴⁵ reported the 500°F and 700°F isothermal sections of Al-Li-Mg alloys. The ternary compound MgLi₂Al was identified. Rowland *et al.*⁴² investigated some isothermal sections of the magnesium-rich corner of the Al-Li-Mg system. Their metallographic and X-ray results did not confirm the existence of the compound MgLi₂Al at equilibrium. In a recent investigation,⁴⁶ microstructural analyses of Al-Li-Mg alloys quenched from 573 K revealed the presence of MgLiAl₂ in equilibrium with Mg₁₇Al₁₂ and LiAl. However, no additional information on the stability of the MgLiAl₂ phase at the temperatures of interest to us was provided.

When comparisons are possible, the different investigations show disagreement. The latest data are in contradiction with those of Shamrai; not only are the compositions irreproducible, but also there is a significant difference in the phases. It seems impossible to reconcile the data of Shamrai with the others even by considering the minor differences in temperature (673 K *vs.* 648 K or 644 K). The four latest investigations show an overall consistency with slight differences in the compositions of the boundaries of different phases. However, the X-ray diffraction data of Rowland *et al.*⁴² do not corroborate the existence of the ternary compound $MgLi_2Al$ observed by Jones *et al.*⁴⁵

Finally, one has to be aware that in all these investigations, the liquidus of the subsidiary binary Li-Al was not well defined. For example, Rowland *et al.*⁴² referred to Li_2Al as a stable compound; it is known that Li_2Al is indeed Li_9Al_4 . Also, the existence of Li_3Al_2 was not yet known. As a consequence of the uncertainties and without further experimental evidence, we did not include any ternary compound in our calculations.

The calculated isothermal sections of the Al-Li-Mg system are given in Fig. I-16 for $T = 673$ K, Fig. I-17 for $T = 728$ K, and Fig. I-18 for $T = 648$ K. They were computer-generated by considering all the possible interactions on a pair-wise basis:

At the Al-rich corner: FCC *vs.* $LiAl$, FCC *vs.* L,
FCC *vs.* Al_3Mg_2 , L *vs.* $LiAl$.

At the Li-rich corner: L *vs.* Li_3Al_2 and L *vs.* BCC.

At the Mg-rich corner: HCP *vs.* L, HCP *vs.* BCC,
HCP *vs.* Al_9Mg_{11} and L *vs.* Al_9Mg_{11} .

The Kohler⁴⁷ equations are used to describe the ternary solution. The coefficients necessary to define the solution thermodynamics are those determined in an earlier study of the binary systems, Li-Al, Li-Mg and Mg-Al.⁴⁸ More details on the computational techniques can be found elsewhere.^{48,49} The isothermal section at 648 K (375°C) was calculated in order to allow a better comparison with the data of Rowland *et al.*, collected for the Mg-rich corner; however, a direct comparison cannot really be made since Rowland *et al.*⁴² were not aware of the existence of Li_3Al_2 . Nevertheless, there is reasonable agreement between our computed isotherm and the experimental data, if one takes into consideration the differences in the binary Li-Al. However, the most striking similarity between Fig. I-19 and the X-ray data of Rowland *et al.*⁴² is the nonexistence of the liquid phase. Note that a difference of 25 K led to the disappearance of the liquid in the Mg-rich side of the system.

b. The Ca-Li-Mg System

The results of a literature survey reveal that neither a measured nor a calculated ternary phase diagram of the Ca-Li-Mg system has been reported. The calculated results of the Ca-Li-Mg diagrams reported here are considered to be the first set of data available. Consequently, comparisons cannot be made.

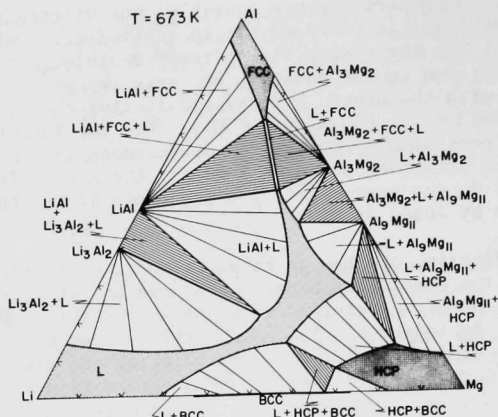


Fig. I-16. Computed Isothermal ($T = 673$ K) Section of the Phase Diagram of the Al-Li-Mg System. ANL Neg. No. 308-76-409

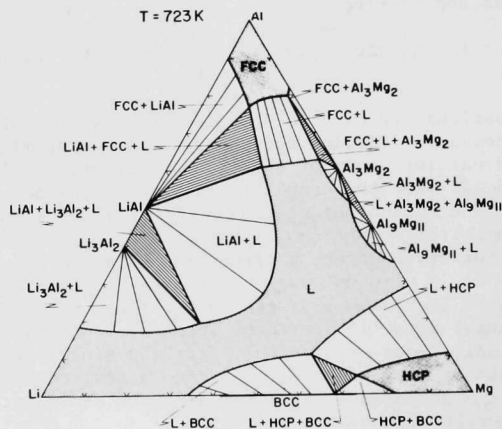


Fig. I-17. Computed Isothermal ($T = 723$ K) Section of the Phase Diagram of the Al-Li-Mg System. ANL Neg. No. 308-76-408

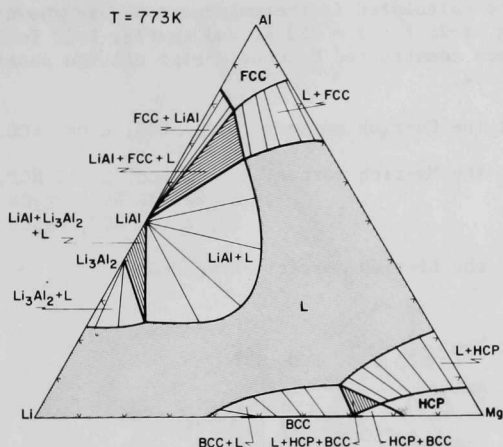


Fig. I-18. Computed Isothermal ($T = 773 \text{ K}$) Section of the Phase Diagram of the Al-Li-Mg System. ANL Neg. No. 308-76-410

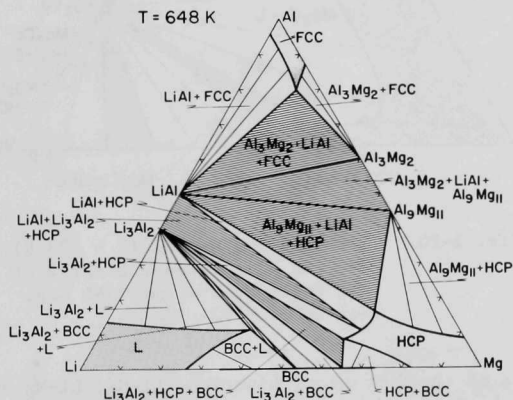


Fig. I-19. Computed Isothermal ($T = 648 \text{ K}$) Section of the Phase Diagram of the Al-Li-Mg System. ANL Neg. No. 308-76-415

The calculated isothermal sections are shown in Fig. I-20 for $T = 673$ K, in Fig. I-21 for $T = 723$ K, and in Fig. I-22 for $T = 773$ K. The phase diagrams were constructed by considering all the possible interactions on a pair-wise basis:

At the Ca-rich corner: L vs. BCC, L vs. FCC.

At the Mg-rich corner: L vs. BCC, L vs. HCP,
 Mg_2Ca vs. FCC, Mg_2Ca vs. L,
 Mg_2Ca vs. HCP, Mg_2Ca vs. BCC.

At the Li-rich corner: L vs. BCC.

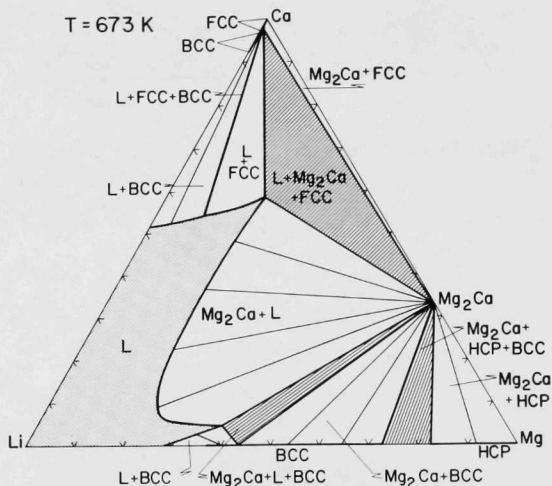


Fig. I-20. Computed Isothermal ($T = 673$ K) Section of the Phase Diagram of the Ca-Li-Mg System. ANL Neg. No. 308-76-412

The thermodynamics of the subsidiary binaries, Li-Ca, Li-Mg and Ca-Mg, were included in the Kohler equations to compute these isothermal sections.

However, it must be emphasized that these calculations are not to be considered final. It would be desirable to have some experimental information as feedback. Modifications can be easily performed to (1) include ternary compounds (stable or metastable); (2) change the stability of the compound generated from the binary compounds; and (3) include any reliable data on the solubility of a component, C, in a binary solution, A-B. These changes can be easily performed within the framework of the present computer program. However one must be aware of the various limitations inherent in the techniques and models.

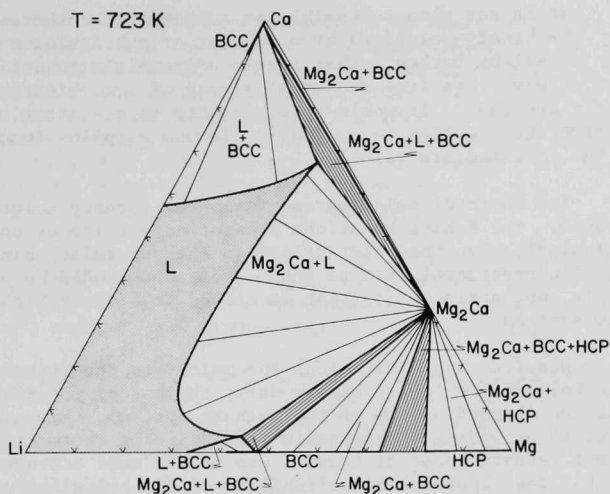


Fig. I-21. Computed Isothermal ($T = 723 \text{ K}$)
Section of the Phase Diagram of
the Ca-Li-Mg System. ANL Neg.
No. 308-76-416

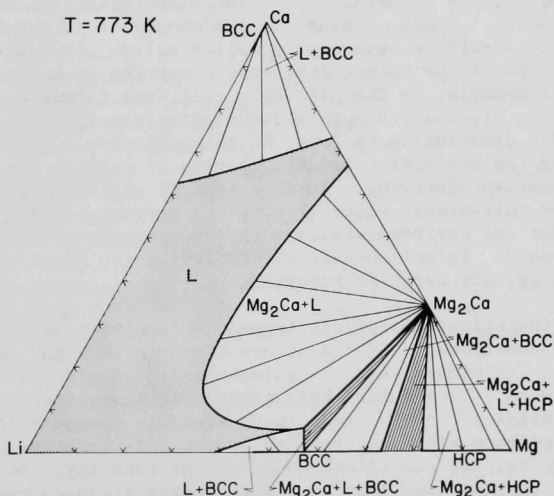


Fig. I-22. Computed Isothermal ($T = 773 \text{ K}$)
Section of the Phase Diagram of
the Ca-Li-Mg System. ANL Neg.
No. 308-76-414

It is not always possible to represent the thermodynamic properties of the binary solutions by a regular or subregular model. It has been shown in detail by Darken²⁹ that simple polynomials cannot always represent the excess Gibbs free energy of mixing of some binary systems such as Li-Pb. In these cases, it would be preferable to use other numerical methods to solve the equation (*e.g.*, one could use a spline function to interpolate the intermediate values).

The thermodynamic representation of ternary solutions can also be improved. The Kohler equations are not as precise as one would desire, particularly when the interactions in the subsidiary binaries are significant. A correctional term to these equations should be considered as, for example, one analogous to that developed in a theoretical study of ternary ionic systems.⁵⁰

Despite some limitations due mainly to the formalism used (*i.e.*, simple polynomials to fit binary data, the use of the Kohler equations for the thermodynamics of the ternary system), this numerical tool remains useful in providing a reasonable prediction of thermodynamically self-consistent ternary phase diagrams. One of the most attractive features is the fact that the accuracy and reliability of the calculations can be improved greatly with a very small amount of experimental information.

E. Electrochemical Studies

1. Metal Deposition/Dissolution Studies (Zoltan Nagy)

This activity consists of a systematic investigation of the kinetics and mechanisms of metal deposition/dissolution reactions in molten alkali halide salts. These studies are fundamental to a general understanding of electrode behavior in molten salts. In addition, these reactions are some of the elementary steps occurring in molten-salt batteries. For example, in the LiAl-FeS_x cell, the formation of iron sulfides probably proceeds through a dissolution-precipitation mechanism in which the anodic dissolution to form the tetrachloride complex is the first step. Likewise the deposition and dissolution of lithium is an elementary step at the negative electrode. Another area of significance is in metalwinning by molten-salt electrolysis--new processes which may be less energy intensive and environmentally more favorable than the present smelting processes. In molten-salt electrolysis, the metal deposition is, of course, the primary cathodic reaction.

The investigations of electrode kinetics have been initiated. The rates of these reactions, as a class, are known to be high, and, therefore, fast relaxation techniques, such as galvanostatic single- and double-pulse measurements, were selected for their study. In these techniques, the change of potential of an electrode is observed in response to current steps.⁵¹ The methods yield information on the rate constant of the overall electrode reaction, the electrical double-layer capacity, and the diffusion coefficient of the reactant species. The concentration dependence of the reaction rate can lead to mechanistic conclusions, mainly to the identification of the rate-determining step. From the temperature dependence of the rate one can, of course, obtain the activation energy.

For fast electrode reactions the time scale of pulses is in the nsec to μ sec range. This requires well-designed electric circuitry, including, as integral parts, fast-rise pulse generators and oscilloscopes, together with impedance-matched cells and leads with minimum stray capacitances and residual inductances. The initial measurements utilized high-temperature coaxial cables and a coaxial cell design. With this apparatus the induction spike and the following ringing were made to subside in about 300 nsec. Even with further refinements, the ringing could, at best, be made to subside in the 50-100 nsec range.

Measurements on iron in the LiCl-KCl eutectic melt, using the single-pulse galvanostatic technique at 450°C and at $7.7 \times 10^{-6} \text{ mol/cm}^3 \text{ Fe}^{2+}$ concentration, has shown that the reaction rate is unusually high ($i_0 \gtrsim 10 \text{ A/cm}^2$) and is outside the range of this technique.

In preparation for the application of the galvanostatic double-pulse technique, which is applicable to reaction rates outside the range of the single-pulse method, theoretical work was carried out to eliminate weaknesses of the double-pulse technique as presently practiced.

In the double-pulse technique, a short, high-current prepulse is applied to precharge the double layer before the application of the measuring pulse. This enables kinetically meaningful measurements to be made at very short times when the diffusional effects are not yet overwhelming. It has been estimated that this allows the measurement of rate constants that are one order of magnitude larger than measurable by the single-pulse method. To assure the correct charging of the double layer, the pulse is adjusted to give a horizontal overpotential trace on the oscilloscope at the beginning of the second pulse. However, an inevitable inductive spike and the following ringing due to the impedance mismatch between the cell and the leads makes the observation of the horizontal trace difficult, and a systematic error is introduced. We have modified the technique to completely eliminate this difficulty. If the double layer is deliberately overcharged with the first pulse, a minimum will be observed in the potential trace during the second pulse. The potential reading at the minimum can be used to determine the kinetics of the reaction. The observation of the minimum is not obstructed by the ringing since it can be adjusted to occur after the ringing has subsided. The appropriate diffusional equations were solved to allow the separation of the overpotential into activation and diffusion parts.

The theoretical analysis of the method was also extended to a generalized multistep reaction scheme in which each step can contain any number (0 and up) of electron transfers and any of the steps can be rate-determining.

An error analysis was also carried out taking into account the nonideality of the current pulses (finite rise-time). It was shown that the error will be negligible ($< 1\%$) with our equipment which has a rise-time of about 30 nsec. On the other hand, very large errors ($\gtrsim 10\%$) will be encountered if the rise-time is larger than 0.5 μ sec. These advances in the theory of the galvanostatic double-pulse technique will also be applied to other relaxation techniques.

F. Meteoritic Studies
(M. Blander)

1. Oxygen Isotopes in Refractory Inclusions in Carbonaceous Meteorites

Clayton *et al.*⁵² have collected a large number of their observations on oxygen anomalies in refractory calcium-aluminum-rich inclusions (CAI's) found in some carbonaceous meteorites. These have been interpreted as originating from a separate, small amount of an extra-solar or pre-solar component which gets mixed into the CAI's. We have proposed an alternative scheme⁵³ in which the entire CAI is composed of minerals in which the oxygen is largely ^{16}O . These then are immersed in an environment with the "normal" oxygen complement of ^{17}O and ^{18}O which diffuses into the interiors of the minerals. We solved the diffusion equations for the case in which the diffusion coefficients of ^{18}O are smaller than those for ^{17}O . For the maximum isotope effect ($D_{17}/D_{18} = 1.03$), we calculate that the oxygen anomalies should follow the curve plotted as a solid line in Fig. I-23. If the original hypothesis of Clayton was valid, the isotope anomalies would follow the dashed curve in Fig. I-23. All of the points of Clayton *et al.*⁵² plotted in Fig. I-23 appear to follow the diffusion hypothesis and negate most of the speculations on the source of these anomalies. This diffusion model and the concepts of constrained equilibria⁵³ appear to be necessary to understand the properties of these unusual materials^{53,54} and Clayton and Mayeda appear to have adopted the diffusion model in modified form.⁵⁵

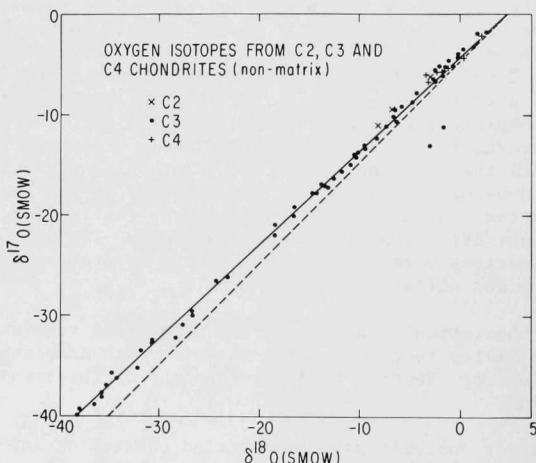


Fig. I-23. Oxygen Isotope Anomalies in Carbonaceous Chondrites. (Points are from Ref. 52. Solid line--diffusion model. Dashed line--model for mechanical mixing of pre-solar ^{16}O -rich component with materials with the normal oxygen isotopic composition.) ANL Neg. No. 308-77-316

REFERENCES

1. J. N. Butler and R. S. Brokaw, *J. Chem. Phys.* **26**, 1636 (1957).
2. T. A. Renner, G. H. Kucera, and M. Blander, *J. Chem. Phys.* **66**, 177 (1977).
3. T. A. Renner and M. Blander, *J. Phys. Chem.* **80**, 857 (1977).
4. See for example, G. Allen and E. F. Calden, *Quart. Rev.* **7**, 255 (1953).
5. W. Bernst, *Boltzmann-Festschrift*, **904**, (1904); See also Ref. 1.
6. J. D. Lambert, E. N. Staines, and S. D. Woods, *Proc. Roy. Soc., London*, **200A**, 262 (1949).
7. J. Del Bene and J. A. Pople, *J. Chem. Phys.* **52**, 4858 (1970).
8. J. Del Bene, *J. Chem. Phys.* **55**, 4633 (1971).
9. W. A. Lathan, L. A. Curtiss, W. J. Hehre, J. B. Lisle, and J. A. Pople, *Progress in Physical Organic Chemistry*, A. Streetweiser and R. S. Taft, Eds., John Wiley and Sons, Inc., New York, 1974, Vol. 11, p. 175.
10. P. J. Krueger and H. D. Mettee, *Can. J. Chem.* **42**, 340 (1964).
11. D. J. Frurip, L. A. Curtiss, and M. Blander, *Proc. 7th Symp. on Thermophysical Properties*, p. 721 (1977).
12. J. E. Del Bene, G. T. Worth, F. T. Marchese, and M. E. Conrad, *Theor. Chim. Acta (Berl.)*, **36**, 195 (1975).
13. P. A. Nelson, *et al.*, *High-Performance Batteries for Stationary Energy Storage and Electric Vehicle Propulsion, Progress Report for the Period January-March 1977*, Argonne National Laboratory Report, ANL-77-35 (June 1977).
14. H. A. Laitinen and J. W. Pankey, *J. Amer. Chem. Soc.* **81**, 1053 (1959).
15. H. A. Laitinen and C. H. Liu, *J. Amer. Chem. Soc.* **80**, 1015 (1958).
16. F. C. Mrazek and J. E. Battles, *J. Electrochem. Soc.* **124**(10), 1556 (1977); B. Tani, *Amer. Mineral* **62**, 819 (1977).
17. J. E. Hall, Argonne National Laboratory, unpublished data.
18. C. H. Liu, A. J. Zielen and D. M. Gruen, *J. Electrochem. Soc.* **120**, 67 (1973).
19. A. E. Martin, Argonne National Laboratory, private communication.
20. G. Kucera and M. L. Saboungi, *Met. Trans.* **7B**, 213 (1976).

21. M. L. Saboungi, J. J. Marr and M. Blander, Extended Abstract No. 37, 152nd Meeting of the Electrochemical Society, October 1977.
22. G. N. Papatheodorou, J. Chem. Phys. *66*, 2893 (1977).
23. A. H. Barret and M. Mandel, Phys. Rev. *109*, 1572 (1958).
24. G. N. Papatheodorou, J. Phys. Chem. *77*, 472 (1973).
25. M. Z. Zgierski, J. Raman Spectrosc. *6*, 53 (1977).
26. J. P. deNeufville, S. C. Moss, and R. S. Ovshinsky, J. Non-Cryst. Solids *13*, 191 (1974).
27. J. R. Powell, F. T. Miles, A. Aronson and W. E. Winsche, *Studies of Fusion Reactor Blankets with Minimum Radioactive Inventory and with Tritium Breeding in Solid Lithium Compounds: a Preliminary Report*, Brookhaven National Laboratory Report, BNL-18236, June 1973.
28. M. Blander *et al.*, *Physical Inorganic Chemistry Annual Report, July 1975-June 1976*, Argonne National Laboratory Report, ANL-76-101.
29. L. S. Darken, Trans. AIME *239*, 80 (1967).
30. J. E. Enderby, J. Phys. (Paris) *35*, C4-309 (1974).
31. J. E. Enderby and E. W. Collings, J. Non-Cryst. Solids *4*, 161 (1970).
32. H. Hoshino, R. W. Schmoltzler and F. Hensel, Phys. Lett. *51A*, 7 (1975).
33. R. W. Schmoltzler, H. Hoshino, R. Fisher and F. Hensel, Ber. Bunsenges. Phys. Chem. *80*, 107 (1976).
34. T. E. Faber and J. M. Ziman, Phil. Mag. *11*, 153 (1965).
35. A. B. Bhatia and D. E. Thornton, Phys. Rev. *B2*, 3004 (1970).
36. H. Ruppersberg and H. Egger, J. Chem. Phys. *63*, 4095 (1975).
37. H. Ruppersberg and W. Speicher, Z. Naturforsch. *31a*, 47 (1976).
38. F. H. Stillinger and R. Lovett, J. Chem. Phys. *49*, 1991 (1968).
39. M. L. Saboungi, J. J. Marr and M. Blander, J. Chem. Phys. *68*, 1375 (1978).
40. P. A. Nelson *et al.*, Argonne National Laboratory Report ANL-75-1 (1975).
41. M. F. Roche, Argonne National Laboratory, private communication (1977).
42. J. A. Rowland, Jr., C. E. Armantrout, and D. F. Walsh, Trans. AIME *203*, 355 (1955).
43. F. I. Shamrai, Izvest. Akad. Nauk. S.S.S.R. Otdel. Khim. Nauk. 290-310 (1948).

44. P. D. Frost, J. G. Kura and L. W. Eastwood, Trans. AIME 188, 1277 (1950).
45. A. Jones, J. H. Lennon, R. R. Nash, W. H. Chang and E. G. Mac Peek, Technical Report 52-169 U. S. Air Force, Air Research and Development Command, Wright-Patterson Air Force Base (1952).
46. M. Padezhnova, E. V. Melnik, L. S. Guzei and L. N. Guseva, Izv. Akad. Nauk. S.S.S.R. Met. 4, 222 (1976).
47. F. Kohler, Monatsh Chem. 19, 738 (1960).
48. M. L. Saboungi and C. C. Hsu, CALPHAD 1 (3) pp. 273-251 (1977).
49. L. Kaufman and H. Nesor, Z. Metallk. 64, 249 (1973).
50. M. L. Saboungi and M. Blander, J. Chem. Phys. 63 (1), 212 (1975).
51. P. Delahay, *The Study of Fast Electrode Processes by a Relaxation Technique*, Advances in Electrochemistry and Electrochemical Engineering, Vol. I, Chap. 5, P. Delahay and C. W. Tobias, Eds., Wiley-Interscience (1961).
52. R. N. Clayton, N. Onuma, L. Grossman and T. K. Mayeda, Earth Planet Sci. Lett. 34, 209 (1977).
53. M. Blander and L. Fuchs, Geochim. Cosmochim. Acta 39, 1605 (1975).
54. G. J. Wasserburg, T. Lee and D. A. Papanastassiou, Geophys. Res. Lett. 4, 299 (1977).
55. R. N. Clayton and T. K. Mayeda, Geophys. Res. Lett. 4, 295 (1977).

II. CHEMISTRY OF LIQUID METALS

(V. A. Maroni, E. Veleckis, W. F. Calaway,
R. M. Yonco, D. K. Kroeck,* and J. Magee†)

A. Thermodynamic Studies of the Sorption of Hydrogen in Lithium-Containing Alloys (E. Veleckis, D. K. Kroeck, and J. Magee)

The nature of hydrogen interactions with lithium alloys is of fundamental interest to a number of energy-related technologies (see, for example, references 1 and 2). Since very little information on this subject is available in the literature, we have initiated a program to study the thermodynamics of interactions of hydrogen with selected solid, lithium-containing binary intermetallics.

Two alloys were chosen for the initial study: the β -phase (nominally "LiAl") of the Li-Al system and the γ -phase ("Li₇Pb₂") of the Li-Pb system. Both of these phases melt congruently above 700°C and meet other important criteria required for solid fusion-reactor blankets.¹ The LiAl alloy has found useful applications as an electrode material in lithium-aluminum/metal sulfide batteries.²

The alloys were prepared by melting the required amounts of pure component metals in evacuated, sealed tantalum crucibles. (Special precautions were taken to avoid overheating of the Li-Pb melt owing to the abnormally high heat of alloy formation, 75.6 kcal/mol Li₇Pb₂.³) The alloys were found to be very brittle and could be readily crushed in a mortar and pestle. Approximately 2 cm³ of the -20+80 mesh granules were placed in a thin-walled Armco iron crucible which was then sealed *in vacuo* by electron-beam welding.

The hydridation apparatus and experimental procedures have been described elsewhere.⁴ Briefly, the procedure involved placing the sample capsule in a Sieverts' apparatus, heating to the desired temperature, adding small successive portions of hydrogen, and recording equilibrium hydrogen pressures after each addition.

Hydridation of binary, lithium-containing alloys offers a convenient method for studying the thermodynamic properties and phase relations of these alloys. The method is based on an observation^{5,6} that when hydrogen is contacted with an alloy, LiM_x, it reacts with the lithium in the alloy to form LiH and thereby changes the alloy from its initial composition $x = n_M/n_{Li}$ to a new composition, $x = n_M/(n_{Li} - n_H)$, that is enriched in M. The overall reversible reaction and the corresponding equilibrium constant are given by



* Fall 1976 Undergraduate Research Program Participant, University of Colorado, Colorado Springs, CO.

† Summer 1977 Undergraduate Research Program Participant, Georgia Institute of Technology, Atlanta, GA.

$$K \text{ (atm}^{-1/2}\text{)} = a_{\text{LiH}} / \left(a_{\text{Li}} \cdot \sqrt{P_{\text{H}_2}} \right) \quad (2)$$

In these equations, n is the number of gram atoms, a is the activity, and P_{H_2} is the equilibrium hydrogen pressure in atmospheres.

Below the monotectic temperature of the Li-LiH system⁴ (694°C), the LiH-rich phase is essentially pure solid LiH. Therefore, the LiH precipitating out of LiM_x alloy may be taken to have unit activity and Eq. 2 becomes

$$a_{\text{Li}} = 1 / \left(K \cdot \sqrt{P_{\text{H}_2}} \right) \quad (3)$$

Equation 3 expresses a simple relationship between the activity of lithium in a binary alloy (LiM_x) and the square root of the equilibrium hydrogen pressure over the alloy, the proportionality factor being equal to the reciprocal of the equilibrium constant for reaction 1.

As the quantity of added hydrogen is gradually increased, the composition of the LiM_x alloy will undergo changes in the direction of higher x -values. Homogeneous intermediate phases encountered in these composition ranges will reveal themselves (on isothermal P_{H_2} vs. composition plots) as rising segments, whereas the heterogeneous regions are identifiable by horizontal (plateau pressure) lines.

The equilibrium constant, K , which appears in Eqs. 2 and 3, can be calculated from the standard free energy of formation of solid LiH, *i.e.*, $K = \exp(-G_f^\circ/\text{RT})$. Previous work at ANL on the Li-LiH system has generated sufficient information for the construction of $\ln \sqrt{P_{\text{H}_2}}$ vs. N_{LiH} isotherms between the eutectic and monotectic temperatures. Thus, analytical expressions are available for (1) P-C-T relationships in the α -solution region,⁴ (2) Sieverts' law constants,⁴ (3) plateau pressures,⁷ and (4) solubilities of LiH in liquid lithium.⁸ The standard free energy of formation of solid LiH is obtained by evaluating the following integral:

$$\begin{aligned} \Delta G_f^\circ (\text{kcal/mol}) &= \text{RT} \int_0^1 \ln \sqrt{P_{\text{H}_2}} dN_{\text{LiH}} \\ &= 19.76 \times 10^{-3} T - 22.63 \end{aligned} \quad (4)$$

where N_{LiH} is the mole fraction of LiH in Li-LiH solutions. To assist integration, Sieverts' law was assumed to be valid for $0 < N_{\text{LiH}} < 0.001$.

1. Lithium-Aluminum Alloys

According to a recent phase diagram,⁹ the Li-Al system has four homogeneous solid phases: α (dilute solution of Al in Li), β ("LiAl"), γ ("Li₃Al₂"), and δ ("Li₃Al₄"). The latter two phases are believed to be line compounds, but the β -phase is known to have a wide homogeneity range. We have prepared three LiAl_x samples having compositions within the β -phase (51.5, 47.7, and 44.4 at. % Al).

The results for the first two alloy preparations are shown in Fig. II-1a as $\log P_{H_2}$ vs. at. % Al isotherms. Both alloys produced essentially the same Al-rich boundary for the β -phase (~ 52 at. % Al). On the left side of this boundary, the rising isothermal segments correspond to the homogeneity ranges of the β -phase. Constant pressure plateaus on the right side indicate the onset of a wide ($\alpha + \beta$) region.

Figure II-1b shows the corresponding lithium activity plots, calculated for the pressure data of Fig. II-1a using Eqs. 3 and 4. Yao *et al.*¹⁰ have reported emf measurements for the 50 at. % Al alloy at three temperatures (314, 343, and 380°C). The corresponding a_{Li} values, extrapolated from their data to the temperatures of our study, show excellent agreement.

Further comparison between the hydridation and emf data can be made using the extensive data collected for the ($\alpha + \beta$) region, where the hydrogen pressure and emf measurements are more reliable because of their insensitivity to variations in the alloy composition. These data are shown in Fig. II-2 as $\log a_{Li}$ vs. 1000 K/T plots. There appears to be a slight disagreement between the two studies. Probable sources for the disagreement could include inaccuracies in the ΔG_f° (solid LiH) values or the impurity effects in the alloys. Final judgment must await the completion of experimental work. Hydridation experiments with the final alloy sample (44.4 at. % Al) are under way.

2. Lithium-Lead Alloys

The hydridation technique of investigating intermetallic alloys is being tested on a more complex alloy system, namely, the Li-Pb system. The reported phase diagram³ reveals a host of intermediate phases: $Li_{22}Pb_5$, Li_7Pb_2 , Li_3Pb , Li_8Pb_3 , and $LiPb$. Since our principal interest is centered around the highest melting phase, " Li_7Pb_2 ", we made alloy preparations with compositions on the lithium-rich side of that phase. Exploratory experiments at 500 and 550°C show that the pressure vs. composition isotherms have traversed three intermediate phases (Li_7Pb_2 , Li_3Pb , and Li_8Pb_3) at the stoichiometric ratios predicted in the phase diagram. The first of these phases shows a narrow range of homogeneity.

B. Resistometric Studies of Distribution and Corrosion Phenomena in Liquid-Metal Systems (W. F. Calaway)

During FY 1977, a project was initiated to investigate ternary systems of the form, $Li-M-X$, where M is a transition metal and X is a nonmetallic element such as nitrogen, oxygen or carbon. The project is aimed at increasing knowledge of lithium corrosion of metals by examining selected aspects of the solution behavior of nonmetallic elements in the two metal phases. The systems of interest will consist of the two condensed phases: a liquid phase composed mainly of lithium and a solid phase constituted by the transition metal. A nonmetallic element added to such a system is expected to be partitioned between these two phases. The partitioning is described quantitatively by a distribution coefficient which is the ratio of the respective concentrations of the nonmetallic element in each phase.

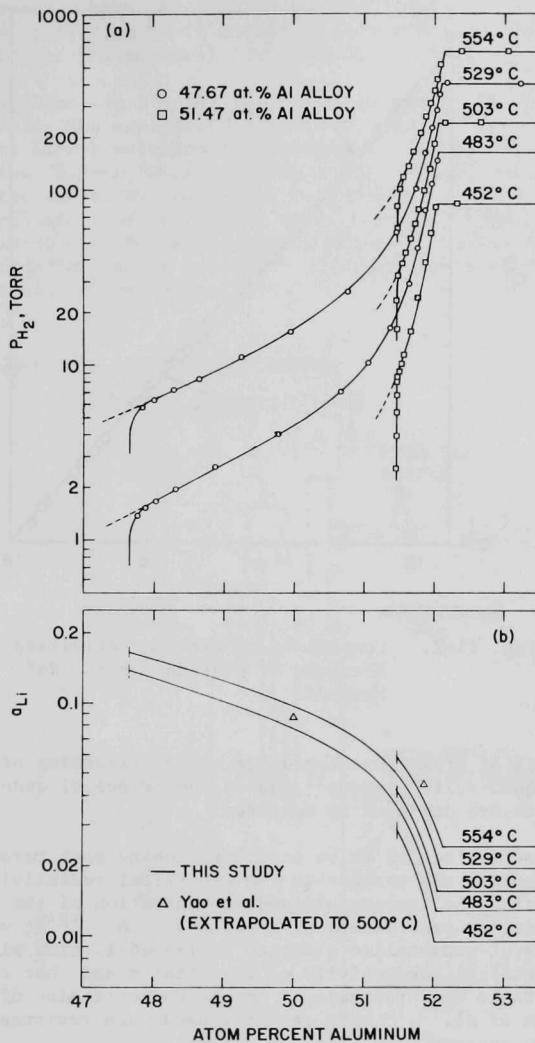


Fig. II-1. Isotherms in the Lithium-Aluminum System. Concentration Dependence of (a) Hydrogen Decomposition Pressures and (b) Lithium Activities.

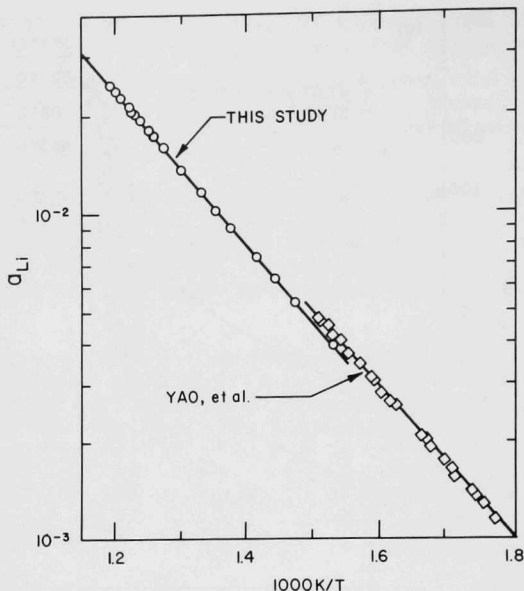


Fig. II-2. Comparison of Lithium Activities Measured by Hydridation and Emf Methods.

This parameter is of prime importance for an understanding of corrosion phenomena in liquid-solid systems¹¹ and is the principal quantity which these experiments are designed to measure.

The experimental method to be used for probing each ternary system consists of measuring the changes in the electrical resistivity of the liquid phase while varying the temperature and concentration of the nonmetallic element. In previous experiments by Arnol'dov *et al.*,¹² it was found that small quantities of nonmetallic elements in liquid lithium significantly altered the electrical conductivity of the lithium and that the observed change in resistance was proportional to the concentration of the nonmetallic element. Pulham *et al.*^{13,14} have recently used such resistance changes to study the binary systems Li-H, Li-D and Li-N.

The electrical resistance will be used to investigate the ternary systems in the following manner. Known quantities of a nonmetallic element will be added to liquid lithium and the resistance measured in order to produce a calibration curve of concentration *vs.* resistance. To a known amount of lithium-nonmetal solution will be added a known amount of transition metal. A portion of the nonmetal will enter the refractory metal, causing a reduction in the resistance of the lithium solution. The resistance change will be used to calculate the concentration of the

nonmetallic element in both the lithium and refractory metal; and, thus, the distribution coefficient. In addition, by monitoring the resistance with time, the kinetics of the nonmetal partitioning can be recorded.

The all-stainless-steel apparatus to be used in these experiments is shown in Fig. II-3. The equipment consists of a sealed pot (for equilibrating the Li-M-X solutions) connected to a three-meter length of thin-walled tubing (3.2-mm OD and 0.25-mm wall). Electrical leads attached to each end of the tubing are connected to a precise digital ohmmeter. By measuring the resistance of the tubing when it is empty and when it is filled with a lithium solution, the resistance of the solution can be calculated. With the present design of the apparatus, concentrations of the nonmetal as low as 10 ppm should be detectable.

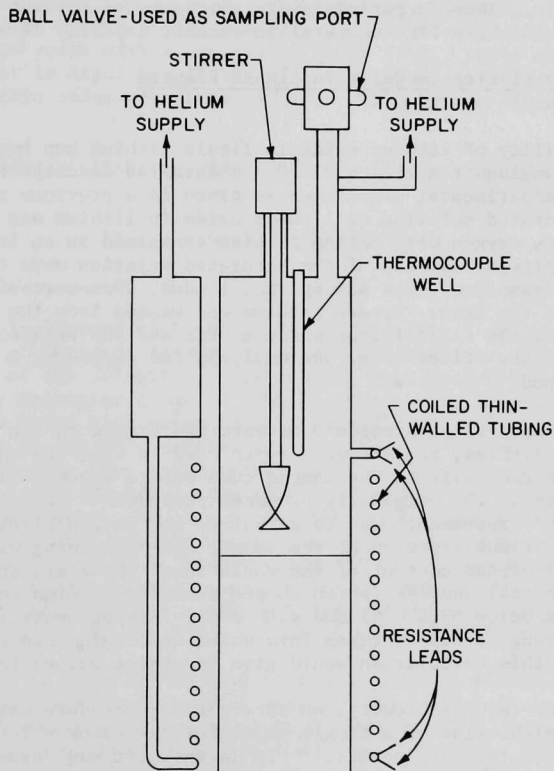


Fig. II-3. Stainless Steel Apparatus for Measuring the Resistivity of Liquid Lithium Solutions.

The apparatus is designed to fit into a furnace well which will be attached to a helium atmosphere glove box for easy access to the metal samples. Penetrations into the apparatus have been provided for a thermocouple well, a stirring rod, and a ball valve to be used as a sampling port. In addition, helium gas lines are connected to the pot and to the opposite end of the thin-walled tubing. By manipulating the pressure differential between the two ends of the tube, lithium can be forced into the tubing in order to measure the resistance and then returned to the pot for subsequent equilibrations.

Assembly of the apparatus is progressing. In preliminary experiments, the resistances of pure liquid lithium and lithium-nitrogen solutions will be measured to confirm proper operation of the apparatus. In addition, some experiments on the capability of reactive metals (*e.g.* yttrium) to getter the impurities from lithium will be necessary before full-scale operations begin. These experiments are necessary to develop a means of establishing a low base-line nonmetallic-element impurity level.

C. Solubility of Lithium Oxide in Liquid Lithium
(R. M. Yonco)

The solubility of lithium oxide in liquid lithium has been measured at temperatures ranging from 195 to 734°C. A detailed description of the apparatus and experimental procedure was given in a previous report.¹⁵ Briefly, a saturated solution of lithium oxide in lithium was prepared by reacting gaseous oxygen with molten lithium contained in an iron vessel. Twenty-eight filtered samples of the saturated solution were taken in special nickel sampling tubes having two, tandem, 2- μ m-pore-size filters at the open end of the tube. Excess lithium was washed from the outside of the tube with water, the first filter was cut off, and the entire sample, encapsulated in the filter tube, was analyzed for oxygen by a fast-neutron activation method.¹⁶

Since the analytical procedure detects the oxygen in the sample tube as well as in the lithium, it is necessary to have an accurate value for the oxygen blank attributable to the sample tube before solubilities in lithium can be calculated. The originally proposed procedure¹⁵ (which was supported by a preliminary experiment) was to calculate the oxygen blank as the product of the weight fraction of the sample tube remaining with the sample and the initial oxygen content of the whole tube. However, subsequent experience with real samples (which showed anomalously high solubility values at temperatures below $\sim 300^\circ\text{C}$ ¹⁵) and with control experiments (which measured the oxygen content of sample tubes into which no lithium had been admitted) indicated that this calculation would give incorrect values for the blank.

In light of this difficulty, an alternative procedure was selected, based on the calculation of a single value for the blank which could be applied to all of the data points.¹⁵ To do this, it was assumed that such a value would be temperature independent (as indicated by experience with the control samples). It was further assumed that there was a linear relationship between $\log x_{(\text{Li}_2\text{O})}$ and T^{-1} , where $x_{(\text{Li}_2\text{O})}$ is the mole fraction of lithium oxide and T is in kelvins. This would be true if Henry's law was obeyed, if the enthalpy of fusion of Li_2O was constant, and if no phase

change occurred within the temperature range of the experiment--all seemingly reasonable assumptions for the Li-Li₂O system. To the extent that these assumptions are true, there is justification for selecting a value for the oxygen blank which, when applied to each data point, would give a plot of $\log x_{(\text{Li}_2\text{O})}$ vs. T^{-1} that best conformed to a straight line.

Since the largest errors due to variations in the true value of the blank were expected to occur at the lowest oxygen levels, the value of the blank was calculated with each data point being weighted directly according to its estimated oxygen content. The value of the blank so derived is 0.44 mg and is well within the standard deviation of the values measured for the control samples, *i.e.*, 0.48 ± 0.09 mg.

A linear regression of the data points was then performed with the derived blank being applied to each point and with each point being weighted inversely according to its difference from the calculated value. By this procedure, a data point with a low oxygen level (*i.e.*, where the probability for a large error is high) has little effect on the constants in the solubility equation unless the true value of its blank is close to the derived value.

The solubility of lithium oxide in liquid lithium can be expressed by the equations

$$\ln S = 6.054 - 6669 T^{-1} \quad (5)$$

$$\log S^* = 6.992 - 2896 T^{-1} \quad (6)$$

where S is in mole percent of Li₂O and S^* is in weight parts per million of oxygen. A plot of the data is shown in Fig. II-4 and is compared with linear representations of the solubility measurements previously reported by Hoffman¹⁷ and by Konovalov *et al.*¹⁸ The uncertainty in the value of the derived blank is quite high relative to the small amount of oxygen present in samples taken at low temperatures and consequently the data points plotted in this region show considerable scatter. However, this uncertainty rapidly becomes insignificant as the amount of oxygen in the samples increases. Consequently, the data points taken at higher temperatures become sufficiently well established to permit extrapolation of the solubility curve to the freezing point of lithium, 180.6°C, with reasonable confidence. The solubility of oxygen at the melting point of lithium is indicated to be ~4 wppm. Extrapolation of the curves obtained by Hoffman and by Konovalov *et al.* yield values of 43 and 120 wppm, respectively, at this temperature.

The enthalpy of solution of Li₂O in liquid lithium calculated from the slope of the solubility curve is 55.6 kJ/mol. This value is better related to the estimated enthalpy of fusion of Li₂O (58 kJ/mol)¹⁹ than are the enthalpies of solution calculated from the works of Hoffman (38.3 kJ/mol) and of Konovalov *et al.* (38.2 kJ/mol). Since the enthalpies of fusion and of solution differ by an excess enthalpy value that is probably small, the agreement between these two values can be construed to support the accuracy of the slope of our solubility curve. It should be mentioned that the nine data points reported by Konovalov *et al.* show very poor correlation and that the agreement of their enthalpy value with that of Hoffman is, for the most part, the result of a rather arbitrary choice for the slope of the line representing their data.

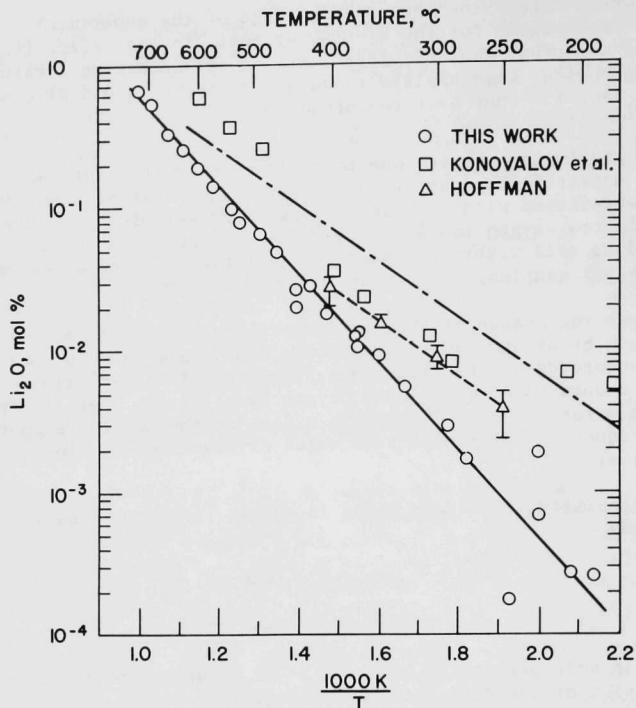


Fig. II-4. Solubility of Lithium Oxide in Liquid Lithium.

It should also be noted that Hoffman and Konovalov *et al.* filtered their samples through coarse porosity filters, 20 μm and 30-40 μm pore size, respectively. A comparison of the three sets of data shows that higher solubility values were consistently reported for samples taken through coarser filters. A possible explanation for this order might be that at least part of the undissolved lithium oxide exists as a fine, reasonably stable suspenoid which can pass through the coarse filters but is held back by the 2- μm -pore-size filters used in our work.

In consideration of the large number of data points collected over an extended temperature range, the agreement between the calculated enthalpy of solution and the estimated enthalpy of fusion, the use of 2- μm -pore-size filters for taking samples, and, especially, the use of the fast neutron activation method²⁰ for determining oxygen content, the preference for the solubility data produced by this study over those reported in previous studies seems justified. The solubility equations (Eqs. 5 and 6) define the theoretical limit of oxygen removal by cold trapping, although it is suggested that this limit might only be reached by filtration through fine porosity (2 μm or less) filters.

REFERENCES

1. J. R. Powell, *Tritium Recovery from Fusion Reactor Blankets Using Solid Lithium Compounds*, CONF-750989, III-197, 1975.
2. *High-Performance Batteries for Stationary Energy Storage and Electric-Vehicle Propulsion*, Progress Report for the Period Jan-Mar 1977, Argonne National Laboratory Report ANL-77-35.
3. R. Hultgren *et al.*, *Selected Values for the Thermodynamic Properties of Binary Alloys*, Amer. Soc. Met., Metals Park, Ohio, 1973, p. 1078.
4. E. Veleckis, E. H. Van Deventer, and M. Blander, *J. Phys. Chem.* **78**, 1933 (1974).
5. S. Aronson and F. J. Salzano, *Inorg. Chem.* **8**, 1541 (1969).
6. J. H. Owen and D. Randall, *Equilibrium and Kinetic Studies of Systems of Hydrogen Isotopes, Lithium Hydrides, Aluminum, and LiAlO₂*, CONF-750989, III-433, 1975.
7. *Chemical Engineering Division Physical Research on Liquid-Metal Systems Annual Report, July 1975-June 1976*, Argonne National Laboratory Report ANL-76-106, p. 5 (1977).
8. E. Veleckis, R. M. Yonco, and V. A. Maroni, *J. Less-Common Metals* **55**, 85 (1977).
9. K. M. Myles, F. C. Mrazek, J. A. Smaga, and J. C. Settle, *Proc. Symp. and Workshop on Advanced Battery Research and Design*, Argonne National Laboratory, Mar 22-23, 1976, ANL-76-8, p. 50B (1976).
10. N. P. Yao, L. A. Heredy, and R. C. Saunders, *J. Electrochem. Soc.* **118**, 1039 (1971).
11. D. L. Smith and K. Natesan, *Nucl. Tech.* **22**, 392 (1974).
12. M. N. Arnol'dov, M. N. Ivanovskii, V. I. Subbotin and B. A. Shmatko, *High Temp.* **5**, 723 (1967).
13. P. F. Adams, M. G. Down, P. Hubberstey and R. J. Pulham, *J. Less-Common Metals* **42**, 325 (1975).
14. P. Hubberstey, P. F. Adams, R. J. Pulham, M. G. Down and A. E. Thunder, *J. Less-Common Metals* **49**, 253 (1976).
15. *Chemical Engineering Division Physical Research on Liquid-Metal Systems Annual Report, July 1975-June 1976*, Argonne National Laboratory Report ANL-76-106 (1977).
16. D. J. Veal and C. F. Cook, *Anal. Chem.* **34**, 178 (1962).

17. E. E. Hoffman, *Solubility of Nitrogen and Oxygen in Lithium and Methods of Lithium Purification*, Special Technical Publication 272, p. 195, American Society for Testing Materials (1959).
18. E. E. Konovalov, N. I. Seliverstov, and V. P. Emel'yanov, *Solubility of Oxygen and Chlorine in Liquid Lithium*, Russ. Met. 3, 77 (1969).
19. D. R. Stull and H. Prophet, *JANAF Thermochemical Tables*, 2nd Ed., NSRDS-NBS 37, U. S. Department of Commerce (1971).
20. This study is being done in collaboration with J. H. DeVan and E. J. Strain of the Oak Ridge National Laboratory. The fast-neutron activation analyses were performed by E. J. Strain.

III. THERMOCHEMICAL STUDIES

(C. E. Johnson, W. N. Hubbard, G. K. Johnson,
K. Y. Kim* and R. G. Pennell†)A. Thermochemistry of Coal Components

(K. Y. Kim, R. E. Winans‡ W. N. Hubbard and C. E. Johnson)

The pyrolysis of coal yields a large number of complex aromatic materials. The relationship between these aromatic compounds and the structure of coal is not clear. Several investigators have oxidized coal to comparatively simple carboxylic acids which could be readily related to the molecular architecture of coal.^{1,2} These studies have resulted in the identification of certain aromatic compounds that constitute the structural building blocks of coal. Thermochemical data for these building-block molecules are of value since they contribute to a better understanding of coal structure, define possible paths of decomposition, and identify the effects that variables such as temperature might have on processes of coal liquefaction and gasification.

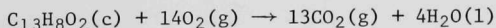
Because coal consists mainly of carbon, hydrogen, and oxygen,³ coal components consisting primarily of these elements have attracted our attention. Further, little thermochemical data are available on these compounds in spite of their importance in coal technology. Our initial calorimetric studies have focused on xanthone (xanthen-9-one), chromone, and benzo[b]naphtho[2,3-d]furan, which are oxygen-containing heteroaromatic units that have been identified in studies on the oxidative degradation of coal. Such data are necessary for establishing a basic set of data whereby thermodynamic properties of more complex organic species in coal and coal-conversion processes can be estimated.

1. Xanthone

The molar energy change due to the combustion of xanthone in oxygen is

$$\Delta E^{\circ}_{\text{c}}(\text{xanthone, c, 298.15}) = -6059.52 \pm 2.01 \text{ kJ mol}^{-1}$$

for the reaction



where the uncertainty in $\Delta E^{\circ}_{\text{c}}$ is equal to twice the combined standard deviations contributed by the xanthone combustion experiments, the calibration experiments, the uncertainty in the certificate value of benzoic acid, the estimate of the heat capacity of xanthone, and the weighings. Addition of the term ΔnRT ($\Delta n = -1$) to the energy change yields the enthalpy of combustion of xanthone:

$$\Delta H^{\circ}_{\text{c}}(\text{xanthone, c, 298.15}) = -6061.99 \pm 2.01 \text{ kJ mol}^{-1}$$

* Post-doctoral appointee.

† Undergraduate Research Program Participant, Goucher College, Towson, Md.

‡ Member of the ANL Chemistry Division.

Subtraction of 13 times the enthalpy of formation of carbon dioxide,⁴ $\Delta H_f^\circ(\text{CO}_2, \text{g}, 298.15) = -393.51 \pm 0.13 \text{ kJ mol}^{-1}$, and 4 times the enthalpy of formation of water,⁴ $\Delta H_f^\circ(\text{H}_2\text{O}, \text{l}, 298.15) = -285.830 \pm 0.042 \text{ kJ mol}^{-1}$, from $\Delta H_c^\circ(\text{xanthone}, \text{c}, 298.15)$ yields the enthalpy of formation of xanthone:

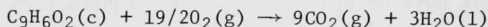
$$\Delta H_f^\circ(\text{xanthone}, \text{c}, 298.15) = -196.94 \pm 2.64 \text{ kJ mol}^{-1}$$

2. Chromone

The molar energy change due to the combustion of chromone in oxygen was found to be

$$\Delta E_c^\circ(\text{chromone}, \text{c}, 298.15) = -4186.29 \pm 0.94^* \text{ kJ mol}^{-1}$$

for the reaction



Addition of the term ΔnRT ($\Delta n = -1/2$) to the energy change yields the enthalpy of combustion of chromone:

$$\Delta H_c^\circ(\text{chromone}, \text{c}, 298.15) = -4187.53 \pm 0.94^* \text{ kJ mol}^{-1}$$

Subtraction of 9 times of $\Delta H_f^\circ(\text{CO}_2, \text{g}, 298.15)$ ⁴ and 3 times of $\Delta H_f^\circ(\text{H}_2\text{O}, \text{l}, 298.15)$ ⁴ from $\Delta H_c^\circ(\text{chromone}, \text{c}, 298.15)$ yields the enthalpy of formation of chromone,

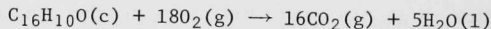
$$\Delta H_f^\circ(\text{chromone}, \text{c}, 298.15) = -211.55 \pm 1.51^* \text{ kJ mol}^{-1}$$

3. Benzo[b]naphtho[2,3-d]furan

The molar energy change for benzo[b]naphtho[2,3-d]furan (BNF) combustion is

$$\Delta E_c^\circ(\text{BNF}, \text{c}, 298.15) = -7760.38 \pm 1.84^* \text{ kJ mol}^{-1}$$

for the reaction:



Addition of the term ΔnRT ($\Delta n = 2$) to ΔE_c° yields the enthalpy of combustion of BNF,

$$\Delta H_c^\circ(\text{BNF}, \text{c}, 298.15) = -7765.34 \pm 1.84^* \text{ kJ mol}^{-1}$$

which leads to the enthalpy of formation of BNF,

$$\Delta H_f^\circ(\text{BNF}, \text{c}, 298.15) = 40.03 \pm 2.78 \text{ kJ mol}^{-1}$$

* Mean and standard deviation of the mean.

4. Estimation of $\Delta H_f^\circ(g)$ and ΔH_{sub} of Xanthone

Xanthone is an important compound not only in coal conversion technology but also in structural interpretations because of the presence of two kinds of oxygen groups forming a γ -pyrone ring. Even though the heat of formation has been estimated⁵⁻⁸ for some aromatic systems containing one or two oxygen atoms, no such estimates have been reported for the γ -pyrone series. The value of the standard enthalpy of formation of gaseous xanthone is needed for the interpretation of its properties. Since the required sublimation data are not available, an attempt was made to estimate $\Delta H_f^\circ(g)$. Table III-1 gives the group additivity values needed for the estimation of the enthalpy of formation of gaseous xanthone. Also shown in Table III-1 are the standard enthalpies of formation of the compounds from which the group additivity values were derived. The $\Delta H_f^\circ(g)$ values are quoted from Cox and Pilcher.⁹ The estimation of $\Delta H_f^\circ(\text{xanthone, g, 298.15})$ involved the addition of eight $[C_B(H)]$ bond values, one $[(CO)(C_B)_2 - (C_B)_4]_{6-R}$ bond value and one $[O(C_B)_2 - (C_B)_4]_{6-R}$ bond value. Thus, $\Delta H_f^\circ(\text{xanthone, g, 298.15}) = (8 \times 13.8) + (-102.9) + (-86.6) = -79.1 \text{ kJ mol}^{-1}$; the possible error was calculated to be $\pm 6.7 \text{ kJ mol}^{-1}$.

From the group additivity values given in Table III-1 and selected values from Benson,⁵ $\Delta H_f^\circ(g)$ was estimated for anthrone and several other quinones. These estimated values (with the experimental values⁹ given in parentheses) are in units of kJ mol^{-1} : *p*-benzoquinone, -122.2 (-122.6); 1,4-naphthoquinone, -108.8 (-110.9); 9,10-anthraquinone, -95.4 (-95.4); 5,12-tetracenequinone, -33.5 (-33.9); and anthrone, 32.2 (32.2*).


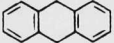
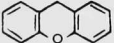
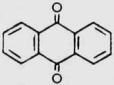
The heat of sublimation of a compound can be estimated if sublimation data are available for related compounds having similar molecular weights and structures. For xanthone (mol. wt. = 196.2), the heat of sublimation is estimated to be $112.1 \text{ kJ mol}^{-1}$ from the average of the heats for dibenzopyran (mol. wt. = 182.2, $\Delta H_{sub} = 112.1$)¹⁰ and anthraquinone (mol. wt. = 208.2, $\Delta H_{sub} = 112.1$).¹¹ The heat of sublimation of xanthone may also be estimated to be $117.8 \text{ kJ mol}^{-1}$ by taking the difference between the estimated $\Delta H_f^\circ(g)$ and the measured $\Delta H_f^\circ(c)$. Both estimates are in good agreement.

5. Resonance Energy

Resonance has the effect of increasing the stability of any molecule in which it is an important feature. Since xanthone is known to be one of the stable oxygen heteroaromatics in coal,^{1,2} its resonance energy was calculated to compare it with those of other aromatic compounds with similar molecular structures. The heat of combustion of xanthone(g) was calculated using the values of the bond contributions and their corrections as reported by Klages¹² and Wheland.¹³ The difference between the calculated value for the molar heat of combustion and the experimental value is regarded as the resonance energy. The resonance energies are presented in Table III-2.

* Because anthrone is yet to be measured, we use a second estimation technique, taking the average of $\Delta H_f^\circ(9,10\text{-dihydroanthracene})$ and $\Delta H_f^\circ(\text{anthraquinone})$.

Table III-1. Calculation of Group Additivity Values (kJ mol^{-1})

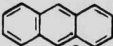
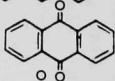
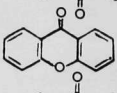
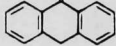
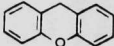
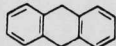
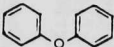
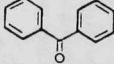
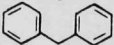
Compound	Structure	$\Delta H_f^\circ(\text{g})^a$	Group
Benzene		82.89 ± 0.54	$[\text{C}_B - (\text{H})]_6^b = \frac{82.89}{6}$ $= 13.82 (\pm 0.08)$
9,10-Dihydroanthracene		159.8 ± 4.6	$[\text{CH}_2(\text{C}_B)_2 - (\text{C}_B)_4]_{6-R}^c = \frac{159.8 - (8 \times 13.82)}{2}$ $= 24.6 (\pm 2.5)$
Dibenzopyran		48.5 ± 5.0	$[\text{O}(\text{C}_B)_2 - (\text{C}_B)_4]_{6-R} = 48.5 - (8 \times 13.82) - 24.6$ $= -86.7 (\pm 5.4)$
9,10-Anthraquinone		-95.4 ± 6.7	$[(\text{CO})(\text{C}_B)_2 - (\text{C}_B)_4]_{6-R} = \frac{-95.4 - (8 \times 13.82)}{2}$ $= -103.0 (\pm 3.4)$

^aValues taken from Ref. 9.

^b C_B represents the C atom in the benzene ring.

^c $_{6-R}$ indicates that the group is a part of a six-membered ring.

Table III-2. Heats of Combustion of Resonance Hybrids (kJ mol^{-1})

Compound	Structure	Heat of Combustion		Resonance Energy	Remark
		Observed ^a	Calculated		
Anthracene		7169.3	7515.7	346.4	planar
Anthraquinone		6557.2	6897.7	340.5	planar
Xanthone (Xanthen-9-one)		6174.3 ^b	6512.4	338.1	(planar)
Anthrone		6970.5 ^c	7293.1	322.6	planar
Dibenzopyran (Xanthene)		6593.1	6907.8	314.7	nonplanar
9,10-Dihydroanthracene		7383.9	7688.5	304.6	nonplanar
Diphenyl ether		6201.1	6507.8	306.7	nonplanar
Benzophenone		6605.3	6893.1	287.8	nonplanar
Diphenylmethane		7002.8	7288.5	285.7	nonplanar

^aTaken from Ref. 9.^bCalculated from observed $\Delta H_f^\circ(\text{c})$ and estimated ΔH_{sub} .^cEstimated taking the average of $\Delta H_f^\circ(\text{dihydroanthracene})$ and $\Delta H_f^\circ(\text{anthroquinone})$.

Biswas and Sen¹⁴ assumed that the xanthone molecule was planar in an X-ray study of its crystal and molecular structure. In addition, X-ray crystallographic studies of anthrone, which is similar to xanthone in molecular structure, led Srivastava¹⁵ to assign a planar structure to anthrone. Therefore, the enthalpy of formation and resonance energy of anthrone were estimated and compared with those of xanthone. The resonance stabilization energy of xanthone falls between those of anthraquinone and anthrone, both of which are known to be planar molecules. These findings suggest that xanthone may also be planar. The somewhat greater resonance energy of xanthone, when compared with that of anthrone, may be due to the contribution of the unshared electrons of the ether oxygen atom to the resonance conjugation. This is consistent with the reported results¹⁶⁻¹⁸ that the xanthone molecules, to which the γ -pyrone ring is coupled, are aromatic.

B. Thermochemistry of the Trifluorides of Scandium, Yttrium, Lanthanum and the Rare Earths

(W. N. Hubbard, R. G. Pennell, G. K. Johnson, D. W. Osborne,* and K. Y. Kim)

The thermodynamic properties of the compounds of the rare earths are important not only for the study and interpretation of periodic variations of chemical and physical properties but also in connection with practical problems encountered in fission-product chemistry. The properties of the fluorides are especially important in reprocessing of spent nuclear fuel by processes involving either volatile or molten fluorides.

The work described herein is part of a continuing effort to elucidate the thermodynamics of the trifluorides of scandium, yttrium, lanthanum, and the rare earths.¹⁹⁻²¹ Results of previous portions of the study have been published.

This report gives the experimental results of measurements of the enthalpies of formation of the trifluorides of lanthanum, praseodymium, neodymium, gadolinium, dysprosium, holmium, and erbium. Also reported are results of measurements of the high-temperature enthalpies, relative to 298.15 K, for lanthanum trifluoride.

1. Enthalpies of Formation

The enthalpy of formation measurements were made by combustions of the metal in fluorine to the trifluoride in a calorimeter. The apparatus and methods used for calibration of the system; for preparation, support, and ignition of the samples; and for analysis of the products were previously described.²² The combustion samples were high-purity metal foils obtained from the ERDA Ames Laboratory. During combustion, the sample foil was supported by the appropriate metal trifluoride. These pure trifluorides were also prepared at the Ames Laboratory.

* Member of the ANL Chemistry Division.

Table III-3 summarizes the derived results for the fluorine-bomb combustions of lanthanum, neodymium, erbium, praseodymium, gadolinium, dysprosium and holmium. In that table, ΔE_f° , ΔH_f° , ΔS_f° , and ΔG_f° represent, respectively, the standard energy, enthalpy, entropy, and Gibbs free energy of formation of the rare-earth trifluorides from the elements at 298.15 K.

2. High-Temperature Enthalpy Data

Considerable relative enthalpy data for the rare earth trifluorides have been measured in the past by Spedding and his co-workers at the ERDA Ames Laboratory.²³ Just recently, low-temperature heat capacity measurements were completed by D. W. Osborne and H. E. Flotow²⁴ of the ANL Chemistry Division for the trifluorides of lanthanum, praseodymium and neodymium. While the available high-temperature data for praseodymium and neodymium can be easily combined with the low-temperature data in a logical manner, the high-temperature data for lanthanum trifluoride cannot be combined with the low-temperature data; also, the shape of the curve indicating the change in heat capacity with temperature does not rise in the same manner as the rest of the lanthanide trifluorides. In an effort to resolve this problem, high-temperature drop-calorimetric measurements were made on LaF_3 .

The results from our measurements on LaF_3 combined well with the low-temperature measurements of Osborne and Flotow;²⁴ however, the Ames data²³ were much higher at the low-temperature end. Our data and the data of Ames Laboratory were in substantial agreement above 1000 K, thereby lending support to the Ames data in the high-temperature region. The fact that the heat capacity of lanthanum trifluoride is much higher than those of the other rare earth trifluorides suggests that there may be one or more previously unsuspected thermochemical contributions to the heat capacity at these higher temperatures.

Values of the relative enthalpy at 320 and 350 K calculated from the low-temperature data,²⁴ some values from Spedding and Henderson's equation²³ for temperatures above 1000 K, and values of the relative enthalpy measured in this investigation were used to derive a general equation which is considered the best representation of the combined data for lanthanum trifluoride. The equation is

$$H_T - H_{298.15} = A + BT + CT^2 + DT^3 + ET^4 + FT^5$$

in which the coefficients have the values indicated: $A = -2.234681 \times 10^4$; $B = 5.369166 \times 10^1$; $C = 9.452303 \times 10^{-2}$; $D = -8.965778 \times 10^{-5}$; $E = 4.131366 \times 10^{-8}$; and $F = -5.963629 \times 10^{-12}$. From this equation the relevant high-temperature thermodynamic data can be calculated.

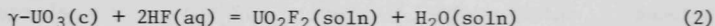
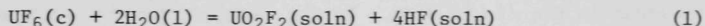
Table III-3. Derived Results for the Rare-Earth Trifluorides at 298.15 K

Cpd	ΔE_f° , kJ mol ⁻¹	ΔH_f° , kJ mol ⁻¹	ΔS_f° , J K ⁻¹ mol ⁻¹	ΔG_f° , kJ mol ⁻¹
LaF ₃	-1695.8 ± 2.0	-1699.5 ± 2.0	-253.9 ± 2.5	-1623.8 ± 2.1
PrF ₃	-1684.4 ± 2.6	-1689.1 ± 2.6	-256.0 ± 4.2	-1612.8 ± 2.9
NdF ₃	-1675.7 ± 1.9	-1679.4 ± 1.9	-254.7 ± 4.2	-1603.5 ± 2.3
GdF ₃	-1695.6 ± 2.3	-1699.3 ± 2.3	-252.0 ± 5.1	-1624.2 ± 2.8
DyF ₃	-1688.3 ± 1.9	-1692.0 ± 1.9	-258.9 ± 5.1	-1614.8 ± 2.4
HoF ₃	-1694.1 ± 2.3	-1697.8 ± 2.3	-259.0 ± 5.3	-1620.6 ± 2.8
ErF ₃	-1689.9 ± 1.9	-1693.6 ± 1.9	-257.2 ± 5.1	-1616.9 ± 2.4

C. Uranium Compounds: The Enthalpies of Formation of γ -UO₃ and UF₆
(G. K. Johnson)

In the course of a recent assessment of the thermochemistry of γ -UO₃, Cordfunke, Ouweltjes, and Prins²⁵ pointed out that the standard enthalpy of formation of γ -UO₃, $\Delta H_f^\circ(\text{UO}_3, \text{c}, \gamma, 298.15 \text{ K})$, based on solution calorimetric measurements in H₂SO₄ by Fitzgibbon *et al.*,²⁶ was in excellent agreement with the result based on a study of the high-temperature decomposition of γ -UO₃ to U₃O₈ and O₂(g) by Cordfunke and Aling.²⁷ These results, however, did not agree with the results based on the HF solution calorimetric measurements of Popov *et al.*²⁸ and Vidavskii *et al.*²⁹ Cordfunke *et al.* suggested that the discrepancy, about 7 kJ mol⁻¹, might be due to the uncertain value for $\Delta H_f(\text{HF}, \text{aq})$. This large disagreement prompted us to redetermine $\Delta H_f^\circ(\gamma\text{-UO}_3)$ by HF solution calorimetry.

The calorimetric measurements involved the hydrolysis of UF₆ and the reaction between γ -UO₃ and HF(aq), as follows:



Thus, combination of the measured enthalpy changes for the above reactions, along with ΔH_f for UF₆(c), HF(aq), and H₂O(l), and a small enthalpy of dilution correction, yields $\Delta H_f^\circ(\gamma\text{-UO}_3)$.

The calorimetric reaction experiments with HF(aq) were performed with the LKB-8700 precision calorimetric system equipped with a gold reaction vessel. High-purity samples of UF₆ and γ -UO₃ in which no detectable impurities could be found were used in this work. The UF₆ samples were contained in capsules constructed of a chlorotrifluoroethylene polymer and the UO₃ samples in glass ampoules. All reactions proceeded rapidly and completely.

The value calculated for $\Delta H_f^\circ(\gamma\text{-UO}_3)$, $-1213.1 \pm 2.6 \text{ kJ mol}^{-1}$, is in good agreement with the combined results of Popov *et al.*²⁸ and Vidavskii *et al.*,²⁹ -1214.7 ± 2.9 , which were determined in a similar HF cycle. The results, however, are in disagreement with the generally accepted values of Cordfunke *et al.*,²⁷ $-1223.8 \pm 0.8 \text{ kJ mol}^{-1}$, and Fitzgibbon *et al.*,²⁶ $-1223.0 \pm 2.5 \text{ kJ mol}^{-1}$.

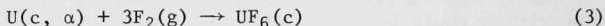
After considerable discussion, it became evident that our derived result for γ -UO₃ could not be correct, and we were left with several possible explanations for the discrepancy. These included the following: (1) the possibility that the solution chemistry of UF₆ and UO₃ was not well understood and that different species might be formed when these compounds were reacted with HF(aq); (2) the possibility that there was a 10 kJ mol⁻¹ error in $\Delta H_f^\circ(\text{UF}_6, \text{c})$; and (3) the possibility that there was a 1.7 kJ mol⁻¹ error in $\Delta H_f(\text{HF}, \text{aq})$, which entered the cycle 6 times. After much discussion, it was decided that an error in the enthalpy of formation of UF₆ was the most probable of the possible errors even though there were two independent determinations^{30,31} of $\Delta H_f^\circ(\text{UF}_6)$ that were in excellent agreement. These determinations involved a fluorine bomb calorimetric investigation at this laboratory,³⁰ $\Delta H_f^\circ(\text{UF}_6, \text{c}) = -2186.7 \pm 1.8 \text{ kJ mol}^{-1}$, and a fluorine flow

calorimetric investigation³¹ at Fulmer Research Institute, $\Delta H_f^\circ(\text{UF}_6, c) = -2185.3 \pm 2.5 \text{ kJ mol}^{-1}$. Despite this good agreement, a redetermination of the enthalpy of formation of UF_6 by fluorine bomb calorimetry was undertaken.

A sample of high-purity uranium in the form of a 0.32-cm-dia rod was cleaned of surface oxidation by treatment with 5M HNO_3 and stored thereafter in a high-purity helium-atmosphere glove box. Analysis of the sample yielded the following results for impurities (in ppm): O, 30; N, 16; H, <5; C, 35; Al, 12; Ca, 6; Fe, 12; Mo, 1; Si, 10; Sn, 2; and Mg, 1.

A combustion technique was developed in which stacked foils of tungsten were used both as an auxiliary combustion aid and sample support. The uranium rod was placed on the top of three foils and after ignition, the rod burned through each foil in order, finally falling onto a nickel dish. Combustions were carried out in a single-chamber bomb charged to 12.9 atm with fluorine. By the time the sample finally contacted the Ni, there was no longer any molten uranium, which would have readily alloyed with the nickel; only partially fluorinated uranium, UF_3 , UF_4 and UF_5 , was left as residue in the nickel dish. In the calorimetric combustions the amount of partially fluorinated residue varied between 10 and 110 mg. This combustion procedure, which resulted in a very "hot" and rapid combustion, differed significantly from that used previously,³⁰ which was essentially a very slow reaction. In that procedure, very dilute fluorine was used and the sample was not allowed to get hot enough to melt. The reaction usually quenched before half of the uranium had reacted.

Seven combustions of the uranium sample in fluorine were performed according to the reaction



The derived results for crystalline and gaseous UF_6 are present in Table III-4, where the symbols in the table have their usual significance. The entropies, $S^\circ(298.15 \text{ K})$ for $\text{U}(c)$, $\text{F}_2(g)$, $\text{UF}_6(l)$, and $\text{UF}_6(g)$ were taken to be 50.2,³² 202.7,³³ 227.6³⁴ and 378.2³⁴ $\text{J K}^{-1} \text{ mol}^{-1}$, respectively. The enthalpy of sublimation of $\text{UF}_6(c)$ was taken to be $49.6 \pm 0.4 \text{ kJ mol}^{-1}$.³⁵

The result obtained in this study for $\Delta H_f^\circ(\text{UF}_6, c)$ is approximately 10.4 kJ mol^{-1} more negative than the previous calorimetric results.³⁰ We are unable to account for this difference at this time. Two combustion experiments were performed using some of the samples employed in the earlier work and the result obtained for $\Delta H_f^\circ(\text{UF}_6, c)$ was $-2198.3 \text{ kJ mol}^{-1}$, in good agreement with our recent data. The difference in results obtained in the earlier work is therefore not due to the use of a different sample but, presumably, must be associated with the combustion technique.

When the more negative value for $\Delta H_f^\circ(\text{UF}_6, c)$ is used in the calculation of the $\gamma\text{-UO}_3$ cycle, a value of $-1224.1 \pm 2.6 \text{ kJ mol}^{-1}$ is obtained for $\Delta H_f^\circ(\gamma\text{-UO}_3)$. This result is in excellent agreement with the accepted values for $\gamma\text{-UO}_3$ and hence there is strong support for the correctness of the more negative result for $\Delta H_f^\circ(\text{UF}_6, c)$ derived in this work.

Table III-4. Derived Results for UF_6 at 298.15 K

Thermodynamic Function	$\text{UF}_6(\text{c})$	$\text{UF}_6(\text{g})$
$\Delta E_c^\circ/M, \text{ J g}^{-1}$	-9201.5 ± 7.7	
$\Delta E_f^\circ, \text{ kJ mol}^{-1}$	-2190.3 ± 1.8	-2143.3 ± 1.9
$\Delta H_f^\circ, \text{ kJ mol}^{-1}$	-2197.8 ± 1.8	-2148.2 ± 1.9
$\Delta S_f^\circ, \text{ J K}^{-1} \text{ mol}^{-1}$	-430.5 ± 2.1	-279.9 ± 0.8
$\Delta G_f^\circ, \text{ kJ mol}^{-1}$	-2069.4 ± 1.9	-2064.7 ± 1.9

D. Thermochemical Study of Cs_3CrO_4 and Cs_4CrO_4
(K. Y. Kim, G. K. Johnson, and C. E. Johnson)

Considerable interest has been directed toward the Cs-Cr-O system because cesium chromates, such as Cs_2CrO_4 , $\text{Cs}_2\text{Cr}_2\text{O}_7$, Cs_3CrO_4 , Cs_4CrO_4 and Cs_5CrO_4 ,³⁶ may form in irradiated nuclear fuel pins as a result of chemical interactions between fission-product cesium and the stainless-steel cladding. Thermochemical data for these compounds would be of value in connection with the elucidation of the surface scaling or cesium intergranular penetration of the steel cladding. Reliable thermodynamic data are also valuable in predicting the compounds most likely to be formed. Even though the Cs-Cr-O system has attracted the attention of many researchers,³⁶⁻⁴⁰ no reliable thermochemical data were available on Cs_3CrO_4 and Cs_4CrO_4 in spite of their importance. Therefore, solution calorimetry, using XeO_3^* as an oxidant, was employed to determine the standard enthalpies of formation for Cs_3CrO_4 and Cs_4CrO_4 .

1. Calorimetric Experiments for Cs_3CrO_4 and Cs_4CrO_4

The reactions of $\text{Cs}_3\text{CrO}_4^\dagger$ and $\text{Cs}_4\text{CrO}_4^\dagger$ crystals with XeO_3 in CsOH solutions were conducted in the LKB Solution Calorimeter. The samples were loaded into glass ampoules in the helium-atmosphere glove box and the ampoules were sealed with silicone rubber stoppers⁵ and wax. The XeO_3 -CsOH solution in the calorimeter was saturated with $\text{Xe}(\text{g})$ before the experiment to ensure that all the Xe formed during reaction would leave the calorimeter as a gas. Thus, corrections for the appreciable solubility of Xe were avoided.

*The assistance of E. H. Appelman, Chemistry Division, ANL, in the preparation of this material is acknowledged.

†The preparation of these materials by Dr. B. A. Phillips of AERE, Harwell, England, is acknowledged.

The standard enthalpies of formation of Cs_3CrO_4 and Cs_4CrO_4 were derived from the Hess cycles. The results from the calorimetric experiments and calculations are given in Table III-5, where the entries in the table have their usual significance.

Table III-5. Calorimetric Results and Enthalpy of Formation of Cesium Chromates

	Cs_3CrO_4	Cs_4CrO_4
$\Delta H_r/M, \text{ J g}^{-1a}$	-524.68 ± 1.59^b	-985.70 ± 1.85^b
Impurity Correction, J g^{-1}	-0.11 ± 0.25	--- ^c
$\Delta H_r, \text{ kJ mol}^{-1}$	-270.12 ± 1.65^d	-638.36 ± 2.40^d
$\Delta H_f^2(c, 298.15 \text{ K}), \text{ kJ mol}^{-1}$	-1542.7 ± 2.6^d	-1587.6 ± 3.1^d

^aHeat of reaction of cesium chromate with the $\text{XeO}_3\text{-CsOH}$ solution.

^bUncertainty is the standard deviation of the mean.

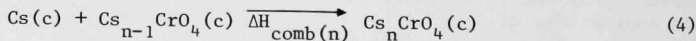
^cImpurity corrections are yet to be defined.

^dUncertainty is twice the standard deviation of the mean.

After the Cs_3CrO_4 and Cs_4CrO_4 crystals reacted with the XeO_3/CsOH aqueous solution in the calorimeter, the product solutions were checked with respect to the CrO_4^{2-} concentration by employing a Cary-14 Spectrophotometer. Within the reproducibility (about $\pm 0.3\%$) of the spectrophotometer, all the reactions were confirmed as having proceeded 100% in the conversion of all the chromium species to Cr(VI) .

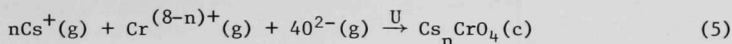
2. Discussion

The heats of formation of Cs_3CrO_4 and Cs_4CrO_4 measured in our laboratory are in good agreement with the results of oxygen potential measurements by Knights and Phillips,⁴⁰ which are -1504 ± 130 and $-1542 \pm 140 \text{ kJ mol}^{-1}$, respectively. Since the compounds Cs_3CrO_4 and Cs_4CrO_4 were synthesized by combining cesium with Cs_2CrO_4 , the heats of reactions of such compounds may be calculated from the following reaction.



For the formation of Cs_3CrO_4 , $\Delta H_{\text{comb}}(3)$ is $-112.71 \text{ kJ mol}^{-1}$ and for Cs_4CrO_4 , $\Delta H_{\text{comb}}(4)$ is $-44.9 \text{ kJ mol}^{-1}$. It has been observed that the heat of reaction of Cs metal with $\text{Cs}_{n-1}\text{CrO}_4(c)$ is drastically decreased as n is increased and may ultimately reach zero enthalpy change. This may imply that the Cs atoms are simply mixed with $\text{Cs}_{n-1}\text{CrO}_4$ molecules when the Cs atoms are overcrowded around the chromate complex ions. The reduction of chromium should not always be possible by addition of cesium metal to cesium chromates.

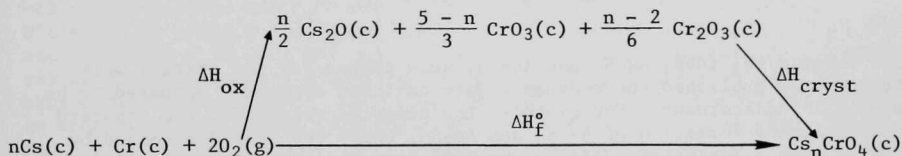
The lattice energies, U , calculated by applying the conventional method to Eq. 5



are -32376 ± 54 , -24200 ± 54 , and -17644 ± 54 kJ mol^{-1} for Cs_2CrO_4 , Cs_3CrO_4 , and Cs_4CrO_4 , respectively. The calculated decreasing lattice energies suggest that the distance between cesium and chromate ions may become greater as more cesium is added. Ionic sizes for Cr^{6+} , Cr^{5+} and Cr^{4+} are quite close to each other ranging from 0.52 to 0.56 \AA^{41} and the geometry of the CrO_4^{2-} , CrO_4^{3-} , and CrO_4^{4-} molecules are all tetrahedral.⁴² Therefore, these three complex ions can be assumed to be almost the same size.

If Cs_5CrO_4 can be prepared according to reaction 4, the combination energy $\Delta H_{\text{comb}}(5)$ for $n = 5$ may be estimated to be lower than -17.9 kJ mol^{-1} from the values $\Delta H_{\text{comb}}(3)$ and $\Delta H_{\text{comb}}(4)$. Using this value, the standard enthalpy of formation of Cs_5CrO_4 , $\Delta H_f^\circ(\text{Cs}_5\text{CrO}_4, \text{c}, 298.15)$, can be estimated to be -1605.5 kJ mol^{-1} .

The compound Cs_nCrO_4 may be considered to be synthesized through a hypothetical route:



In this process, ΔH_{ox} is defined as the sum of enthalpies of formation of oxides and ΔH_{cryst} as that of $\text{Cs}_n\text{CrO}_4(\text{c})$ formation from the oxides. The ΔH_{cryst} values can be calculated from the measured ΔH_f° less the calculated ΔH_{ox} . The square root values of ΔH_{cryst} for $n = 2$ through 4 were plotted against mole fractions of Cs_2O to extrapolate $\Delta H_{\text{cryst}}(5)$ for $n = 5$ in Fig. III-1. A value of 242 ± 20 kJ mol^{-1} was obtained for $\Delta H_{\text{cryst}}(5)$. Employing this value, $\Delta H_f^\circ(\text{Cs}_5\text{CrO}_4, \text{c}, 298.15)$ was estimated to be -1604 ± 20 kJ mol^{-1} which is in good agreement with the ΔH_f° value obtained by using the estimated $\Delta H_{\text{comb}}(5)$ value.

The seventh ionization potential of chromium is so high⁴² that no Cr(VII) compound has ever been synthesized. Therefore, it may be very difficult for CsCrO_4 to exist at 298.15 K.

E. The Thermodynamic Properties of the Arsenic Sulfides (G. K. Johnson, W. N. Hubbard and C. E. Johnson)

The thermodynamic properties of sulfides are of interest in the development of geothermal energy resources because of the environmental and corrosion problems associated with them. We have undertaken a program to determine the thermodynamic properties of a number of sulfides using fluorine bomb calorimetry to determine their enthalpies of formation at 298.15 K and drop calorimetry to determine their high-temperature thermodynamic functions.

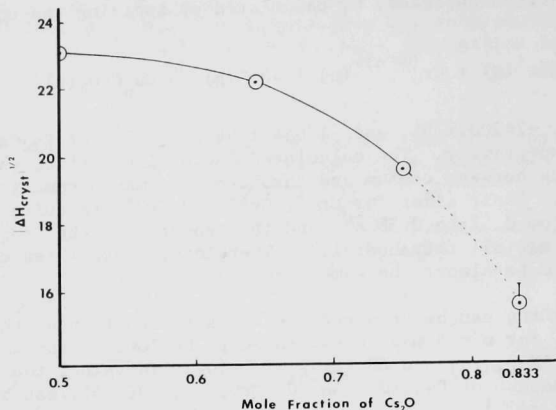


Fig. III-1. Plot of $(\Delta H_{\text{cryst}})^{1/2}$ vs. Mole Fraction of Cs_2O [ordinate units are $(\text{kJ mol}^{-1})^{1/2}$].

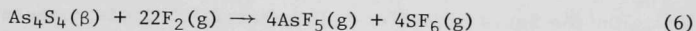
The arsenic sulfides, As_4S_4 and As_2S_3 , were chosen for the initial work because the published thermodynamic data on these compounds appeared to be especially discordant. For example, the accepted values for the standard enthalpies of formation of As_4S_4 and As_2S_3 , which had been determined by oxygen bomb calorimetry, differed by 100% from the results available from equilibrium studies. In addition, there were no high-temperature enthalpy measurements available for As_4S_4 .

In nature As_4S_4 occurs as the mineral realgar and As_2S_3 occurs as the mineral orpiment. It is extremely difficult to obtain the natural minerals in adequate purity for calorimetric work; hence, it was necessary to work with compounds prepared in the laboratory by reacting high-purity arsenic with sulfur. The laboratory preparations, however, do not yield substances in the same crystalline forms as the natural minerals. The As_4S_4 undergoes an irreversible transformation at 553 K from the low-temperature form (α) to the high-temperature form (β), which is the crystalline form produced in the laboratory. The laboratory preparation of As_2S_3 results in a noncrystalline glass. The calorimetric samples were prepared by heating stoichiometric amounts of high-purity arsenic and sulfur in an evacuated and sealed quartz tube for several days at 673 K. The samples were handled entirely in a helium atmosphere glove box after preparation.

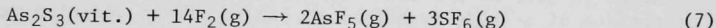
Preliminary combustion experiments established that the arsenic sulfides reacted spontaneously and completely in high-pressure fluorine to form only gaseous AsF_5 and SF_6 . It was therefore necessary to use a two-chambered reaction vessel⁴³ in which the fluorine could be kept separated from the sulfide until it was desired to initiate the reaction in the calorimeter.

For the drop-calorimetric experiments with $\beta\text{-As}_4\text{S}_4$ (the high-temperature properties of vitreous As_2S_3 will be determined at a later date), it was determined that a platinum-10% rhodium capsule was compatible with As_4S_4 below ~ 900 K. Above this temperature there was some attack on the capsule material. The overall operation of the 1500 K drop calorimetric system⁴⁴ was checked by performing a series of drop experiments with NBS standard sapphire over the temperature range from 373 to 1273 K. The agreement over this entire range was excellent. Because of the low temperature studied with As_4S_4 , it was necessary to use 1.3 kPa of helium in the furnace and calorimeter to help establish thermal equilibrium.

Eight calorimetric combustions of $\beta\text{-As}_4\text{S}_4$ and six combustions of vitreous As_2S_3 in fluorine were performed according to the reactions:



and



The derived results are given in Table III-6. The auxiliary data needed to derive the results in Table III-6 are $\Delta H_f^\circ(\text{AsF}_5, \text{g}) = -1236.75 \pm 0.79 \text{ kJ mol}^{-1}$,⁴⁵ $\Delta H_f^\circ(\text{SF}_6, \text{g}) = -1220.8 \pm 1.0 \text{ kJ mol}^{-1}$,⁴⁶ $S^\circ(\text{As}_4\text{S}_4, \beta) = 254.0 \pm 2.5 \text{ J K}^{-1} \text{ mol}^{-1}$,⁴⁷ $S^\circ(\text{S, rhomb}) = 31.80 \text{ J K}^{-1} \text{ mol}^{-1}$,⁴⁸ and $S^\circ(\text{As, } \alpha) = 35.15 \text{ J K}^{-1} \text{ mol}^{-1}$. There are currently no available entropy values for vitreous As_2S_3 despite the fact that several low-temperature heat-capacity studies⁴⁹⁻⁵⁰ have been performed. We are currently attempting to combine the available data and derive a value for $S^\circ(\text{As}_2\text{S}_3, \text{vit.}, 298.15 \text{ K})$.

Table III-6. Derived Results for the Arsenic Sulfides at 298.15 K

Thermodynamic Function	$\beta\text{-As}_4\text{S}_4$	Vit. As_2S_3
$(\Delta E_C^\circ/M), \text{ J g}^{-1}$	-22577 ± 10	-24567.4 ± 9.8
$\Delta E_C^\circ, \text{ kJ mol}^{-1}$	-9661.3 ± 4.3	-6044.1 ± 2.4
$\Delta H_C^\circ, \text{ kJ mol}^{-1}$	-9696.0 ± 4.3	-6066.4 ± 2.4
$\Delta H_f^\circ, \text{ kJ mol}^{-1}$	-134.2 ± 6.7	-69.5 ± 4.2
$\Delta S_f^\circ, \text{ J K}^{-1} \text{ mol}^{-1}$	-13.8 ± 3.1	
$\Delta G_f^\circ, \text{ kJ mol}^{-1}$	-130.1 ± 6.8	

Twenty-three drop calorimetric experiments, twelve below the melting point, ten above the melting point, and one in which the sample was partially melted, were performed with $\beta\text{-As}_4\text{S}_4$. The enthalpy data above the melting point were fit by the method of least squares to an equation of the form

$H_T - H_{298.15} = A + BT + CT^2 + DT^3$. The values of the coefficients are $A = -7.142681 \times 10^4$, $B = 3.045239 \times 10^2$, $C = -1.304292 \times 10^{-1}$ and $D = 1.1152568 \times 10^{-4}$. The enthalpy data below the melting point were fit by the method of least squares to an equation of the form $H_T - H_{298.15} = A + BT + CT^2 + DT^3 + ET^4$. The values of the coefficients are $A = -4.6923346 \times 10^4$, $B = 1.0795196 \times 10^2$, $C = 2.4483326 \times 10^{-1}$, $D = -3.1985772 \times 10^{-4}$, and $E = 1.835951 \times 10^{-7}$. The equation for the enthalpy data for the solid was constrained so that $H_T - H_{298.15} = 0$ at $T = 298.15$ K and $C_p(298.15)$, which is the slope of the $H_T - H_{298.15}$ curve, equals 288.11. The latter is the value obtained from low-temperature adiabatic calorimetry.⁴⁷ The enthalpy and entropy of fusion of β -As₄S₄ at the melting point, 580.15 K,⁵¹ were derived to be 26.67 ± 0.20 kJ mol⁻¹ and 45.97 ± 0.34 J K⁻¹ mol⁻¹, respectively.

On the basis of differential thermal analysis measurements, Street and Munir⁵¹ have reported the enthalpy of the irreversible α to β transition in As₄S₄ to be 3.47 ± 0.17 kJ mol⁻¹ at 553 K. This datum plus the results obtained in this work would allow us to derive the exact thermodynamic properties of α -As₄S₄ (realgar) at 553 K. If in addition we assume that the enthalpy and entropy functions of α - and β -As₄S₄ are equal between 553 and 298.15 K, then the thermodynamic properties of α -As₄S₄ can be obtained at 298.15 K as well. This assumption is probably valid since the two forms have very similar crystal structures. It is certainly valid well within the uncertainties involved. Thus the following thermodynamic properties are derived for α -As₄S₄ (realgar) at 298.15 K; $\Delta H_f^\circ = -137.7 \pm 7.0$ kJ mol⁻¹; $S^\circ = 247.7 \pm 2.6$ J K⁻¹ mol⁻¹; $\Delta S_f^\circ = -20.1 \pm 3.2$ J K⁻¹ mol⁻¹ and $\Delta G_f^\circ = -131.7 \pm 7.0$ kJ mol⁻¹.

The enthalpies of formation derived in the present work are compared with available literature results in Table III-7. The oxygen bomb calorimetric investigation of Britzke *et al.*⁵² is extremely difficult to interpret. The products of their combustions were mixtures of As₂O₃, As₂O₅, SO₂, SO₃, As₂O₃·SO₃ and As₂O₃·As₂O₅. This presents a very difficult analytical problem to the investigator and it is not too surprising that the results are in error. The selected values of Mills⁵³ and the Bureau of Standards⁴⁷ are attempts to update the data of Britzke *et al.*; however, these selected values also appear to be in error. Our data for As₄S₄ are in excellent agreement with the equilibrium data of Barton⁵⁴ and in fair agreement with the equilibrium data of Jellinek *et al.*⁵⁵ For As₂S₃, our data tend to support the less negative equilibrium result of Barton, although the numbers are not strictly comparable because of the difference in physical states. It is not likely, however, that taking into account the crystalline-to-amorphous transition would be enough to bring our result in accord with those of Barton. It is our opinion that the fluorine bomb calorimetric results are to be preferred over the other methods because of the uncomplicated nature of the fluorine combustion experiments.

There are no previous high-temperature results with which our drop-calorimetric data for β -As₄S₄ can be compared. Street and Munir⁵¹ have, however, reported an enthalpy of fusion of β -As₄S₄ of 25.1 ± 1.3 kJ mol⁻¹ based on DTA measurements. This result is in agreement with our enthalpy of fusion; but owing to the nature of the DTA experiment, their result is not as reliable.

Table III-7. Comparison of ΔH_f° Results for Arsenic Sulfides

Data Source	ΔH_f° , kJ mol ⁻¹		
	α -As ₄ S ₄	As ₂ S ₃ (orpiment)	As ₂ S ₃ (glass)
Britzke <i>et al.</i> (Ref. 52)	-241.8	-145.6	-
NBS-270-3, selected value (Ref. 33)	-285.3	-169.0	-
Mills, selected value (Ref. 53)	-284 ± 42	-167 ± 21	-
Barton (Ref. 54)	-142	-115	-
Jellinek <i>et al.</i> (Ref. 55)	-163 ± 42		-
This study	-137.7 ± 7.0		69.5 ± 4.2

REFERENCES

1. R. Hayatsu, R. G. Scott, L. P. Moore and M. H. Studier, *Nature* **257**, 378 (1975).
2. R. Hayatsu, R. E. Winans, R. G. Scott, L. P. Moore and M. H. Studier, submitted to *Fuel*, in press.
3. D. W. Van Krevelen, *Coal*, Elsevier Publishing Co., Amsterdam (1961).
4. CODATA Bulletin No. 17, ICSU CODATA, Paris (1976).
5. S. W. Benson, *Thermochemical Kinetics*, 2nd Ed., Wiley, New York (1976).
6. S. E. Stein, D. M. Golden and S. W. Benson, *J. Phys. Chem.* **81**, 314 (1977).
7. R. Shaw, D. M. Golden and S. W. Benson, *Predictive Scheme for Thermochemical Properties of Polycyclic Aromatic Hydrocarbons*, Appendix C, Report No. FE-2202-2, Stanford Research Institute, May 1977.
8. W. C. Herndon, *Thermochim. Acta* **8**, 225 (1974).
9. J. D. Cox and G. Pilcher, *Thermochemistry of Organic and Organometallic Compounds*, Academic Press, London (1970).
10. R. C. Cass, S. E. Fletcher, C. T. Mortimer, H. D. Springall and T. R. White, *J. Chem. Soc.* 1406 (1958).

11. A. Magnus, Z. Phys. Chem. (Frankfurt) 9, 141 (1956).
12. F. Klages, Chem. Ber. 82, 358 (1949).
13. G. W. Wheland, *Resonance in Organic Chemistry*, Wiley, New York (1955).
14. S. C. Biswas and R. K. Sen, Indian J. Pure Appl. Phys. 7, 408 (1969).
15. S. N. Srivastava, Acta Cryst. 17, 851 (1965).
16. J. Gayoso, H. Bouanani and A. Boucekkine, Bull. Soc. Chim. Fr. 3-4, 538 (1974).
17. H. Bouanani and J. Gayoso, *ibid.*, 3-4, 545 (1974).
18. G. H. Stout, T. S. Lin and I. Singh, Tetrahedron 25, 1975 (1969).
19. E. Rudzitis, M. H. Feder, W. N. Hubbard, J. Phys. Chem. 69, 2305 (1965).
20. E. Rudzitis, Argonne National Laboratory Report ANL-7450, p. 64 (1968).
21. W. N. Hubbard, Argonne National Laboratory Report ANL-75-47, p. 38 (1975).
22. W. N. Hubbard, R. G. Pennell, G. K. Johnson, Argonne National Laboratory Report ANL-76-102, p. 18 (1976).
23. F. H. Spedding, D. C. Henderson, J. Chem. Phys. 54, 2476 (1971).
24. D. W. Osborne and H. E. Flotow, ANL, private communication (1977).
25. E. H. P. Cordfunke, W. Ouweltjes and G. Prins, J. Chem. Thermodyn. 7, 1137 (1975).
26. G. C. Fitzgibbon, D. Pavone and C. E. Holley, Jr., J. Chem. Eng. Data 12, 122 (1967).
27. E. H. P. Cordfunke and P. Aling, Trans. Faraday Soc. 61, 50 (1965).
28. M. M. Popov, F. A. Kostylev and T. F. Karpova, Zh. Neorg. Khim. 2, 9 (1957).
29. L. M. Vidovskii, N. I. Byakhova and E. A. Ippolitova, Zh. Neorg. Khim. 10, 1746 (1965).
30. J. L. Settle, H. M. Feder and W. N. Hubbard, J. Phys. Chem. 67, 1892 (1963).
31. C. Hayman, Proceedings of Thermodynamik-Symposium, K. Schafer (Ed) paper I-7, Heidelberg, 1967.
32. F. L. Oetting, M. H. Rand, and R. J. Ackerman, *The Chemical Thermodynamics of Actinide Elements and Compounds*, Part 1, IAEA, Vienna, 1976.

33. D. D. Wagman, W. H. Evans, V. B. Parker, I. Halow, S. M. Bailey, and R. H. Schumm, NBS Tech. Note 270-3 (1968).
34. M. H. Rand and O. Kubaschewski, *The Thermochemical Properties of Uranium Compounds*, Interscience, New York (1963).
35. V. B. Parker, NBS, private communication, 1976.
36. J. E. Antill, K. A. Peakall and E. F. Smart, J. Nucl. Mater. 56, 47 (1975).
37. P. A. G. O'Hare and J. Boerio, J. Chem. Thermodyn. 7, 1195 (1975).
38. P. A. G. O'Hare, J. Boerio and K. J. Jensen, J. Chem. Thermodyn. 8, 381 (1976).
39. W. G. Lyon, D. W. Osborne and H. E. Flotow, J. Chem. Thermodyn. 7, 1189 (1975).
40. C. F. Knights and B. A. Phillips, to be published in Chem. Soc. Special Publication 30, 1977.
41. M. C. Day, Jr. and J. Selbin, *Theoretical Inorganic Chemistry*, Reinhold, New York (1962).
42. F. A. Cotton and G. Wilkinson, *Advanced Inorganic Chemistry*, 3rd Ed., Interscience, New York (1972).
43. R. L. Nuttall, S. Wise and W. N. Hubbard, Rev. Sci. Instrum. 32, 1402 (1961).
44. D. R. Fredrickson, R. D. Barnes, M. G. Chasanov, R. L. Nuttall, and W. N. Hubbard, High Temp. Sci. 1, 373 (1969).
45. P. A. G. O'Hare and W. N. Hubbard, J. Phys. Chem. 69, 4358 (1965).
46. P. A. G. O'Hare, J. L. Settle and W. N. Hubbard, Trans. Faraday Soc. 62, 558 (1966).
47. W. W. Weller and K. K. Kelley, U. S. Bur. of Mines RT 6511 (1964); NBS Tech. Note 270-3 (1968).
48. V. V. Tarosov and V. M. Zhdonov, Russ. J. Phys. Chem. 44, 1349 (1970).
49. J. S. Haggerty, A. R. Cooper and J. H. Heasley, Phys. Chem. Glasses 9, 47 (1968).
50. M. Hattori, K. Nagaya, S. Umebacki and M. Tanaka, J. Non-Cryst. Solids 3, 195 (1970).
51. G. B. Street and Z. A. Munir, J. Inorg. Nucl. Chem. 32, 3769 (1970).
52. E. V. Britzke, A. F. Kapustinsky, and L. G. Tschenzova, Z. Anorg. Allg. Chem. 213, 58 (1933).

53. K. C. Mills, *Thermodynamic Data for Inorganic Sulphides, Selenides and Tellurides*, Butterworths, London (1974).
54. P. B. Barton, Jr., *Geochim. Cosmochim. Acta* 33, 841 (1969).
55. K. Jellinek and J. Zakowski, *Z. Anorg. Allg. Chem.* 142, 1 (1925).

IV. ENVIRONMENTAL CHEMISTRY

(R. Kumar, P. T. Cunningham, S. A. Johnson,
B. D. Holt, B. R. Hubble, S. Siegel, E. L. Nielsen)

The research programs of the Environmental Chemistry Group involve basic studies on the chemistry of airborne particulate matter and on the chemistry associated with the control of sulfur dioxide emissions through the cyclic use of mineral sorbents. Strong emphasis is being placed on understanding the mechanisms of formation of airborne particulate matter and the mechanisms that are important to SO_2 control by mineral sorbents. The highlights of the recent work done in these areas are given below.

A. Chemistry of Airborne Particulate Matter

(S. A. Johnson, R. Kumar, P. T. Cunningham)

In previous Argonne reports,¹⁻³ as well as other publications,^{4,5} the development of a method for the collection and analysis of time- and size-resolved samples of airborne particulate matter has been presented. The procedure uses a cascade impactor for sample collection and infrared spectroscopy for sample analysis. This method of analysis has been developed to the point where quantitative determination of nitrate and neutral sulfate is possible for samples containing from five to several hundred micrograms of these ions. Systematic variations in the absorption band positions and intensities in the spectra of some sulfate samples are associated with the degree of acidity of the sample. This infrared spectroscopic method has been used to show that there are, indeed, significant variations in the chemistry of atmospheric aerosols with particle size, and that within a specific size range, the chemistry does change with time.^{4,5} Of particular significance has been the identification of ammonium sulfate as the predominant constituent of submicrometer particles, the observation of regionally occurring acidic sulfate episodes, and the observation that the degree of acidity of the sulfate is highly variable with time.

In order to quantify the degree of sulfate acidity in airborne particulate matter, an acidity scale ranging from 0 to 2 is being used. The acidity value of a given sample is the ratio of the hydrogen ion to the sulfate ion, $\text{H}^+/\text{SO}_4^{2-}$, in the sample. This ratio is correlated with the relative band intensities of the 600 cm^{-1} and the 620 cm^{-1} sulfate bands. The scale is illustrated in Fig. IV-1, together with the spectra of the three stable compounds, ammonium sulfate $[(\text{NH}_4)_2\text{SO}_4]$, letovicite $[(\text{NH}_4)_3\text{H}(\text{SO}_4)_2]$, and ammonium bisulfate $[\text{NH}_4\text{HSO}_4]$, which have values of 0.0, 0.5 and 1.0, respectively, on the sulfate acidity scale.

From well over a thousand samples of submicrometer-sized particles collected in recent years in the Midwest--in the Chicago, IL, and St. Louis, MO, areas--only two or three of the spectra were interpreted as indicating the presence of sulfuric acid in the samples. Very few samples were as acidic as ammonium bisulfate (1.0 on the acidity scale). In these midwestern samples, acidic sulfate was measurable in about one-third of the urban samples and in a smaller fraction of the samples from rural sites.⁵

The atmospheric aerosol sample collection and analysis procedure is presently being used in the Multistate Atmospheric Power Production Pollution Study (MAP3S).⁶ MAP3S covers the northeastern quadrant of the

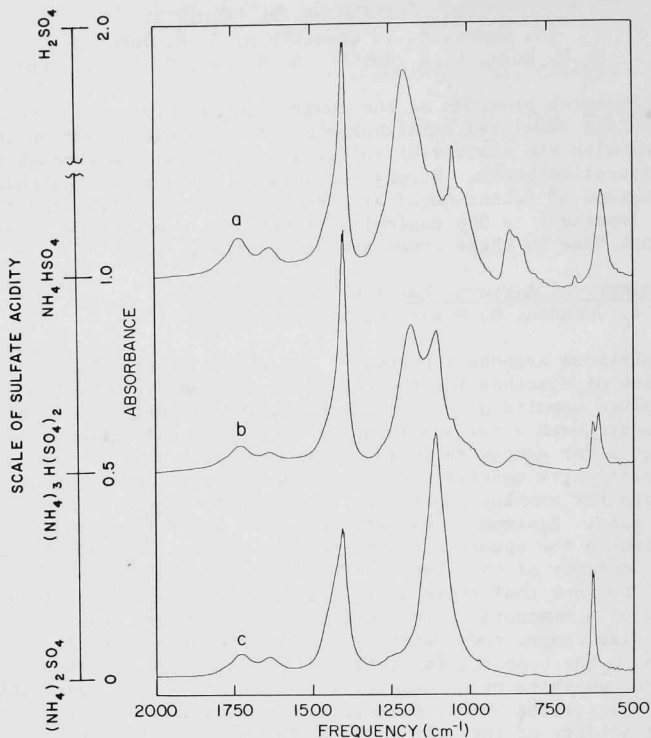


Fig. IV-1. Selected Spectra Showing the Variation in the Spectra of Submicron Particles and the Scale of Acidity (spectrum a = ammonium bisulfate, b = letovicite, c = ammonium sulfate)
ANL Neg. No. 308-3599R

continental United States and involves the collection of current pollutant emission data, atmospheric chemistry data, and atmospheric physics and meteorological modeling of pollutant concentration profiles in time and space.

Airborne particulate matter samples from two MAP3S sites, one near State College, PA, and the other near Charlottesville, VA, have shown a surprisingly large occurrence of acidic sulfate, both in the degree of acidity and the frequency of acidic samples. More than half the samples from these rural sites show measurable acidity, with 35 to 40% of the almost 300 samples analyzed showing an acidity value of 1.0 or greater. Ten samples, or about 3% of those analyzed, contained sulfuric acid (acidity value 2.0). In contrast with these eastern samples, but in agreement with previous midwestern results, only one out of 58 samples from Rockport, IN

(a MAP3S site), and Argonne, IL, showed any significant acidity. The frequent occurrence of acidic ammonium sulfate aerosol in the eastern atmospheres has not been reported previously. These observations are highly significant for the MAP3S, and bear out the usefulness of the sampling and analysis procedure developed at ANL for airborne particulate matter.

B. Oxygen Isotopy in Atmospheric Sulfate Formation*
(B. D. Holt, P. T. Cunningham and R. Kumar)

Oxygen-18 analyses were continued on components of atmospheric sulfate formation in search of new information on the mechanism(s) of oxidation of SO_2 in the atmosphere which predominate under various conditions of location, season, temperature, oxidizing agent, etc.

Results were presented earlier for field samples of sulfates, sulfur dioxide, water vapor, and precipitation water for a 16-month period.³ Variations in the ^{18}O content of particulate sulfate did not appear to correspond to seasonal changes as did isotopic variations in atmospheric water (strongly) and SO_2 (weakly) from which the sulfate was supposedly formed. Continued analyses for 24 months further confirmed these earlier observations. Laboratory experiments were performed to evaluate the isotope fractionation effects in the hydrolysis-oxidation conversion of SO_2 to sulfate. The results of these experiments indicated that the ^{18}O content of the product sulfate was heavily influenced by the ^{18}O content of the water in which it was formed.

In this report, the significant inferences drawn from the analysis of a two-year atmospheric sampling at Argonne, IL, are discussed. A one-year (1975) collection of 24-hour samples of particulate sulfate from San Diego, CA, was analyzed and the results are compared with the results from Argonne. Also, the results of a laboratory experiment to determine the effect of varying the oxidizing agent on the ^{18}O content of sulfate formed by the hydrolysis-oxidation mechanism are presented and discussed. The experimental methods of sample collection and the analytical procedures have been reported previously.^{1,2,7}

1. Results and Discussions

The following observations were made on the results of the two-year study of field samples obtained at Argonne, IL:

(1) The ^{18}O content of both water vapor and precipitation water varied seasonally and in phase with seasonal changes in temperature. The temperature effect appeared to dominate in influencing the isotopic quality of precipitation water during the winter months, in agreement with the discussion by Dansgaard.⁸ The pattern of seasonal variation in ^{18}O content during the spring, summer, and fall months could have been influenced by the

* Assistance in sample collection by E. L. Nielsen and S. A. Johnson, and the analytical work performed by A. G. Engelkemeir and M. F. Bouchard are gratefully acknowledged.

amount of precipitation, as suggested by Dansgaard. It was observed that the precipitation water was, on the average, about 10‰* higher in ^{18}O than water vapor collected at the same time.

(2) The ^{18}O content of sulfate in precipitation water also varied seasonally and in phase with the corresponding variations in the associated precipitation water. The amplitude of the variation in the sulfate was about 0.7 times the corresponding amplitude for the precipitation water. A possible explanation for a factor of $3/4$ would be that three of the four oxygen atoms in the sulfate ion are contributed by the water in which the sulfate is found. Thus, if the sulfate is formed by oxidation of the SO_2 dissolved in the water, the intermediate HSO_3^- ion must become isotopically equilibrated with the large excess of water prior to oxidation to the SO_4^{2-} ion.

(3) The ^{18}O content of atmospheric particulate sulfate showed a random pattern of variation with season. In this respect, the particulate sulfate was unlike the sulfate dissolved in precipitation water. However, the two-year average del values for particulate sulfate and sulfate in precipitation water were almost identical.

(4) No strong correlation was evident between the quantity of particulate sulfate and its ^{18}O content.

(5) The ^{18}O content of sulfate formed by SO_2 collection on the K_2CO_3 -glycerol-treated filter apparently varied seasonally. However, this may not reflect a corresponding seasonal variation in the isotopic content of the atmospheric SO_2 .

(6) The isotopic quality of dustfall varied as a strong function of the dustfall collection rate but only weakly with seasonal changes.

One hypothesis that is consistent with observations 2, 3, and 4 is that the particulate sulfate and the sulfate in precipitation water are both formed by the same hydrolysis-oxidation mechanism in cloud droplets. In a precipitating cloud, some of the sulfate is captured by precipitation water after a relatively short residence in the atmosphere. Thus the isotopic quality of this sulfate corresponds closely with that of the associated water. Conversely, some, perhaps most, of the sulfate escapes capture and is dispersed in the atmosphere as particulate sulfate after release from the host droplet by evaporation. These sulfate particles then experience relatively long residence in the atmosphere, during which time they may mix with other particulate sulfates produced elsewhere. Such mixing may obscure any seasonal effect on the isotopic quality of the aerosol sulfate.

This hypothesis of the atmospheric sulfate formation is also consistent with the results of analysis of atmospheric sulfate samples collected at San Diego, CA, over a period of one year.[†] In these samples, as in the samples collected at Argonne, the ^{18}O content of the particulate sulfate did not show any seasonal pattern. However, the average del value

* The symbol ‰ (del value) is the deviation of the $^{18}\text{O}/^{16}\text{O}$ ratio of a sample from that of a standard in units of parts per thousand.

† Samples obtained from the Air and Industrial Hygiene Laboratory, Department of Health, State of California.

for ^{18}O in the sulfate at San Diego was 4.4‰ higher than that at Argonne. This higher δ value can be attributed to the more southern latitudes in which the San Diego sulfate was formed, as compared with the latitudes in which the sulfate collected at Argonne was formed. The atmospheric water in the lower latitudes is richer in ^{18}O than the water in the higher latitudes.⁹

2. Dependence of Oxygen Isotope Effects on Conditions of Sulfur Oxidation

To examine the effect of varying the conditions of oxidation on the oxygen isotopy of sulfates formed by a hydrolysis-oxidation mechanism, tetravalent sulfur in aqueous solutions of potassium carbonate and glycerol was oxidized to sulfate, both by bromine treatment and by air oxidation in the presence of cupric ions. This experiment was performed to determine a method of treatment of field samples of SO_2 , collected on K_2CO_3 -glycerol filter papers, which are not completely air-oxidized to sulfate at the end of the sampling period. Experience has shown that samples incompletely oxidized in the hi-vol air sampler often require impractically long periods of time to achieve complete oxidation while in storage, prior to isotopic analysis. Exposure to moist air in a covered container somewhat enhances oxidation, but several days or weeks may be required for complete oxidation. The glycerol used in preparation of the alkaline filters is known to be a strong inhibitor to sulfite oxidation.

Figure IV-2 shows the variation of $\delta^{18}\text{O}_{\text{SO}_4^{2-}}$ with $\delta^{18}\text{O}_{\text{H}_2\text{O}}$ for the bromine oxidation (Curve D) and for the Cu^{2+} -catalyzed air oxidation (Curve C). Also plotted in Fig. IV-2 are the corresponding results obtained for sulfates formed in SO_2 - H_2O -air systems (containing no K_2CO_3 or glycerol), as reported previously.³ Curve A represents sulfates formed from SO_2 that was completely oxidized with the stoichiometric amount of air oxygen and excess water in the presence of Fe^{3+} catalyst (~ 1 mg FeCl_3); curve B represents the same system, except that the sulfurous acid was stoichiometrically neutralized with NH_3 (gas) and oxidation occurred in excess air oxygen (vessel open to the air).

It is evident from the plotted data that the $^{18}\text{O}/^{16}\text{O}$ ratio of the sulfates produced by the four different methods of oxidation varied differently as a function of the $^{18}\text{O}/^{16}\text{O}$ ratio of the water in which the sulfates were formed.

The slope of the curve which fits the data of the bromine oxidation is about 1, indicating that all four of the oxygen atoms in the sulfate ion were controlled by the water oxygen in which, and from which, the ion was formed. The slopes of the two curves, A and B, for Fe^{3+} -catalyzed air-oxidation in neutral and slightly acid solutions were about $3/4$, indicating that three of the four oxygens in the sulfate ion were controlled by the water medium. The remaining oxygen in the sulfate ion may have been controlled primarily by the air oxygen, leaving little or none to be controlled by the SO_2 . The slope of the curve for Cu^{2+} -catalyzed air oxidation in the high-pH solutions of K_2CO_3 and glycerol was approximately $2.5/4$, indicating that 2.5 oxygens in the sulfate ion product were controlled by the water oxygen of the excess solvent. The mechanistic origin of the other 1.5 oxygen atoms in the sulfate ion, produced under these conditions, was not investigated.

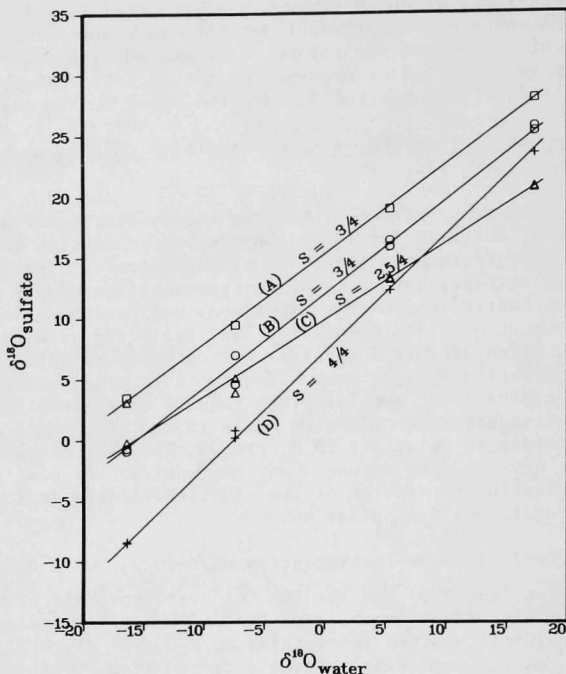


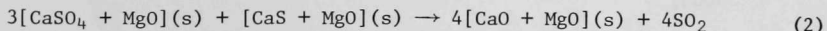
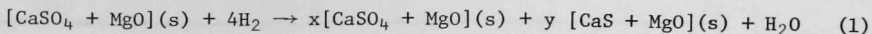
Fig. IV-2. Variations of $\delta^{18}\text{O}_{\text{SO}_4^{2-}}$ with $\delta^{18}\text{O}_{\text{H}_2\text{O}}$ for Different Methods of Oxidation in the Hydrolysis-Oxidation Mechanism of Sulfate Formation (Curve A: H_2SO_4 solution; air oxidation; stoichiometric O_2 ; Fe^{3+} . Curve B: neutral solution; air oxidized; open air; Fe^{3+} . Curve C: K_2CO_3 solution; air oxidized; open air; Cu^{2+} . Curve D: K_2CO_3 solution; Br oxidation; open air) ANL Neg. No. 308-77-637

C. Sulfur Emissions Control Chemistry

1. Dolomite Regeneration Studies: CaSO_4 - CaS Reaction (B. R. Hubble, L. H. Fuchs,* S. Siegel and E. L. Nielsen)

Some of the results of an investigation of the feasibility of a dolomite regeneration scheme based on the following reactions:

* Member of the Chemistry Division, ANL.



have been given in previous reports.¹⁻³ The earlier studies dealt with the stoichiometry of reaction 2 and demonstrated that reaction 2 yields are dependent on the $\text{SO}_4^{2-}/\text{S}^{2-}$ mole ratio of the starting material prepared by the reduction reaction (Eq. 1) at 900°C.

Experiments conducted during the current period were designed to study the effects of (a) the reduction reaction kinetics on the yield of CaO obtained by reaction 2, and (b) the $\text{SO}_4^{2-}/\text{S}^{2-}$ mole ratio on the CaO yield when reaction 1 is carried out under optimum conditions identified under (a). Additional work done is related to (i) an investigation of reaction 2 kinetics, (ii) a microscopic study of starting materials and reaction products, and (iii) an analytical study of the gas evolved in reaction 2, based on the use of gas chromatography (GC). In these studies, the experiments were carried out in a thermal-gravimetric (TG) apparatus, followed by optical-microscopic and X-ray examination of the reaction products.

a. Experimental

The experimental procedure for carrying out the TG experiments was similar to that described in previous reports.¹⁻³ Sulfated stones of -16 +18 U.S. standard screen size were reacted with hydrogen at various concentrations in helium and gas flow rates of 300 cm³/min at 1 atm (101 kPa). Twelve to fifteen particles from selected TG experiments were mounted, sectioned, polished, and examined in reflected light under a microscope. In addition, microtechniques that allowed the selective removal of material from the polished sections provided material for qualitative identification by X-ray powder patterns when mixtures of phases existed that could not be characterized optically. The evolved gas analysis experiments were carried out by connecting the GC to the exit line of the reaction tube of the TG apparatus. Sequential GC measurements were possible every 10 to 15 min during a TG run.

b. Results

Effect of Reduction Reaction Kinetics. To study the effect of reaction 1 conditions (temperature and H₂ concentration) on the subsequent progress of reaction 2, 93% sulfated stones were reduced in various H₂ concentrations and at selected temperatures to a constant, selected yield of $\text{SO}_4^{2-}/\text{S}^{2-}$ mole ratio of 1.2 (see below). These starting materials were then heated under a helium purge at 950°C. The results of the CaSO₄-CaS reaction experiments are shown in Fig. IV-3. The highest reaction 2 yield of (CaO + MgO) and the highest reaction rate were observed for stones prepared at 750°C 6% H₂. These conditions represent the slowest reaction kinetics for the reduction (Eq. 1) step. In general, the results summarized in Fig. IV-3 indicate that slow kinetics for reaction 1 lead to improved kinetics and yields for the subsequent CaSO₄-CaS reaction. One notable exception is the material prepared at 800°C with 2% H₂ which exhibited poorer reaction 2 results than stones prepared at 800°C with 4% and 6% H₂.

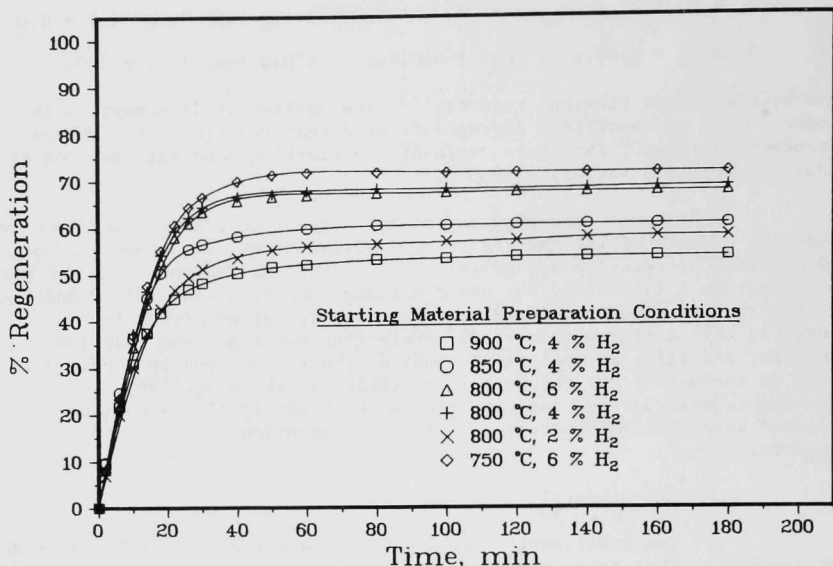


Fig. IV-3. CaSO_4 -CaS Reaction Kinetics at 950°C Using Starting Materials with $\text{SO}_4^{2-}/\text{S}^{2-}$ Mole Ratios of 1.2, but Prepared under Different Conditions.

A microscopic examination of the reduced samples, which were the starting materials for the CaSO_4 -CaS reaction experiments, was carried out to see whether the reduction reaction kinetic effect noted in Fig. IV-3 was related to morphological properties. The major differences between these samples are in the distribution of sulfide and sulfate within the particles. Higher concentrations of CaS on particle exteriors were marked in samples reduced at 900°C-4% H_2 , 800°C-2% H_2 , and 850°C-4% H_2 , but this effect was minimal or absent in samples reduced at 750°C-6% H_2 , 800°C-4% H_2 , and 800°C-6% H_2 . A representative particle from the sample reduced at 800°C-2% H_2 is shown in Fig. IV-4, which depicts the higher amounts of CaS on the exterior. Although firm conclusions are not justified on the basis of this limited number of preliminary sample runs, some general observations may be made which provide a guide for additional experiments.

Formation of higher concentrations of CaS on the particle exteriors is promoted by higher temperatures and probably also by lower H_2 concentrations in the gas. At elevated temperatures the surface reaction to form CaS is rapid and the time to achieve a specific state of reduction is short. The reaction is terminated before the interiors are reduced. On the other hand, at lower temperatures, the surface reaction is slower and the longer time required to reach the predetermined sulfate/sulfide ratio allows greater diffusion of H_2 into, and H_2O out of, the interiors. Thus, the resulting CaS is more uniformly distributed in the particles.

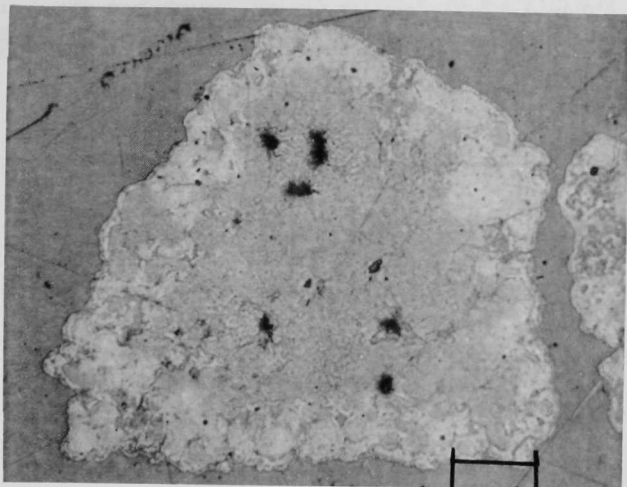


Fig. IV-4. Photomicrograph of a Particle Reduced at 800°C with 2% H_2 [Exterior band is CaS (light gray); interior (darker gray) is $CaSO_4$. Particles from this sample regenerate poorly due to separation of the reactants. Scale bar = 0.2 mm.]

The effect of H_2 concentration is more obscure due to the limited number of samples run. It might be argued, however, that diffusion of H_2 into interiors is enhanced by higher concentrations, whereas at lower concentrations the reaction stops at the surface to form a CaS crust. The three 800°C samples substantiate this suggestion. Particles in the 2% H_2 sample have well-developed crusts but those in the 4% H_2 and 6% H_2 samples have no apparent crust.

It is evident that the percent of regeneration depends upon the previous reduction treatment (Fig. IV-3). The microscopic observations suggest that the solid-solid reaction should be favored by a uniform distribution of the reactants but impeded when they are separated. The experimental results obtained for the solid-solid reaction (Fig. IV-3) are therefore generally consistent with the deductions based on the microscopic observations. One case is different, however, in that the 800°C-4% H_2 sample regenerates better than the 800°C-6% H_2 sample, but the difference is small and apparently the reaction is insensitive in this range. A greater number of samples must be run to more clearly define the combined effects of temperature and H_2 concentration used to prepare the starting materials for the solid-solid reaction.

Effect of $\text{SO}_4^{2-}/\text{S}^{2-}$ Mole Ratio. Starting materials for reaction 2 were prepared by reacting aliquots of 93% sulfated dolomite with 6% H_2 at 750°C for various lengths of time to give $\text{SO}_4^{2-}/\text{S}^{2-}$ mole ratios varying from 0.9 to 2.8. The samples were subsequently reacted at 950°C under $300 \text{ cm}^3/\text{min}$ He flow (reaction 2). The results, shown in Fig. IV-5, indicate that optimum reaction 2 progress occurred when the $\text{SO}_4^{2-}/\text{S}^{2-}$ mole ratio was near 1.6, in contrast to the stoichiometric ratio of 3.

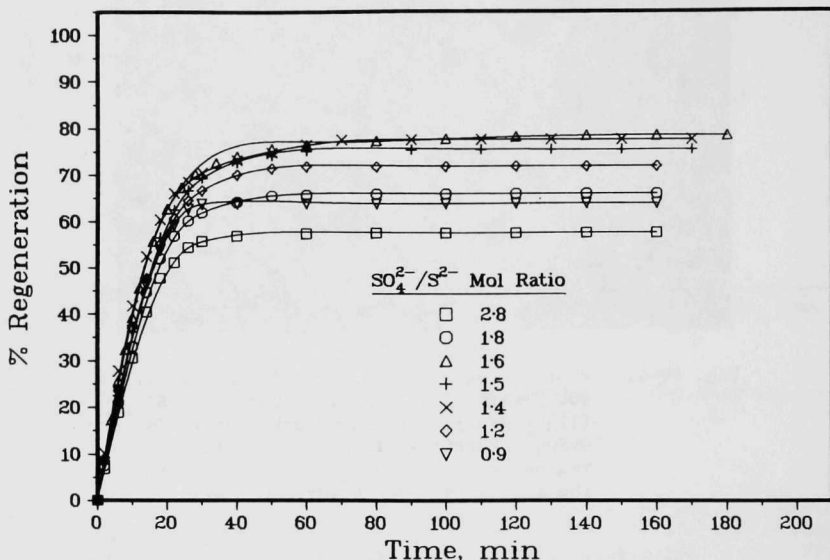
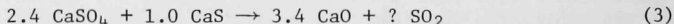


Fig. IV-5. Effect of Various Mole Ratios of $\text{SO}_4^{2-}/\text{S}^{2-}$ on the Kinetics of the CaSO_4 - CaS Regeneration Reaction at 950°C

The kinetics of CaSO_4 - CaS reaction step, shown in Fig. IV-5, are summarized in Table IV-1, which lists initial reaction rates, yields, and times required to reach 80% of maximum yield.

Results of wet chemical analysis of the starting materials and final reacted products from reaction 2 for three of the experiments ($\text{SO}_4^{2-}/\text{S}^{2-} = 2.8, 1.6, \text{ and } 0.9$) shown in Fig. IV-5 indicated that the reaction coefficients associated with the CaSO_4 - CaS reaction may be better described as



if this is the only reaction taking place in the stones. Although the coefficients in Eq. 3 are based on the results of a very limited number of experiments, it is of interest that the coefficients are lower than those

obtained by the X-ray diffraction chemical analysis technique described in an earlier report³ and used as the basis for the TG results shown in Fig. IV-5.

Table IV-1. Summary of Kinetic Parameters for CaSO_4 -CaS Reaction at 950°C

$\text{SO}_4^{2-}/\text{S}^{2-}$ Mole Ratio of Starting Material	Initial Reaction Rate, % Regener./min	Reaction Yield, % Regener.	Time Required to Reach 80% of Maximum Yield, min
2.8	3.11	57.5	18
1.8	3.43	65.9	19
1.6	3.94	78.4	19
1.5	3.52	75.3	20
1.4	4.04	77.5	19
1.2	3.66	71.7	20
0.9	3.66	63.8	17

A microscopic examination of the starting materials for these experiments ($\text{SO}_4^{2-}/\text{S}^{2-}$ mole ratio of 2.8, 1.6 and 0.9) revealed that CaS, CaSO_4 and CaO are, in general, uniformly distributed throughout each particle. There are, however, some exceptions to this generality. In the less reduced sample ($\text{SO}_4^{2-}/\text{S}^{2-} = 2.8$), high concentrations of CaSO_4 are prominent as thin bands which rim the exterior surfaces of particles and as circular bands within the interiors. The band width in both cases is about $5\ \mu\text{m}$. The circular bands enclose areas of sulfide and sulfate. The diameters of these areas are roughly equal to the grain sizes of the original dolomite. This feature is difficult to understand since only a few original grain boundaries are evident on polished sections or thin sections of half-calcined dolomite. These bands of sulfate concentrations tend to disappear in the two more highly reduced samples.

Particles in the samples reduced to $\text{SO}_4^{2-}/\text{S}^{2-}$ mole ratios of 1.6 and 0.9 display moderate gradients in CaSO_4 distribution with slightly greater amounts in the exterior regions. This feature may be ascribed to the coarser grain sizes (up to $10\ \mu\text{m}$) of CaSO_4 in the exteriors of sulfated particles compared with grain sizes of $1\text{--}2\ \mu\text{m}$ in the interiors. Since sulfation of half-calcined particles proceeds from surface to center, the outer sulfate grains grow larger and hence may be more difficult to reduce. These gradients can be correlated with the distribution of CaO formed as a product of the solid-solid reaction as discussed below.

A prominent feature in the CaS-rich samples is the development of cracks due to the decrease in molar volume from that of CaSO_4 to that of CaS. Figure IV-6 shows this effect for two particles having different concentrations of CaS. The particle in Fig. IV-6a has more CaS and consequently displays more cracking than the particle in Fig. IV-6b which contains less CaS. Both particles are from the sample ($\text{SO}_4^{2-}/\text{S}^{2-} = 1.6$) and thus exemplify the differences frequently observed between individual particles in the same sample.

The reduced samples with $\text{SO}_4^{2-}/\text{S}^{2-}$ mole ratios of 2.8, 1.6 and 0.9 (Table IV-1), which yielded 57.5, 78.4 and 63.8% regeneration (reaction 2), respectively, were examined microscopically. In general, the samples appeared completely reacted via the CaSO_4 -CaS reaction until the reaction was terminated by the exhaustion of either of the two reactants. There were particle-to-particle differences, especially in the 58% and 78% regenerated samples. A few particles in each of these samples contained areas of both reactants. The reason why the reaction stopped in these particles was apparently the physical separation of the reactants.

Particles from the 78 and 64% regenerated samples are characterized by exterior bands of CaO; interiors of these particles are mixtures of CaS and CaO. The bands of CaO are especially well developed in the 64% reduced sample as shown for a representative particle in Fig. IV-7. These concentrations of CaO are related to the higher amounts of CaSO_4 on the peripheries of the reduced starting material, as described above. Evidently, the higher sulfate concentrations provided the optimum stoichiometry for the solid-solid reaction to reach completion in these exterior bands, whereas lower amounts in the interiors were insufficient to react with the excess CaS.

Figure IV-8 shows the results of an activation energy study of reaction 2. Starting materials for these experiments were prepared at 750°C with 6% H_2 and had a $\text{SO}_4^{2-}/\text{S}^{2-}$ mole ratio of 1.5. This figure also shows the results of analysis of evolved gas, based on gas chromatography. Only SO_2 was detected; however, no SO_2 was detected in the 750°C experiment. The apparent activation energy based on initial reaction rates computed from the TG data given in Fig. IV-8 is 43.3 kcal/mol.

D. Sulfation Studies: Green River Oil Shale
(B. R. Hubble, L. H. Fuchs,* and E. L. Nielsen)

The investigation of the kinetics and mechanism of the sulfation of calcareous materials has been extended to include oil shale. Experimental results have been obtained which indicate that oil shale from the Mahogany ledge of the Green River formation (28 gal/ton) has short-time (<3 hr) sulfation properties superior to those of 1337 dolomite. Accordingly, the oil shale sorbent system represents a means by which mechanistic information can be obtained on the sulfation process.

Approximately 85% of oil shale (assaying at 25 gal of oil/ton) is mineral matter, about half of which is dolomite and calcite; thus, the Green River oil shales are not true shales but marlstones. These two

* Member of the Chemistry Division, ANL.

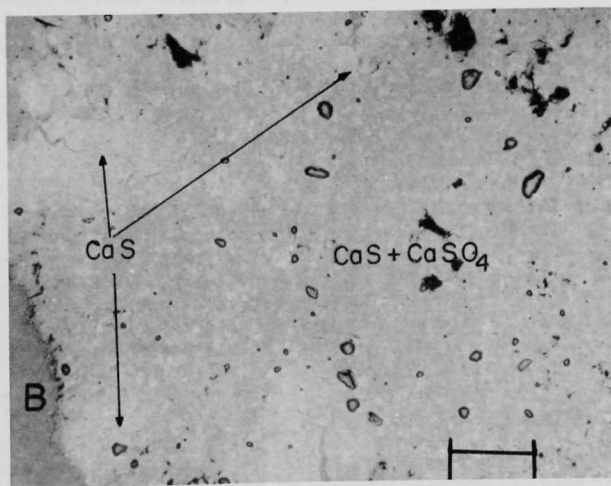
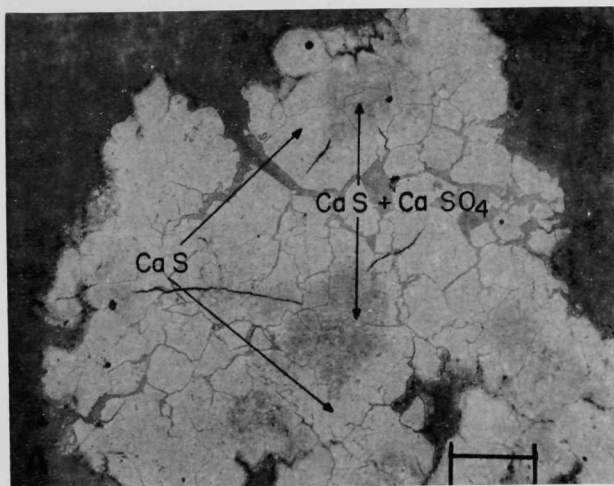


Fig. IV-6. Photomicrographs of Two Particles (A and B) from the Same Sample ($\text{SO}_4^{2-}/\text{S}^{2-} = 1.6$). [Cracks are more abundant in A due to the formation of larger amounts of CaS (light gray). Fewer cracks are present in B which contains less CaS than A. Scale bars = 0.2 mm.]

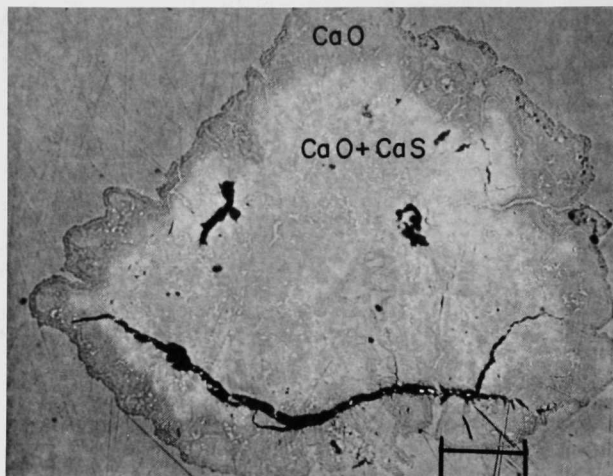
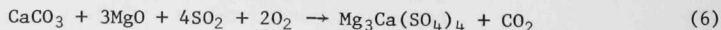
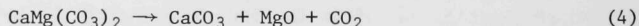


Fig. IV-7. Photomicrograph of a Sulfate-Free Particle after 64% Regeneration (The exterior band of CaO resulted from the slightly greater amount of CaSO_4 on the exterior of the starting reduced material. Unreacted CaS in the interior is consistent with the higher surficial sulfate concentration in the starting material. Scale bar = 0.2 mm.)

carbonates (dolomite and calcite) are the essential components of calcareous rocks considered for use in sulfur emission control. Furthermore, these carbonates in oil shale are fine-grained, with grain sizes ranging from 1 to 10 μm . This can be compared with 1337 dolomite grain sizes which range from 30 to 300 μm . In general, fine-grained calcareous rocks are better SO_2 sorbents than coarse-grained varieties.¹⁰ These two favorable properties, namely, mineral content and fine grain size, warranted an investigation of the sulfation characteristics of spent oil shale.

1. Experimental

The experimental approach parallels that used in the program with 1337 dolomite, namely, half-calcination of the mineral followed by sulfation, according to the following reactions:



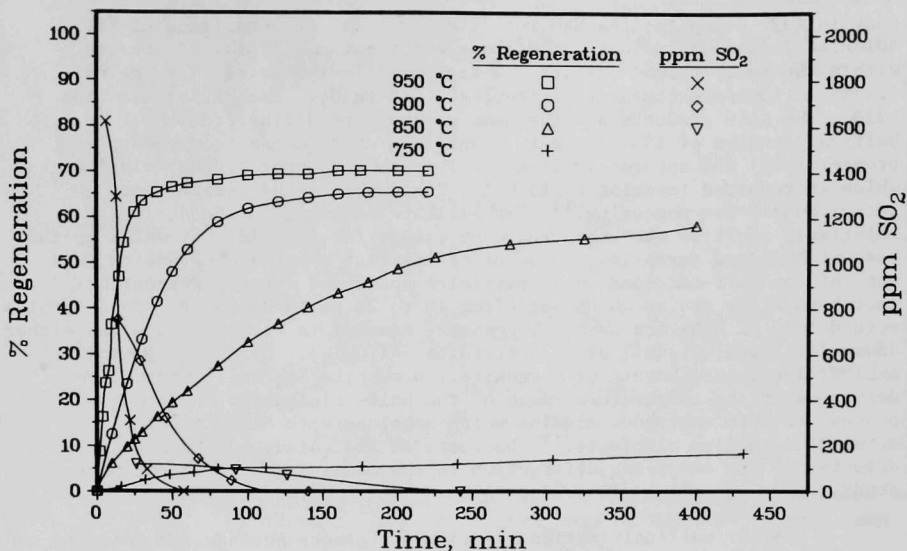


Fig. IV-8. Effect of Temperature on the Reaction Kinetics and SO_2 Evolution for the CaSO_4 - CaS Regeneration Reaction at 950°C with the Initial $\text{SO}_4^{2-}/\text{S}^{2-} = 1.5$

Pretreated shale stones of -16 ± 18 U.S. standard screen size (about 1.1 mm) were used. Thermogravimetric kinetic experiments, employing ~ 200 -mg samples under gas-flow rates of $300 \text{ cm}^3/\text{min}$ at 1 atm (101 kPa), were performed in the manner described in earlier reports.¹⁻³ Treated samples were examined by optical microscopy, X-ray diffraction, and scanning electron microscopy (SEM).

Before the reactions listed above were carried out, the oil shale required pretreatment for the removal of the organic fraction; this was done by preheating the raw shale at 400°C for 15 min in air. The spent shale was then half-calcined at 800°C for 3 hr in 100% CO_2 at 1 atm pressure (reaction 4). The half-calcined shale was then sulfated at 750°C for about 3 hr using a flowing gas mixture consisting of SO_2 (either 0.27 or 3.78%), $\sim 5\% \text{ O}_2$, $\sim 40\% \text{ CO}_2$, balance He (reactions 5 and 6), at 1 atm total pressure.

2. Half-Calcination Results

To ascertain whether the superior sulfation properties of the shale (reported below) are related to its morphological properties, a petrographic examination of the spent and the half-calcined shale was carried out. This study revealed that, during the heat treatment associated with half-calcination, the behavior of shale was in many ways similar to that of 1337 dolomite. In raw shale rich in dolomite and calcite, these two phases are intimately mixed. Upon half-calcination, the coherence of the Ca and Mg exists and is similar to

that in 1337 dolomite; the MgO resulting from the decomposition of the dolomite in the shale does not diffuse but remains uniformly dispersed within the newly formed calcite. X-ray analysis indicates that the main decomposition products are calcite, MgO, and Fe_3O_4 . Except for the iron oxide, the main products are the same as those resulting from the half-calcination of 1337 dolomite. The iron oxide comes from the pyrite present (<1%) and apparently from the ferrous component of the dolomite, which is reported to exist as 15 mol % ferrous iron that substitutes isomorphously for magnesium.¹¹ The silicate minerals in the shale are relatively inert to the heat treatment except for some loss of water in the case of hydrated varieties. A point of interest was the observation that some of the half-calcined shale particles contained several percent of amorphous Al_2O_3 grains which were from 10 to 20 μm in diameter. These grains were devoid of SiO_2 and Na_2O . The source mineral in the raw shale was either dawsonite [$\text{NaAl}(\text{OH})_2\text{CO}_3$] or nordstrandite [$\text{Al}(\text{OH})_3$]. Oil shale is known to exhibit local enrichments of dawsonite. Dawsonite has been observed to decompose in the temperature range of the half-calcination in a two-step process to form amorphous alumina which combines with Na_2O to form crystalline sodium aluminate.¹² However, as indicated, no sodium was detected by SEM and X-ray diffraction in the alumina grains in the present study.

After half-calcination, a major difference between the dolomite and oil shale is the marked increase in the porosity of the shale. Not only does the half-calcined shale have a greater pore volume than half-calcined dolomite (0.4686 cm^3/g vs. 0.2132 cm^3/g), but also the distribution of pore sizes in the shale is shifted toward larger pores. For example, in half-calcined shale 83% of the pores have diameters larger than 0.1 μm , whereas in half-calcined dolomite only 34% of the pores have diameters larger than 0.1 μm . The enhanced porosity of the shale is undoubtedly due to the removal of the kerogen, whereby a multitude of submicrometer intergranular voids are produced. Larger voids ($\geq 5 \mu\text{m}$) are apparent in polished sections of the shale. The increased porosity of the shale should have two favorable effects on sulfation: (1) increased permeability, and (2) increased effective surface area.

3. Sulfation Results

If reactivity toward sulfation were based solely on the amount of CaCO_3 present, a comparison of the relative amounts of this compound in the dolomite and oil shale would indicate that 2.1 times more shale than dolomite would be required to react with the same amount of SO_2 . This relationship holds true for complete sulfation involving long reaction times; however, higher reaction rates for the shale make it more favorable for the relatively short sulfation periods of 3 hr or less than might be encountered in fluidized-bed combustion. The experimental results are given in Fig. IV-9 for concentrations of 0.27 and 3.78% SO_2 . Weight gains are proportional to the quantities of SO_2 reacted to form sulfates.

The initial reaction rates (*i.e.*, at time = 0) computed from the results with 0.27% SO_2 given in Fig. IV-9 are 0.45 mg weight gain/(100 mg of half-calcined shale)(minute) for the shale and 0.08 mg weight gain/(100 mg of half-calcined 1337 dolomite)(minute) for the dolomite. Thus, the initial

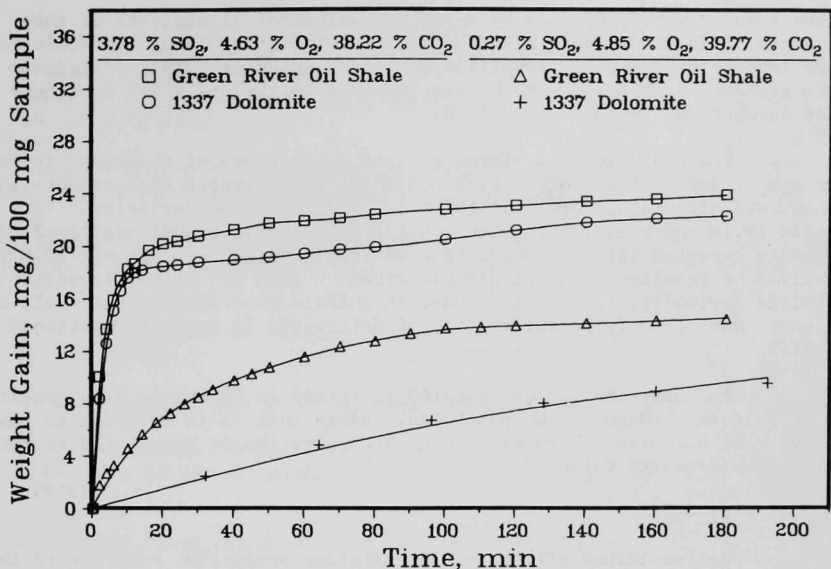


Fig. IV-9. Sulfation Kinetics at 750°C for Half-calcined Oil Shale and Half-calcined 1337 Dolomite

reaction rate of shale is nearly six times that of 1337 dolomite. Based on a unit mass of sorbent, the oil shale captured 1.5 times more SO₂ after 3 hr than did the dolomite. For dolomite, the weight gain after 3 hr represents 37% conversion of CaCO₃ to CaSO₄, whereas for the shale, the weight gain represents approximately 120% conversion of CaCO₃. Thus, it is evident that, in the half-calcined shale, phases other than CaCO₃ are being sulfated. X-ray and petrographic analyses indicate that some MgO is reacting to form the binary sulfate, Mg₃Ca(SO₄)₄. If the assumption is made that all of the CaCO₃ in the shale has been sulfated, then the observed weight gain indicates that approximately 20% of the MgO has been converted to Mg₃Ca(SO₄)₄. Thus, the increased sorbent capacity of the shale as compared to the capacity of dolomite is, in part, related to its ability to form substantial amounts of Mg₃Ca(SO₄)₄.

The initial reaction rates computed from the 3.78% SO₂ results given in Fig. IV-9 are 3.03 mg weight gain/(100 mg of half-calcined shale)(minute) and 2.89 mg weight gain/(100 mg of half-calcined dolomite)(minute). Thus, at this higher SO₂ concentration, the initial reaction rates of shale and dolomite were similar, but after 3 hr the shale had captured 1.1 times more SO₂ than the dolomite. The weight gain of the 1337 dolomite after 3 hr represents a maximum of 87% conversion of available CaCO₃ to CaSO₄ [a small fraction of this weight gain is associated with the formation of Mg₃Ca(SO₄)₄]. The weight gain for the shale indicates that essentially all of the CaCO₃ and MgO have been converted to CaSO₄ and Mg₃Ca(SO₄)₄.

These results were supported by X-ray and wet-chemical analyses of the products. Thus, for short reaction periods of 3 hr or less, the shale has more favorable sulfation properties than 1337 dolomite. This difference is more pronounced at the lower SO_2 reactant concentration, which is closer to that encountered in coal combustion.

Scanning electron microscopy and X-ray scans of shale particles at the end of the 3-hr sulfation with 0.27% SO_2 demonstrated that sulfur (and hence, sulfate) is uniformly distributed throughout the particles. This result is in sharp contrast to the sulfation behavior of half-calcined 1337 dolomite reported earlier, which upon sulfation with 0.39% SO_2 at 750°C for nearly 3 hr resulted in a sulfate distribution that was primarily on the particle periphery.¹³ The difference in sulfate distribution for shale and dolomite can probably be related to the difference in porosity mentioned earlier.

The distribution of $\text{Mg}_3\text{Ca}(\text{SO}_4)_4$ formed in the shale also appears to be uniform throughout the particles. Again this is in contrast to the behavior of dolomite, where binary sulfate formation is restricted to exterior surfaces and cavity walls.¹⁴

4. Discussion

Half-calcined oil shale has sulfation properties superior to those of half-calcined 1337 dolomite for short reaction times owing to higher reaction rates. Two factors that may account for the higher rates for the shale are (1) greater porosity, which leads to increased permeability, and (2) greater tendency for MgO to form $\text{Mg}_3\text{Ca}(\text{SO}_4)_4$. In our previous studies on the sulfation of half-calcined dolomite, we observed that CaSO_4 formation begins on the exterior surfaces of particles and then gradually proceeds to the interiors. In the case of shale, the marked increase in the porosity that results from the removal of kerogen significantly accelerates the sulfation process. Formation of the binary sulfate is also related to porosity. In dolomite, the minor amounts of binary sulfate present are confined to thin ribbons on exterior surfaces and cavity walls; the reaction is not only surface-controlled but stops after the surfaces become encrusted with the binary sulfate. The larger effective surface area of the shale apparently increases its capability to form the binary sulfate before the reaction is stopped by some limiting thickness of the crust.

The superior sulfation characteristics of oil shale as compared with 1337 dolomite are more pronounced at low SO_2 concentrations. Thus, oil shale has the potential for providing more efficient removal of SO_2 , particularly at the low concentrations encountered in fluidized-bed combustors. Accordingly, a potential new use for spent shale has been identified, thereby adding also to the potentiality of low grade raw shale.

REFERENCES

1. *Chemical Engineering Division Physical Inorganic Chemistry Annual Report, July 1973-June 1974*, Argonne National Laboratory Report ANL-8123 (1974).
2. *Chemical Engineering Division Environmental Chemistry Annual Report, July 1974-June 1975*, Argonne National Laboratory Report ANL-75-51 (1975).
3. *Chemical Engineering Division Environmental Chemistry Annual Report, July 1975-June 1976*, Argonne National Laboratory Report ANL-76-107 (1977).
4. P. T. Cunningham, S. A. Johnson and R. T. Yang, *Environ. Sci. Technol.* **8**, 131 (1974).
5. P. T. Cunningham and S. A. Johnson, *Science* **191**, 77-79 (Jan 1976).
6. M. C. MacCracken, *MAP3S: An Investigation of Atmospheric Energy Related Pollutants in the Northeastern United States*, *Atmos. Environ.* **12**, 649-659 (1978).
7. B. D. Holt, *Anal. Chem.* **49**, 1664 (1977).
8. W. Dansgaard, *Tellus* **16**, 437 (1964).
9. H. Förstel, A. Putral, G. Schleser, and H. Lieth, *The World Pattern of Oxygen-18 in Rainwater and Its Importance in Understanding the Biogeochemical Oxygen Cycle*, Symposium on Isotope Ratios as Pollutant Source and Behaviour Indicators, Vienna, Nov. 18-22, 1974, IAEA-SM-191/8 (1975).
10. R. D. Harvey and J. C. Steinmetz, *Environ. Geol. Notes*, No. 50, Ill. State Geol. Survey, 1971, pp. 26.
11. J. W. Smith and W. E. Robb, *J. Sediment. Petrol.* **36**, 486 (1966).
12. C. W. Huggins and T. E. Green, *Amer. Mineral* **58**, 548 (1973).
13. B. R. Hubble *et al.*, *Proc. Fourth Int. Conf. on Fluidized-Bed Combustion*, N. H. Coates, Ed., The MITRE Corporation, McLean, VA, 1976, pp. 367.
14. B. R. Hubble *et al.*, *J. Air Pollut. Control Assoc.* **27**, 344 (1977).

V. STRUCTURAL AND SURFACE STUDIES
(S. Siegel and C. A. Melendres)

A. Kinetics of Electrochemical Incorporation of Lithium in Solid Alloy Electrodes
(C. A. Melendres)

The electrochemical incorporation of lithium into aluminum wire electrodes in molten LiCl-KCl eutectic electrolyte at 450°C was investigated by chronocoulometric, galvanostatic, and potentiostatic techniques.¹ Results of the chronocoulometric measurements were interpreted in terms of the theory developed by Astakhov.² The incorporation of lithium at low current densities (*e.g.*, <5 mA/cm²) to form the solid-solution α -LiAl phase was found to be limited by the rate of lithium diffusion into aluminum, with a measured diffusion coefficient of about 4×10^{-10} cm²/sec at 450°C. Implantation at potentials where a layer of intermetallic compound forms on the electrode surface (*i.e.*, <290 mV anodic of Li/Li⁺ potential in the same electrolyte) was found to be limited initially by the reaction to form the compound LiAl (β -phase) and subsequently by the rate of lithium diffusion into the growing β -phase layer. The results of galvanostatic transient measurements indicate a diffusivity of lithium in β -LiAl of the order of 10^{-8} cm²/sec and a fast charge transfer step. The initial steps in the formation of the intermetallic compound appear to involve typical electrocrystallization processes (nucleation and lattice growth). The process of electrochemical incorporation in solid alloy electrodes which involves the formation of an intermetallic compound bears a striking similarity to the high-temperature oxidation of metals.

The effect of magnesium alloying with aluminum on the kinetics of lithium incorporation into Mg-Al wire electrodes and its subsequent anodic extraction from Li-Al-Mg electrodes is also under investigation.

B. Structural and Morphological Studies on Solid Alloy Electrodes
(C. A. Melendres, S. Siegel, C. Sy,* J. Settle,† and B. Tani‡)

The structural and morphological changes that occur during the charging and cyclic discharging of Li-Al wire electrodes in molten LiCl-KCl eutectic electrolyte at 450°C have been examined by metallographic, electrochemical and X-ray diffraction techniques. On anodic discharge of Li-Al wires, a diffusional type of polarization occurs that decreases progressively with each successive cycle and is accompanied by an apparent increase in lithium diffusivity. This is thought to arise because of an increase in internal area of the electrode due to comminution. Metallographic examination of charged and discharged electrodes has confirmed this hypothesis. The degree of electrode breakdown was found to be more pronounced on discharge than on charge and appears to depend mainly on the depth of discharge. Lithium distribution in wire electrodes during charging appears to be nonuniform. Metallographic and X-ray diffraction investigations lead to the conclusion

* Member of the ANL Chemical Engineering (CEN) Division's Cell Chemistry Group.

† Member of the CEN Division's Materials Group.

‡ Member of the ANL Analytical Chemistry Laboratory.

that the removal of Li from the β -LiAl phase leaves an aluminum matrix of well-separated Al atoms which must undergo major diffusion to form the face-centered-cubic Al structure. Since the α -LiAl and Al structures are similar, diffusion of Al in α -LiAl takes place only to fill vacant atomic sites remaining after Li removal. Because the α - and β -phases appear interspersed, islands or patches of Al will remain, thus leading to increased surface area.

A ternary alloy, based on the incorporation of Mg into Li-Al, is being developed and may demonstrate different morphological changes than those occurring in the binary alloy. Two ternary alloys of Li-Al-Mg are known: Li_2AlMg is reported to be isostructural with β -LiAl,³ leading to the possibility of solid solution and hence increased electrode stability; LiMgAl_2 , of unknown structure, may also play a role in the electrode development.

C. Studies of Corrosion in Molten Salt Systems
(C. A. Melendres and S. Siegel)

The mechanism and rate of corrosion of selected metals and alloys in sulfide and oxide solutions in molten LiCl-KCl eutectic are under investigation. A study of the anodic sulfidation of iron by cyclic voltammetry and controlled potential electrolysis revealed the formation of sulfide coatings whose compositions depend on the applied potential.⁴ An FeS phase was present in samples anodized at potentials between 1.38 and 1.75 V vs. Li-Al in 0.01 and 0.02 molal Li_2S solutions in molten LiCl-KCl eutectic at 450°C, while a sulfide phase of approximate composition $\text{LiK}_6\text{Fe}_{24}\text{S}_{26}\text{Cl}$ (often referred to as J-phase) was found also when the potential was kept between 1.38 and 1.55 V. Optical and scanning electron microscopy showed these phases to have the same hexagonal crystal habit. Further characterization of the structures of the different sulfide phases found during the operation of iron sulfide cathodes is being undertaken using Mössbauer spectroscopy and X-ray diffraction.

The anodic corrosion behavior of the first-row transition metals in an oxide environment is also being studied. The formation of oxide films and their subsequent electroreduction have been found, by cyclic voltammetry, to proceed reversibly on cobalt and copper but only quasi-reversibly on nickel (Figs. V-1, -2, -3). These materials appear to be promising as cathodes for molten-salt secondary batteries.

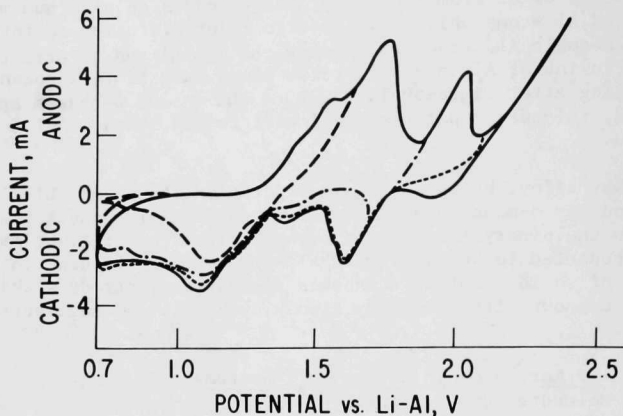


Fig. V-1. Cyclic Voltammograms of Cobalt/Oxide in 0.54M Solution of Li_2O in LiCl-KCl Eutectic at 450°C (scan rate = 10 mV/sec; differences in line symbols indicate different cutoff potentials)

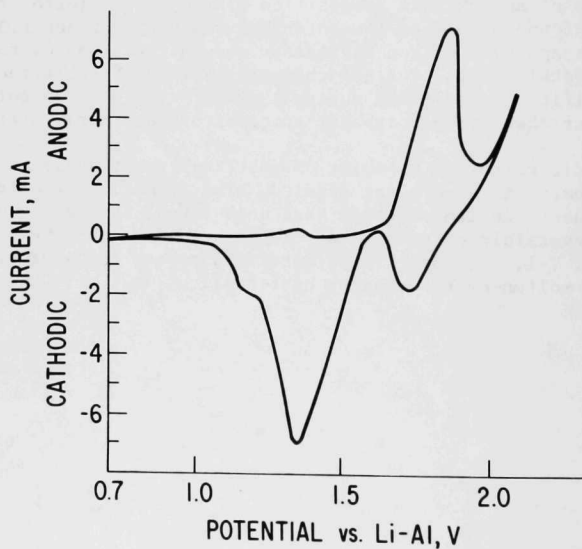


Fig. V-2. Cyclic Voltammogram of Copper/Oxide in 0.54M Solution of Li_2O in LiCl-KCl Eutectic at 450°C (scan rate = 5 mV/sec)

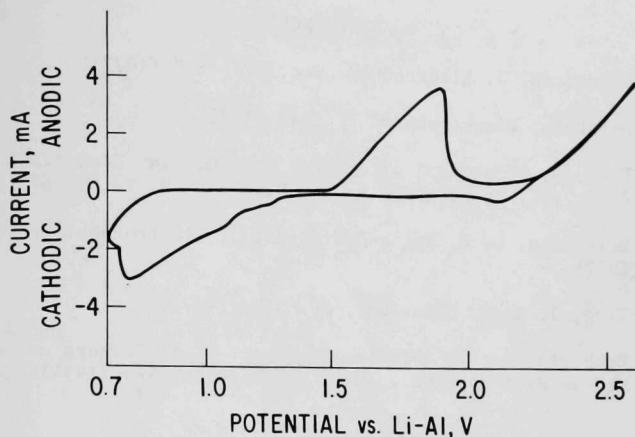


Fig. V-3. Cyclic Voltammogram of Nickel/Oxide in
0.54M Solution of Li_2O in LiCl-KCl
Eutectic at 450°C (scan rate = 20 mV/sec)

D. Bond Strength-Bond Length Relationships for Metal-Oxygen Bonds
(S. Siegel)

A bond strength-bond length relationship has been formulated utilizing structural data of uranyl salts. The bond distance D is given by $D = D(1) - K(1 - 1/S)$, where D is the bond length for bond strength S , and $D(1)$ is the bond length for unit bond strength. It can be shown that a more general form of the relationship is $D = A + K/S$, where A and K appear to be cation and anion covalent radii, respectively. The expression is useful for S values between 1 and 2 and has been applied successfully to $\text{U}^{6+}\text{-O}$, $\text{B}^{3+}\text{-O}$, $\text{V}^{5+}\text{-O}$, and $\text{Mo}^{6+}\text{-O}$ bonds. However, expansion of the Pauling log S form⁵ and inclusion of the Zachariasen coordination correction,⁶ ΔN , leads to the relation $D = \alpha - \beta S^x$, where α , β , and x are readily evaluated. Refinement of the evaluated quantities leads to reasonable D - S relationships for all S (or D) values.

REFERENCES

1. C. A. Melendres, J. Electrochem. Soc. 124, 650 (1977).
2. I. I. Astakhov, Elektrokhim. 8, 1549 (1972).
3. W. B. Pearson, *A Handbook of Lattice Spacings and Structures of Metals and Alloys*, Vol. 2, Pergamon Press, New York, N. Y., p. 67 (1967).
4. C. A. Melendres, C. C. Sy, and B. Tani, J. Electrochem. Soc. 124, 1060 (1977).
5. L. Pauling, J. Amer. Chem. Soc. 69, 542 (1947).
6. W. H. Zachariasen, *The Actinide Elements*, G. T. Seaborg and J. J. Katz, Eds., McGraw-Hill Book Co., Inc., New York, p. 769 (1954).

Distribution for ANL-78-42Internal:

J. P. Ackerman	S. A. Johnson	E. Van Deventer
D. L. Barney	A. A. Jonke	E. Veleckis
M. Blander (3)	G. M. Kesser	D. R. Vissers
J. Bogard	K. Y. Kim	J. R. Weston
L. Burris (4)	G. H. Kucera	R. E. Winans
F. A. Cafasso (5)	R. Kumar (5)	N. P. Yao
R. G. Clemmer	V. A. Maroni (10)	R. M. Yonco
L. L. Cuba	J. J. Marr	B. Ancker-Johnson
P. T. Cunningham (2)	C. A. Melendres	E. J. Croke
L. A. Curtiss	A. F. Melton	J. E. Draley
H. M. Feder	Z. Nagy	P. R. Fields
A. K. Fischer	P. A. Nelson	P. Frenzen
H. E. Flotow	E. L. Nielson	B. R. T. Frost
D. J. Frurip	P. A. G. O'Hare	B. B. Hicks
L. H. Fuchs	G. N. Papatheodorou	M. V. Nevitt
D. W. Green	P. Raptis	W. P. Norris
D. M. Gruen	T. A. Renner	E. G. Pewitt
H. R. Hoekstra	M. F. Roche	R. E. Rowland
B. D. Holt	M. L. Saboungi	D. M. Rote
W. N. Hubbard	J. L. Settle	W. K. Sinclair
B. R. Hubble	A. Sheth	A. D. Tevebaugh
H. R. Isaacson	H. Shimotake	A. B. Krisciunas
C. E. Johnson (10)	S. Siegel	ANL Contract File
G. K. Johnson	M. J. Steindler	ANL Libraries (5)
I. Johnson	R. K. Steunenber	TIS Files (6)
	C. C. Sy	

External:

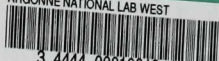
DOE-TIC, for distribution per UC-4 (198)
 Manager, Chicago Operations Office
 Chief, Office of Patent Counsel, CH
 President, Argonne Universities Association
 Chemical Engineering Division Review Committee:

- C. B. Alcock, U. Toronto
- R. C. Axtmann, Princeton U.
- R. E. Balzhiser, Electric Power Research Inst.
- J. T. Banchemo, U. Notre Dame
- T. Cole, Ford Motor Co.
- P. W. Gilles, U. Kansas
- R. I. Newman, Allied Chemical Corp.
- G. M. Rosenblatt, Pennsylvania State U.

D. Ballantine, Div. Biomedical and Environmental Research, USDOE
 J. E. Baublitz, Office of Fusion Energy, USDOE
 R. W. Beadle, Div. Biomedical and Environmental Research, USDOE
 J. T. Bell, Oak Ridge National Lab.
 J. Braunstein, Oak Ridge National Lab.
 L. Brewer, U. California, Berkeley
 F. E. Coffman, Office of Fusion Energy, USDOE
 J. H. DeVan, Oak Ridge National Lab.
 J. Durham, USEPA, Research Triangle Park

R. P. Epple, Div. Basic Energy Sciences, USDOE
L. M. Ferris, Oak Ridge National Lab.
W. R. Grimes, Oak Ridge National Lab.
R. G. Hickman, Lawrence Livermore Lab.
E. F. Johnson, Princeton U.
S. Langer, General Atomic
G. G. Libowitz, Allied Chemical Co., Morristown
L. Nelson, Sandia Corp., Albuquerque
L. Newman, Brookhaven National Lab.
T. Novakov, Lawrence Berkeley Lab.
J. Powell, Brookhaven National Lab.
F. D. Rossini, Rice U.
A. W. Searcy, Lawrence Berkeley Lab.
R. K. Stevens, USEPA, Research Triangle Park
J. S. Watson, Oak Ridge National Lab.
E. F. Westrum, Jr., U. Michigan
R. H. Wiswall, Brookhaven National Lab.
M. Wittels, Div. Basic Energy Sciences, USDOE
R. W. Wood, Div. Biomedical and Environmental Research, USDOE
G. M. McCracken, Culham Lab., UKAEA, Abingdon, England

ARGONNE NATIONAL LAB WEST



3 4444 00010813 4